Thermal Stability and Degradation of NCA in Solid-polymer Batteries

Zur Erlangung des akademischen Grades eines

Doktors der Ingenieurwissenschaften (Dr.-Ing.)

von der KIT-Fakulät für Maschinenbau des
Karlsruher Instituts für Technologie (KIT)
angenommene

Dissertation

von

M.Sc. Münir Mustafa Besli
aus Aalen

Tag der mündlichen Prüfung:	14. Juni 2021
Hauptreferent:	Prof. Dr. rer. nat. Gerhard Schneider
Korreferent:	Prof. Dr. rer. nat. Hans Jürgen Seifert

Dedicated to my late mom, who wanted to see this happen so much,
and to my dad, my greatest hero and encourager.

Abstract

Solid-state batteries utilizing solid-polymer electrolytes in combination with Ni-rich cathodes such as $LiNi_{0.8}Co_{0.15}Al_{0.05}O_2$ (NCA) are promising candidates for the next-generation of energy storage devices. Considering the advantages with regards to safety and potentially high energy densities, many start-ups and companies have looked into commercializing this technology. However, numerous challenges such as the restricted battery performance due to limitations arising from the (thermally) susceptible cathode material, the small electrochemical stability window of suitable polymer electrolytes, and other, yet to be elucidated, degradation processes remain. This thesis is therefore focused on analyzing several possible degradation phenomena arising on different levels of solid-polymer batteries in combination with NCA. A special emphasis is put on the chemical, thermal, and mechanical interplay of the hierarchically structured solid-polymer battery by employing advanced synchrotron techniques.

The systematic approach attempts to clarify the sophisticated thermomechanical, chemothermal, and chemomechanical stability of NCA in a delithiated state on a single particle level. A decomposition provoked by thermal stress in the form of oxygen evolution, phase transformation with concomitant Ni reduction, and, for the first time, the formation of mesopores is demonstrated. Additionally, the importance of the chemothermal interplay of the active material, polymer electrolyte, and Li salt within the cathode of a solid-polymer battery is shown. Ultimately, it is illustrated that the formation of mesoscale intergranular cracks causes a deactivation of sub-particle level domains, and consequently loss of ionic and electrical contact within particles, increasing the local impedance due to rearrangement of transport pathways for charge carriers.

Kurzfassung

Festkörperbatterien mit Polymerelektrolyt in Kombination mit Ni-reichen Kathodenmaterialien, wie zum Beispiel $LiNi_{0.8}Co_{0.15}Al_{0.05}O_2$ (NCA), sind vielversprechende Kandidaten für die nächste Generation von Energiespeichern. Angesichts der Vorteile hinsichtlich Sicherheit und der potentiellen Ermöglichung von hohen Energiedichten, haben sich zahlreiche (Start-up-) Unternehmen mit der Kommerzialisierung dieser Technologie auseinandergesetzt. Dennoch verbleiben einige technologische Herausforderungen, die auf die eingeschränkte Batterieleistung aufgrund des (thermisch) anfälligen Kathodenmaterials, die engen elektrochemischen Stabilitätsfenster nutzbarer Polymerelektrolyte, und andere, noch aufzuklärende, Degradationsprozesse zurückzuführen sind. Diese Arbeit ist daher auf die Analyse möglicher Degradationsphenomäne fokussiert, die auf unterschiedlichen Ebenen der Polymer-Festkörperbatterien in Kombination mit NCA vorkommen. Durch die Nutzung moderner Synchrotrontechniken, wird hierbei ein besonderer Schwerpunkt auf das chemische, thermische und mechanische Zusammenspiel der hierarchisch strukturierten Polymer-Festkörperbatterie gelegt.

Die systematische Herangehensweise bestrebt hierbei die komplexe thermomechanische, chemo-thermische, und chemo-mechanische Stabilität von NCA im delithiierten Zustand, auf der Ebene eines einzelnen Partikels, aufzuklären. Dabei wird dargestellt, wie sich die durch thermische Belastungen ausgelöste Zersetzung in Form von freigesetztem Sauerstoff, Phasenumwandlung und gleichzeitiger Reduktion von Ni sowie durch die Entstehung von Mesoporen zeigt. Zudem wird die hohe Bedeutung des chemo-thermischen Zusammenspiels des Aktivmaterials, Polymerelektrolyten und Lithiumsalzes in der Kathode demonstriert. Letztendlich wird illustriert, dass die Entstehung von intergranularen Frakturen die Deaktivierung von Subpartikel-Domänen verursacht und folglich einen Verlust der Ionen- und Elektronenleitfähigkeit innerhalb von Partikeln, die wiederum eine lokale Impedanzerhöhung so wie Änderung der Transportwege von Ladungsträgern mit sich bringt.

Acknowledgments

This thesis would not have been possible without the contribution, encouragement, support and guidance of many kind-hearted people I have met throughout the entirety of my studies and life.

First, I would like to express my sincere gratitude to my advisor Prof. Dr. Gerhard Schneider, who not only handed me the opportunity to introduce myself to Bosch as a potential PhD candidate, but also gave me the freedom to work and think independently, while always supporting and guiding me. It was an invaluable experience that I will never forget. I would also like to convey a very special thank you to the dissertation committee, second examiner Prof. Dr. Hans Jürgen Seifert, committee chair Prof. Dr. Jürgen Fleischer, and overseer Prof. Dr. Friedrich Prinz for their interest in my work and making my defense happen in these unprecedented times. I would also like to thank Prof. Dr. Dirk Flottmann, who has been an invaluable part of my scientific endeavors, since the day I appeared in his class years ago.

I want to convey my heartfelt gratitude to Dr. Saravanan Kuppan. Sara introduced me to the synchrotron- and microscopy-based characterization of batteries, which opened the path for amazing research and collaborations. I will never forget the countless hours and night shifts we spent together at the beamlines and Bosch laboratories, always pushing for more. But I will also keep the nice memories from our camping trips in my heart.

I would also like to thank Dr. Michael Metzger. Michael has taught me tremendous things about Li-ion batteries for which I am very appreciative. I remember how, from my very first day at Bosch, he helped me by sending interesting papers, discussing with me the degradation processes in batteries, and was always willing to answer my questions whenever I appeared at his desk. I learned to be extremely meticulous and detailed with my research work from him, which was an invaluable lesson for me.

I am also grateful to Dr. Christina M. Johnston. Over the past years

Christina always had my back. During our numerous talks, walks and meetings, she has given me priceless scientific and interpersonal life lessons. I will never forget this.

A very special thanks goes to Dr. Jake Christensen and the entire team at Bosch in Sunnyvale. To Jake, for giving me the opportunity to work with his team over the past years, and to the team for making every day in the office and lab a joyful and great experience. I am very grateful that I have been part of this exceptional team.

My acknowledgments also go out to all collaborators and staff at the Stanford Synchrotron Radiation Lightsource[i], the Lawrence Berkeley National Laboratory, and the Molecular Foundry[ii], who were very supportive during sample preparation, data acquisition, processing, and manuscript review: Dr. Marca M. Doeff, Dr. Yijin Liu, Dr. Alpesh K. Shukla, Dr. Sihao Xia, Dr. Chenxi Wei, Dr. Dennis Nordlund, Dr. Sami Sainio, Dr. Sam Webb, Dr. Sharon Bone, Dr. Erik Nelson, and Dr. Matthew Latimer.

I am very thankful for Camille, who shared every step of this journey with me and has been invaluably supportive and loving. Her place in my heart is very special, and her presence has changed my life in so many beautiful ways that I never want to miss again.

Finally, I would like to express my heartfelt gratitude to my family for their support and patience. Words cannot explain how grateful I am for my parents, my father Oğuzhan Beşli and my late mother Avatif Beşli, who departed from us in the final stages of writing this thesis. All the sacrifices they have made for me and my siblings, their unconditional love, support, encouragement, the values they thought me, and their constant believe in me is what kept me going all my life.

---

[i] Use of the Stanford Synchrotron Radiation Lightsource, SLAC National Accelerator Laboratory, is supported by the U.S. Department of Energy, Office of Science, Office of Basic Energy Sciences under Contract No. DE-AC02-76SF00515.

[ii] Work at the Molecular Foundry was supported by the Office of Science, Office of Basic Energy Sciences, of the U.S. Department of Energy under Contract No. DE-AC02-05CH11231.

Contents

List of Figures

List of Tables

Acronyms

2D-FF-TXM two-dimensional full-field transmission X-ray microscopy

3D-FF-TXM three-dimensional full-field transmission X-ray microscopy

AC alternating current

AEY auger electron yield

ALD atomic layer deposition

ARC accelerating rate calorimetry

ASSBs all-solid-state batteries

BIB broad ion beam

CCD charge-coupled device

DEC diethyl carbonate

DMC dimethyl carbonate

DoE U.S. Department of Energy

DSC differential scanning calorimetry

$\mathbf{E_0}$ photoelectron energy origin

EC ethylene carbonate

EDS energy-dispersive X-ray spectroscopy

EIS electrochemical impedance spectroscopy

ESRF European Synchrotron Radiation Facility

EV electric vehicle

FIB focused ion beam

FOV field of view

FY fluorescence yield

hard XAS hard X-ray absorption spectroscopy

ICP-OES inductively coupled plasma-optical emission spectroscopy

LAGP lithium aluminum germanium phosphate

LCO $LiCoO_2$

$\mathbf{Li_{0.3}NCA}$ $Li_{0.3}Ni_{0.8}Co_{0.15}Al_{0.05}O_2$

LIB lithium-ion battery

$\mathbf{LiBF_4}$ lithium tetrafluoroborate

LiBOB lithium bis(oxalato)borate

$LiFePO_4$ lithium iron phosphate

$LiMn_2O_4$ lithium manganese oxide

$LiPF_6$ lithium hexafluorophosphate

LiTFSI lithium bis(trifluoromethanesulfonyl)

LMB lithium-metal battery

LMO $LiMnO_2$

LNO $LiNiO_2$

LR-NMC Li-rich Ni-, Mn-, and Co-based layered oxide material

MLD molecular layer deposition

MPF mirror pitch feedback

NCA $LiNi_{1-x-y}Co_xAl_yO_2$

NiO nickel oxide

NMC $LiNi_{1-x-y}Mn_xCo_yO_2$

NMC532 $LiNi_{0.5}Mn_{0.3}Co_{0.2}O_2$

NMC622 $LiNi_{0.6}Mn_{0.2}Co_{0.2}O_2$

NMC811 $LiNi_{0.8}Mn_{0.1}Co_{0.1}O_2$

PAN poly(acrylonitrile)

PCL polycaprolactone

PEO poly(ethylene oxide)

PMMA poly(methyl methacrylate)

PS polystyrene

PVC poly(vinyl chloride)

SE solid electrolyte

SEM scanning electron microscopy

SN succinonitrile

SOC state-of-charge

soft XAS soft X-ray absorption spectroscopy

SPB solid polymer battery

SPE solid-polymer electrolyte

SSB solid-state battery

SSRL Stanford Synchrotron Radiation Lightsource

T-XRD temperature-controlled X-ray diffraction

T_g glass transition temperature

TEM transmission electron microscopy

TEY total electron yield

TGA-MS thermogravimetric analysis-mass spectrometry

TLD through-lens detector

TM transition metal

TWS Trainable Weka Segmentation

TXM transmission X-ray microscopy

VTF Vogel-Tamman-Fulcher

WEKA Waikato Environment for Knowledge Analysis

XANES X-ray absorption near edge structure

XRD X-ray diffraction

1 Introduction

The year 2019 marked a truly special year for the lithium-ion battery (LIB) with the Nobel Prize in Chemistry being jointly awarded to John B. Goodenough of the University of Texas at Austin, M. Stanley Whittingham of Binghamton University, and Akira Yoshino of Meijo University *'for the development of Li-ion batteries'*[iii]. First developed in the 1970s by Whittingham using metal dihalcogenides (TiS_2), LIBs laid the foundation of today's ever-present mobile consumer electronics [1], electric vehicles (EVs) [2], and the storage of renewable energy sources such as wind and solar [3].

With our society facing the consequences of climate change through the decade-long burning of fossil fuels, the pursuit of the utilization of renewable energy sources brings the need for the next-generation energy conversion and storage systems. Hence, lighter, cheaper, and more energy dense LIBs are needed to decarbonize transportation, and pave the way for an electrified mobility [1, 4, 5]. This quest of an electrified future is also reflected in the aggressive and ambitious U.S. Department of Energy (DoE) goals for 2022, or China's battery technology roadmap for the period 2020-2030 [6–8]. Hereby, the key performance parameters critical for the electrification of powertrains are price (in \$/kWh), energy density (expressed as specific (gravimetric) energy in Wh/kg or volumetric energy in Wh/l), and specific power (expressed in W/kg). The *EV Everywhere Grand Challenge* of the DoE is calling for LIB battery packs that are [6, 7]:

- Four times cheaper (\$500/kWh ⟶ \$125/kWh)
- Two times smaller in size (200 Wh/l ⟶ 400 Wh/l)
- More than two times lighter (100 Wh/kg ⟶ 250 Wh/kg)

[iii] The Royal Swedish Academy of Sciences (accessed 07/18/2020: https://www.nobelprize.org/prizes/chemistry/2019/popular-information).

- Five times more powerful (400 W/kg ⟶ 2000 W/kg)

These ambitious goals and driving ranges past the 300 miles (480 km) mark can only be accomplished with high-capacity cathode and anode materials [9], and novel 'beyond LIB' chemistries such as Li-air, Li-sulfur, and Li-metal [7]. However, for the majority of car manufacturers the cathode material of choice for the next-generation EVs are Ni-rich transition metal layered oxide materials, which are already being employed today: $\mathrm{LiNi_{1-x-y}Co_xAl_yO_2}$ (NCA) (with $\mathrm{x + y \leq 0.2}$) and $\mathrm{LiNi_{1-x-y}Mn_xCo_yO_2}$ (NMC) (with $\mathrm{x + y \leq 0.4}$) [9, 10]. Although the reasoning behind this is the technical maturity of the mentioned cathode materials [10], Ni-rich layered oxides still come with the culprit of being intrinsically instable at high potentials and a tendency to release oxygen. On the anode side, the unchallenged material of choice is still graphite, despite research efforts being devoted to silicon-based materials, Li-metal, or even anode-free Li-metal batteries. Especially Li metal, being lightweight and having a specific capacity of 3800 mAh/g [11], is a very promising substitute for the graphite/copper current collector assemblage. But the utilization of Li metal with the established, but highly flammable, liquid organic electrolytes is limited due to dendrite formation and potential thermal runaway upon shorting.

With this in mind, a key requirement for automotive LIBs becomes apparent - safety. If the above goals are to be achieved within the given timeline and without compromising the safety of LIBs, a unique and promising path is solid-state batteries (SSBs) that eliminate the flammable organic electrolyte and make it possible to utilize Li metal, therefore having high energy densities while also being safe [9]. However, while the superior mechanical stability of polymer- and ceramic-based solid electrolytes (SEs) poses a more rigid barrier to Li dendrite growth, SSBs still suffer from poor electrochemical performance issues [9, 12]. Nevertheless, since the attainment of SSBs, be it with SEs of polymeric, ceramic, or even compositional nature, would help to enable next-generation battery chemistries with high energy densities, long cycle lives, and without a compromise on safety, extensive research efforts have been focused on advancing this field.

Therefore, the presented thesis is devoted to the detailed study of degradation mechanisms in lithium-metal batteries (LMBs) paired with a solid-polymer electrolyte (SPE) and Ni-rich layered oxide cathodes, NCA in particular. The taken approach primarily utilizes advanced, synchrotron-based characterization methods in order to shed light on different aspects: (I) thermomechanical, (II) chemothermal, and (III) chemomechanical stability. In the first part, the thermal stability of delithiated NCA is investigated *in-situ* under thermal abuse conditions during continuous heating to 450 °C, which could locally evolve during operation because of large localized currents and self-heating effects. Emphasis is put on the microscopic morphology of the single particles and the critical temperatures at which the most significant changes are happening. In the second part, the long-term chemothermal stability of delithiated NCA is systematically investigated at relevant operating temperatures of polymer SSBs with *ex-situ* synchrotron hard and soft X-ray absorption spectroscopy. Specifically, the reduction of the Ni valence on a particle level, i.e., from surface to bulk, is studied and directly correlated to temperature, time, and the presence of polymeric electrolyte, i.e., poly(ethylene oxide) (PEO) or polycaprolactone (PCL), and/or Li salts, i.e., lithium tetrafluoroborate ($LiBF_4$) or lithium bis(trifluoromethanesulfonyl) (LiTFSI). In the last part, the focus is set on the mesoscale chemomechanical interplay that exists over a wide range of length scales (μm$-$mm) within the hierarchically structured SSB, and the morphological as well as valence heterogeneities within secondary NCA particles that are cycled in solid-polymer batteries.

Partial results of the presented work have been published in the *Journal of Materials Chemistry A* and *Chemistry of Materials* [13–15]. Any partially reused material from the original publications has been reproduced with the permission of the copyright holders *The Royal Society of Chemistry* and *American Chemical Society.*

2 Fundamentals

2.1 The Renaissance of Li Metal

With a density of 0.534 g cm^{-3} (at 20 °C), and a standard electrode potential of $E^0 = -3.045$ V vs. SHE [16], Li is not only the lightest of all metals, but also, paired with the right positive cathode material, allows to realize battery cells with high energy density. However, despite tremendous research efforts starting in the 1960s [17], and many LMB chemistries commercialized in the 1980s by Exxon, Duracell, Bell Labs, and MoLi [18], LMBs eventually moved into the background and had to be pulled out from the market [19, 20]. Several safety issues related to dendritic growth of Li, exothermic reactions between Li metal and electrolyte, and hence thermal runaways causing fire were the main cause for this [16, 18], but also the commercialization and success of the intercalation-based graphite/$LiCoO_2$ (LCO) battery in 1991 by Sony [16, 21].

Today, the dominating intercalation-based LIB technology is still based on a graphite negative electrode in combination with liquid organic carbonate electrolytes and a layered metal oxide material, thanks to the superior wetting of the solid electrodes by the liquid electrolyte and its high conductivities [22]. Nevertheless, there are several drawbacks to this technology: (I) insufficient thermal and electrochemical stabilities that lead to several safety incidents related to smartphones [23], and EVs [24], (II) an upper limit for the possible achievable energy content, due to the volume and weight of the host materials in which Li ions intercalate [25], and (III) oxidative instability at high cell voltages of the organic electrolyte are limiting factors in utilizing high-voltage cathodes [26, 27]. Therefore, replacing the liquid electrolyte with SEs, is a feasible way to overcome the existing problems of the current LIBs platform, while also enabling new battery chemistries [22]. In fact, a roughly 35-50% increase in specific energy and roughly 50-55% increase in volumetric energy density at the cell level are possible when replacing the graphite anode with Li metal [25, 28]. This has led to a rapidly growing interest in SEs and SSBs by both, academia and industry, reflected in an increased number of scientific studies [29, 30], big investments by industry, and a market size forecast of \$6 billion by 2030 [31]. Thanks to this recent effort, significant progress has been made for SSBs through optimization of SEs and advanced characterization approaches, which also led to multiple commercialization efforts by companies such as Toyota, Seeo, and QuantumScape, to name just a few [30], and ongoing investments into those companies, e.g., recently \$200 million by Volkswagen in QuantumScape [32].

2.2 Architecture and Processes in SSBs

Figure 1 schematically visualizes the internal architecture and processes in LIBs and SSBs. Similar to commercial LIBs, SSBs consist of an anode, electrolyte and cathode. The crucial difference between both battery architectures is that SSBs, such as LMBs, combine both, solid electrodes as well as solid electrolyte. As annotated in Figure 1, the SE also acts as a separator between both anode and cathode, however, this comes with the search for SEs that have ionic conductivities comparable with liquid electrolytic solutions, but also provide mechanical rigidity and a high electrochemical stability window [1, 30, 33]. In comparison to this, the commercially dominant LIB architecture utilizes solid electrodes with liquid electrolytic solutions that consist of Li salts, e.g., lithium hexafluorophosphate ($LiPF_6$), in a mixture of organic carbonates, e.g., dimethyl carbonate (DMC), ethylene carbonate (EC) etc. Hence, the makeup of SSBs is technically simpler and does not need liquid electrolytes and a porous separator since the SE is combining both functionalities, which also leads to less packaging requirements due to the absence of a liquid. In addition, Li metal, if used as an anode, cannot only replace graphite as an anode, but the entire graphite/current collector assemblage, reducing the number of components and the size of LMBs further [33].

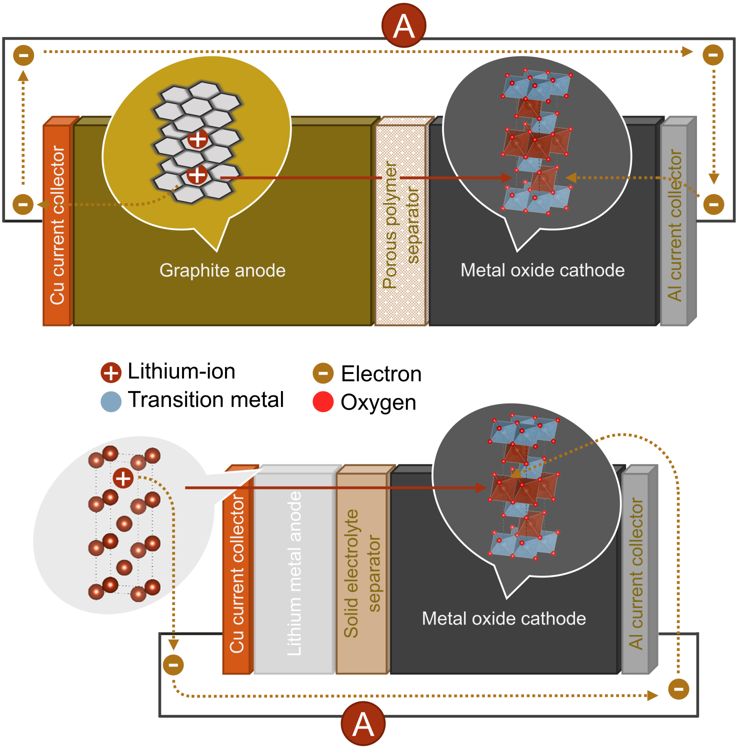

Figure 1: Architectural and conceptual comparison of typical LIBs (utilizing liquid organic electrolyte, top) and LMBs (utilizing a solid electrolyte, bottom) shown during discharge; dimensions of components representative of real LIBs and LMBs. Li ions deintercalate from the anode material and move through the separator to intercalate into the cathode crystal lattice, while electrons are transferred via an external circuit from anode to cathode. A NCA cathode structure is used to represent layered oxide cathodes. Li metal structure and polyhedral NCA structure drawn with VESTA 3 [34].

The working principle of SSBs is very similar to that in LIBs, both architectures are based on a shuttling of Li ions between two solid electrodes [30]. As indicated in Figure 1, during the discharge process, Li ions de-intercalate from the anode host structure, migrate across the electrode/electrolyte interface, and are transported via the electrolyte to the cathode side, where the ions move across the electrolyte/electrode interface and are finally intercalated into the cathode host structure (in Figure 1 into the NCA crystal lattice). At the same time, an electron transfer occurs via an external circuit from anode to cathode. Upon charge, Li ions de-intercalate from the metal oxide cathode and intercalate into the anode host structure, with electrons being transferred on an external circuit from cathode to anode. Hereby, the biggest variations between both architectures, LIBs and LMBs, are that (I) the graphite host structure is replaced by Li metal in LMBs, (II) the liquid electrolyte/porous separator in LIBs is replaced with a SE in LMBs, (III) the electrode/electrolyte and electrolyte/electrode interfaces at the anode and cathode side, respectively, are solid/liquid in the case of LIBs, and solid/solid in the case of LMBs.

2.3 Striving for Higher Energy Densities

2.3.1 Brief Description of the Concept of Energy Density

The energy density can either be expressed as specific (gravimetric) energy in Wh/kg or volumetric energy in Wh/l. The volumetric energy density is an important factor for many applications and especially critical for product design or when changing the anode from graphite to a volumetric smaller Li metal anode (see Figure 1). However, on the cathode side, due to similar crystal structures (layered oxides) and densities, volumetric energy density is a less significant figure for classical LIBs with graphite anodes, which is why the volumetric energy density is rarely reported in the literature. At the same time, reporting volumetric energy densities can be of advantage for all-solid-state batteries (ASSBs), which becomes conspicuous when taking a look at a recent analysis from Randau et al. of the performance of ASSBs [35], in which both specific energies as well as volumetric energies are reported.

Depending on the type of technical discussion, the energy density of LIBs can be interpreted at different ‘levels’. The theoretical achievable energy densities are usually context related and considered at either the material level, cell level, battery pack level, or system level [16]. Here it should be noted that the theoretical achievable energy densities usually do not directly translate into the practical achievable energy densities due to inconsideration of relevant parameters as has recently also been addressed by Betz et al [36], who plea for more transparency in the energy calculations within the battery community. For the aforementioned DoE battery pack goals of the *EV Everywhere Grand Challenge*, 250 Wh/kg at the battery pack level, would translate to roughly 325 Wh/kg at the cell level, and 800 Wh/kg at the materials level [37]. It is important to always refer to the considered level when talking about the energy density, which is not always done correctly in the literature due to insufficiently provided information, as reported by Berg et al [38]. In the following discussion, the energy density is always related to the cell level; it should be noted that for considerations of the energy density at the cell level, the masses of inactive materials like cell housing and separator are not included in the calculation. Simply put, the specific energy $\mathrm{E_{cell}}$ (in Wh/kg) of a LIB cell can be calculated as shown in Eq. 1 using the specific cell capacity $\mathrm{Q_{cell}}$ (in Ah/kg) and the nominal cell voltage $\mathrm{U_{cell}}$ (in V).

$$\mathrm{E_{cell}} = \mathrm{Q_{cell}} * \mathrm{U_{cell}} \tag{1}$$

Hereby, the specific cell capacity $\mathrm{Q_{cell}}$ is determined by the number of Li equivalents (n), the molecular weight M (in g/mol) of the limiting active material, and the Faraday constant (F = 96485 C/mol) as shown in Eq. 2. The cell voltage $\mathrm{U_{cell}}$ can be determined by the difference of the respective half-cell potentials as defined in Eq. 3:

$$\mathrm{Q_{cell}} = \left(\frac{\mathrm{F} * \mathrm{n}}{3600 * \mathrm{M}}\right) * 1000 \tag{2}$$

$$\mathrm{U_{cell}} = \mathrm{U_{cathode}} - \mathrm{U_{anode}} \tag{3}$$

From Eq. 1 one can see that to increase the specific energy of a LIB cell, either a higher cell voltage or improved specific capacities of the active materials are necessary. For the latter scenario, both cathode and anode capacities would have to be further matched in order to assure the cyclability of Li. Therefore, early on research effort has been devoted to develop high-voltage and high-capacity active materials.

2.3.2 Development in Recent Years

In the past 30 years, the technological progress for LIBs has come a long way in which the increase of the energy content was always the dominating factor. Figure 2 visualizes the incremental increase in gravimetric energy density after the initial commercialization of the LIB by Sony in 1991. Today, commercial LIBs can achieve gravimetric and volumetric energy densities of 250 Wh/kg and 700 Wh/l (at the cell level), respectively, with 247 Wh/kg cylindrical cells being implemented in the 2019 Tesla Model 3 [39]. When taking a close look at the recently reported highest specific energies for Li-based battery technologies in academic literature, one can see that significant progress has been made (yellow dots in Figure 2), and that all cells are based on Li metal anodes. As of July 2020, the highest specific energy (at the cell level) for a research

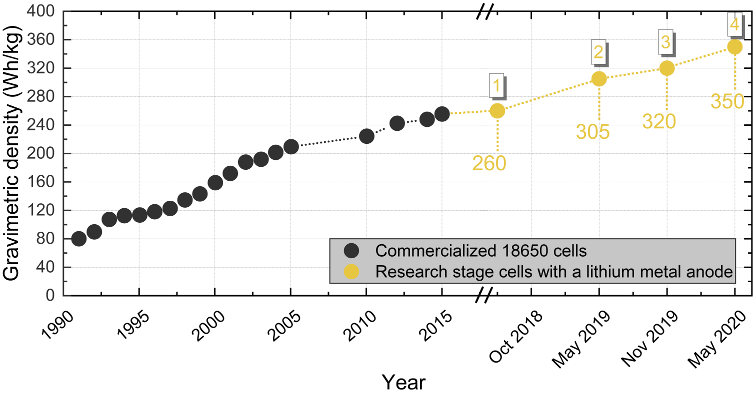

Figure 2: Development of the specific energy density of LIBs and LMBs after their commercialization in 1991. Specific energies until 2015 are based on commercialized cylindrical cells [28]. Values in yellow are for research stage LMBs cells of commercial relevance taken from references published by: (1) Korea Institute of Science and Technology [40], (2) Pacific Northwest National Laboratory [41], (3) Tsinghua University [42], and (4) Battery500 Consortium [43].

stage cell based on Li metal was reported by the Battery500 Consortium[iv] with 350 Wh/kg. Hereby the employed cathode material in all of those cells is based on Ni-rich NMCs such as $LiNi_{0.5}Mn_{0.3}Co_{0.2}O_2$ (NMC532), $LiNi_{0.6}Mn_{0.2}Co_{0.2}O_2$ (NMC622) or $LiNi_{0.8}Mn_{0.1}Co_{0.1}O_2$ (NMC811). Interestingly, the cathode material of commercial LIB batteries with the highest specific energies, all reported by Panasonic (last four black dots in Figure 2), are also based on Ni-rich layered oxides like NCA [44–46].

2.3.3 Layered Cathode Materials

Typically, intercalation-based positive electrode materials for LIBs are metal oxides with an olivine-, a spinel-, or a layered-type crystal structure (see Figure 3), where the Li-ion transport dimensionality is either 1D, 2D, or 3D, respectively. Here, the focus is set on layered-type cathode materials. Employing layered oxide materials for LIBs was first suggested

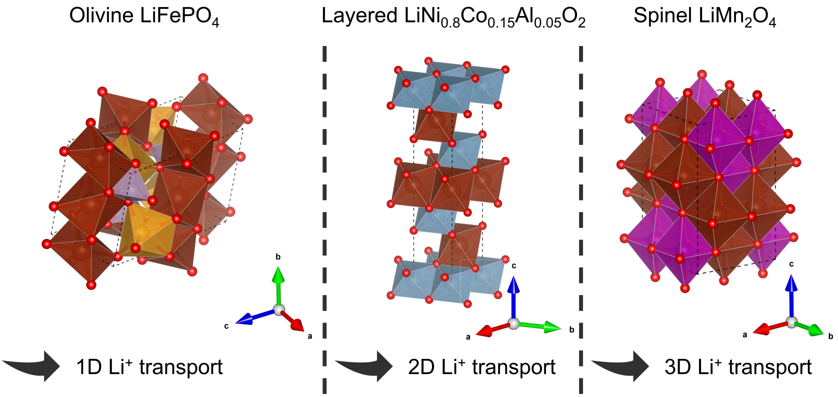

Figure 3: Crystal structure of three intercalation-based cathode materials, namely lithium iron phosphate ($LiFePO_4$), NCA, and lithium manganese oxide ($LiMn_2O_4$), with olivine, layered, and spinel structure, respectively.

[iv] Launched in 2017, the Battery500 Consortium is a multi-institution program with the aim to develop the next-generation LMB, consisting of national labs such as the Stanford National Accelerator Laboratory, and university collaborators such as Binghamton University, The University of Texas at Austin, etc.

and successfully implemented by M. Stanley Whittingham in 1976 using TiS_2 [47, 48]. The layered structure of TiS_2 comprises Ti and S sheets in a close-packed arrangement that allows for the intercalation of Li ions into the host material, without the breakage of a chemical bond during the charge and discharge of the battery. However, a small operating voltage (~2 V) and difficulties in finding practical electrolytes for this system quickly started the development of novel layered oxide materials, leading to LCO [49]. Patented in 1979, Goodenough's work on LCO and its favorable electrochemical properties such as high open circuit voltage and high Li-ion mobility due to the larger space between CoO_2 layers, made LCO the widest employed cathode material for LIBs embedded in portable electronic devices, even today [18, 49–51]. Despite its superior qualities, one major drawback of LCO is that only a small portion (140 mAh/g) of the theoretical capacity (274 mAh/g) can be utilized [5]. This low practical capacity is mainly due to structural instabilities at high cell potentials arising from a band overlap between $Co^{3+/4+}$:t_{2g} and O^{2-}:2p as seen in the depicted energy diagram in Figure 4. Ever

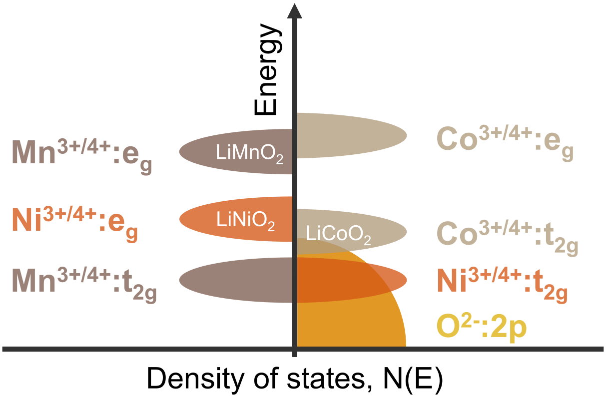

Figure 4: Redox energies of transition metal (TM) $Co^{3+/4+}$, $Ni^{3+/4+}$, and $Mn^{3+/4+}$ couples for $LiCoO_2$, $LiNiO_2$, and $LiMnO_2$, respectively. Redox energies are drawn relative to the O^{2-} p-band and are indicative of the chemical stability: the $Co^{3+/4+}$:t_{2g} band overlaps with the O^{2-}:2p band, while the $Ni^{3+/4+}$:e_g band barely touches the O^{2-}:2p band, and the $Mn^{3+/4+}$:e_g band lies way above the O^{2-}:2p band.

since the commercial success of LCO cathodes, a multitude of attempts have been made to find a suitable layered oxide material by replacing Co with other TMs, especially ones that minimize the overlap with the O^{2-}:2p band [5]. Along with this, Co itself is an expensive mineral (32.01 \$/kg[v]) mostly found in the Democratic Republic of Congo, but more importantly it is mined under harsh working conditions that raise human rights concerns [52]. Hence, due to its lower price (17.53 \$/kg[vi]) and lower toxicity Ni offers ecological and economical advantages in form of $LiNiO_2$ (LNO) [5, 53–55]. Furthermore, LNO is isostructural to LCO, i.e., crystallizing in the α-$NaFeO_2$ crystal structure (space group $R\bar{3}m$) [1, 55], and Ni^{3+} can be fully oxidized to Ni^{4+} without the loss of oxygen from the crystal lattice as for Co^{3+} [56], since the redox active e_g band only barely touches the O^{2-}:2p band, which makes high cell voltages, i.e., capacities, possible. LNO, however, has some major drawbacks. Mainly, a series of phase changes of LNO at different lithiation states [57–59], and a challenging synthesis procedure in which precursor Ni^{2+} ions end up in Li 3a-sites and therefore hinder Li diffusion [60], have obstructed the application of LNO as a cathode material. Like LCO and LNO, $LiMnO_2$ (LMO) also has been considered as a cathode active material, particularly because of its cost and ecological reasons [5]. However, in the case of LMO, the application as a cathode material is hindered due to poor cyclability as a result of a layered-to-spinel phase transition ($LiMn_2O_4$) [61]. With LCO, LNO, and LMO each being constricted by their respective shortcomings, and with comparable ionic radii of Ni, Co, and Mn, solid solutions of ternary layered oxides soon became a logical path forward (see compositional phase diagram shown in Figure 5) [62]. These mixed TM layered oxides (also NMC cathodes) are a way to combine the respective benefits of LNO (high capacity), LCO (rate capability), and LMO (stability) [63, 64].

2.3.3.1 Ni-rich Layered Oxides: NCA

---

[v] https://www.mining.com/markets/commodity/cobalt (accessed: 12/19/2020).

[vi] https://www.mining.com/markets/commodity/nickel (accessed: 12/19/2020).

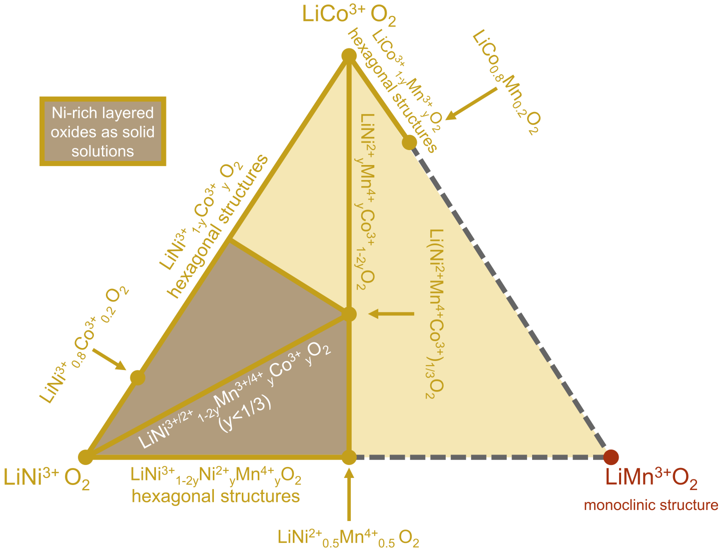

Figure 5: Compositional phase diagram of Li-stoichiometric layered TM oxides such as LCO, LNO, and LMO. Yellow solid lines represent solid solutions with hexagonal crystal structure, while black dashed lines represent immiscible/unstable compositions. Reproduced and edited with permission from He et al. [62].

With the push for even higher capacities and the possibility to oxidize Ni all the way to Ni^{4+}, in recent years, a significant amount of research work has been focused on Ni-rich mixed TM layered oxides that are derived from LNO [55, 56, 62, 65–68], and on overcoming the set of challenges for LNO. It was found that the presence of excess Ni^{2+} in Li 3a-sites, and the structural phase changes at high delithiation states can be suppressed by a small amount of Co and the addition of a redox inactive metal such as Al, respectively [54]. Determining the optimal amount of Co and Al for LNO through experimental work ultimately led to the optimal composition of $LiNi_{0.8}Co_{0.15}Al_{0.05}O_2$ (NCA) [68–71], with the main advantage of the structural stability at high states of delithiation [70, 72, 73]. The properties exhibited by this composition make NCA a good candidate for commercial batteries due to superior capacity retention upon cycling and hence found commercial application in EVs by Tesla, and by SAFT [55]. Besides NCA, the industry also has standardizing Ni-rich compositions of ternary layered NMC oxides, e.g., NMC622.

A recent study by Placke et al. showed how NCA-based cells have a significant advantage over, e.g., the classical LCO material, or the extensively researched Li-rich Ni-, Mn-, and Co-based layered oxide materials (LR-NMCs) [28]. By projecting the specific and volumetric energy densities of cells made up with one of the aforementioned cathode materials and either a Li metal, Si/C composite, or graphite anode, Placke et al. showed how the higher operating voltage and bulk density of NCA makes superior LIB electrode stacks possible (see Figure 6) [28]. Their calculations of energy densities for NCA electrode stacks clearly depict how the substitution of today's graphite negative electrode by Li metal would result in a roughly 50% and 55% gain in specific energy and energy density, respectively (also see section 2.2). Highest specific energies and energy densities were found for electrode stacks of Li/NCA and Si-C/NCA, respectively [25, 28]. Furthermore, the positive impact of a high-capacity anode such as Li on the energy density became even more obvious when same volumes are utilized as in currently employed commercial cylindrical batteries (see Figure 6d, where a 165 μm electrode thickness is used instead of 100 μm), leaving aside practical feasibility [28].

This clearly shows how Ni-rich cathodes like NCA and a Li metal could pave the way for the next-generation of energy-dense LMBs, given that the technical challenges, especially regarding Li metal safety and processability, could be overcome. One step towards this goal is polymer-based SEs. Eliminating the liquid organic electrolyte, replacing it by a polymer-based SE, and coupling this stack with a Ni-rich cathode such as NCA could help attain the next-generation batteries. Furthermore, with NCA being isostructural to commonly employed cathode materials such as LCO, and similarities in their general electronic structures, NCA is an ideal cathode reference material for investigating the intrinsic electro-

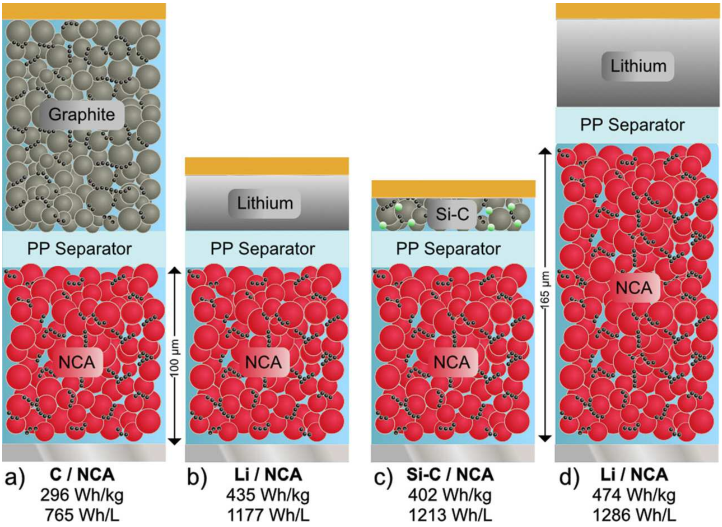

Figure 6: Specific and volumetric energy densities for various LIB electrode stacks: (a) C/NCA, (b) Li/NCA, (c) Si-C/NCA, and (d) a thick Li/NCA configuration. Reproduced with permission from Placke et al. [28].

chemistry of mixed TM layered oxides [74, 75]. The structural stability of NCA makes experimental isolation of the impact of delithiation from the effects of structural changes possible, and hence makes NCA an almost ideal system to study the intrinsic behavior of oxygen [75], and the degradation mechanisms for LMBs with a SPE, as done in this thesis.

2.3.3.2 Crystal Structure and Related Transitions

The operation as well as degradation of layered oxides involve transformations between their related layered (O1, O3, H1-3, etc.) and cubic (spinel, rocksalt) phases [76]. As briefly mentioned before, the crystallography of layered oxides is a rhombohedral structure (often referred to by its prototype structure α-$NaFeO_2$) with the space group $R\bar{3}m$ [1, 55]. In this, a close packed oxygen framework is formed in the fully lithiated state with an *ABCABC* stacking, also known as O3-type[vii] structure (see center panel of Figure 3) [76]. Here, TM and Li ions occupy the octahedral 3a and 3b sites, respectively. At high delithiation states an *ABAB* stacking known as O1 phase is preferred, with a possible hybrid H1-3 phase consisting of alternating blocks of O1 and O3 environments [76]. These transformations from O3 to O1 or H1-3 are first order phase transformations and appear as plateaus in the voltage vs. capacity curve, when the material is charged to high voltages [76]. Besides, irreversible structural transitions, induced by TM migration, are also possible between related cubic phases, i.e., spinel ($Fd\bar{3}m$) and rocksalt ($Fm\bar{3}m$). Particularly in a thermodynamically unstable, delithiated state (with respect to spinel and rocksalt phases), layered-to-spinel and layered-to-rocksalt transitions become possible [76].

2.3.3.3 Performance Decay and Intrinsic Instability

Despite their comprehensive advantages in terms of specific capacity, rate capability, operating potential, and cost [78, 79], Ni-rich layered oxides still face two essential problems: (I) performance decay over the lifetime, and (II) intrinsic (thermal) instability [80–82]. The performance decay often looms in form of fading capacity and voltage, and increased cell impedance, whereas the intrinsic instability can lead to safety hazards such as a thermal runaway [81, 83–85]. The origins of the performance and safety issues, related to the cathode active material, are often linked and can generally be narrowed down to the following (see graphical summary in Figure 7):

1. Ni/Li cation mixing (disordering)
2. Thermal decomposition and oxygen release

[vii] Introduced by Delmas et al. [77], this notation uses a letter indicating the intercalant coordination, e.g., (O)ctahedral or (T)etrahedral, followed by a number representing the number of layers in the repeat unit. For layered oxides of the form Li_xMO_2 the notation O1 would refer to octahedrally coordinated intercalants separated by a single MO_2 layer.

3. Layered-spinel-rocksalt phase transition
4. Microcracks of secondary particles
5. Residual Li components

Ni/Li cation mixing is a process in which TM ions such as Mn^{2+}, Co^{2+}, and in particular Ni^{2+} migrate into vacant Li^+ sites due to similar ionic radii of Ni^{2+} (0.69 Å) and Li^+ (0.76 Å) [68]. This effect leads to reduced capacity, reduced Li migration, and can induce the phase transition from layered over spinel to rocksalt [86–89]. Besides being a problem during synthesis (see section 2.3.3), cation mixing can occur over the whole lifetime of the battery, especially with increased Ni content and temperature [81]. Ni/Li cation mixing in Ni-rich layered oxides can be compared to a thermal decomposition and associated transition from the layered phase to the spinel/rocksalt phases (for details see Zhang et al. and Wang et al. [81, 90]). Therefore, suppressing cation mixing during synthesis [91], doping of cations and anions [92–94], and adopting surface coating strategies are crucial [95, 96].

Thermal decomposition and oxygen release can become a major issue in Ni-rich materials especially in a highly delithiated, i.e., overcharged, state [97]. In a highly delithiated state, Ni-rich cathode materials become unstable and hence are susceptible to thermal decomposition, leading to a breaking of TM-O bonds, release of oxygen, and subsequent chemo-mechanical breakdown via phase transition to a rocksalt phase over a spinel phase [86, 98, 99]. These degradations take particularly place at the interface of cathode/electrolyte [100–102]. The thermal instability and tendency to release oxygen is greater, the higher the Ni content of the cathode material is [86, 103]. For NCA, the onset of oxygen evolution was found to initiate at roughly 75-80% state-of-charge (SOC) [104]. In this process, most of the released oxygen instantaneously reacts with electrolyte compounds to produce CO and CO_2 as shown by Jung et al [105]. This leads to the dangerous accumulation of gases, pressure build-up, and further reduction of CO_2 on the anode to form Li_2CO_3, as suggested by Eq. 4 [106].

$$2\ \mathrm{CO_2} + 2\ \mathrm{Li^+} + 2\ \mathrm{e^-} \rightarrow \mathrm{Li_2CO_3} + \mathrm{CO} \tag{4}$$

$$\mathrm{Li_2CO_3} + \mathrm{LiPF_6} \rightarrow 2\ \mathrm{LiF} + \mathrm{LiPOF_4} + \mathrm{CO_2} \tag{5}$$

As described by Eq. 5, Li_2CO_3 can additionally react with electrolyte salts such as $LiPF_6$ to produce even more adverse CO_2 [97, 106].

Layered-spinel-rocksalt phase transition is ineluctable at high states of delithiation due to the strong thermodynamic driving forces exhibited by Ni-rich oxides to transform to spinel/rocksalt via cation rearrangement (migration and reduction) and oxygen release; only the kinetic limitations of these phase transitions make cyclability possible [76, 107]. The driving force scales with increased Ni content, SOC, and temperature [81]. At low SOC the layered-spinel-rocksalt phase transition takes place through disproportionation of Ni and subsequent oxygen evolution, while at high SOC the oxygen evolution is predominating [81, 108]. However, this process does not always cover the entire cathode particle and is more severe near the surface of particles, which can be explained by the kinetically hindered oxygen evolution in the bulk of the material [42]. In fact, the very surface of the cathode particles is in a more rocksalt-like phase while the subsurface is in a more spinel-like phase [100, 109]. This effect, often called ‘surface reconstruction’, has traditionally been seen as an undesirable process since it results in the formation of a thick and highly resistive surface layer, leading to increased cell impedance [76, 81]. A surface layer in a rocksalt phase effectively inhibits the motion of Li ions and is ionically blocking [110]. However, surface reconstruction layers sometimes are also seen to be critical to the success of layered oxide cathodes by forming a passivation layer, which may protect the cathode [76]. Nevertheless, recently it was also shown that the core of the particle can also undergo a phase transition to spinel/rocksalt [15, 111].

Microcracking of secondary particles, often along grain boundaries (intergranular), can contribute significantly to the performance loss of Ni-rich layered oxides [112, 113]. Although a recent trend towards single crystal

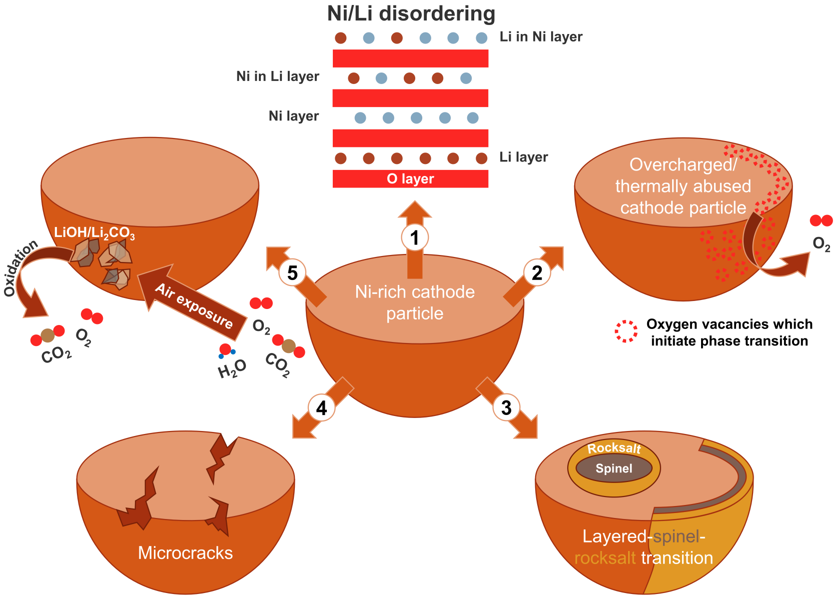

Figure 7: Overview of common degradation mechanisms in layered cathode materials. (1) Ni/Li cation mixing as a result of similar ionic radii. (2) Thermal decomposition via oxygen release at highly delithiated (overcharged) states. (3) Thermodynamically favored layered-spinel-rocksalt transition via cation rearrangement and oxygen evolution, with the rocksalt phase being Li diffusion limited. (4) Fracture development through repetitive (de-)intercalation and anisotropic lattice volume changes. (5) Undeterrable residual Li compounds leading to electrochemical reactions during cycling.

cathode materials has evolved [114–116], most of the currently employed cathode materials are polycrystalline in the form of spherical secondary particles that consist of many submicrometer-sized and densely packed primary particles (grains). This mesoscale architecture is susceptible to degradation mechanisms involving crack formation and decrepitation [113, 117–121]. Through the process of repeated (de-)intercalation of Li ions, intergranular fractures can develop along the grain boundaries of the primary particles upon electrochemical cycling. Often, this phenomenon is attributed to anisotropic crystal lattice volume changes [102, 122–125].

Models for Li intercalation suggest that fracturing can be driven by diffusion-induced stress, which increases with (de-)intercalation particle size and current density, as well as abrupt two-phase lattice constant changes [126–129]. Intergranular cracking can be observed already after a few cycles, [117, 122] and additionally intensifies as a function of the cycle number [124, 130], the upper cutoff voltage [131–133], operating temperature [121], C-rate [134] and storage time [135]. It can result in reduced electrical contact of active material and, thus, increased electrical resistance and aggravated side reactions like electrolyte decomposition and TM dissolution [117, 122, 136], due to the increase in exposed electrode surface area. These effects collectively expedite capacity fade and impedance rise in the cell.

Residual Li components such as LiOH and Li_2CO_3 are unavoidably present on the surface of Ni-rich cathode materials. Their presence can be traced back to excess LiOH used to compensate for Li loss at high temperatures during synthesis, and as a suppressor of the aforementioned Ni/Li disordering [137]. Furthermore, exposure to ambient conditions during storage/handling, and subsequent reaction with H_2O and O_2 also form residual Li components [81, 138–142], as described by Eq. 6 and 7 (conceptually shown for the base cathode material $LiNiO_2$). Additionally, Jung et al. and Sicklinger et al. have recently shown that not just LiOH and Li_2CO_3 residues, but also hydrated nickel carbonate-hydroxide, and basic nickel carbonate, in the form of $(NiCO_3)_2 \cdot (Ni(OH)_2)_3 \cdot 4H_2O$ and $NiCO_3 \cdot 2Ni(OH)_2 \cdot 2H_2O$, respectively, can be found on the surface of NMCs after ambient air exposure [142, 143].

$$\mathrm{LiNiO_2 + x\,H_2O \rightarrow Li_{1-x}H_xNiO + x\,LiOH} \tag{6}$$

$$\mathrm{2\,LiNiO + x\,H_2O + x\,CO_2 \rightarrow 2\,Li_{1-x}H_xNiO_2 + x\,Li_2CO_3} \tag{7}$$

Besides causing problems during electrode slurry preparations [81, 97], the presence of Li_2CO_3 exacerbates the cell gassing via electrochemical oxidation to O_2 and CO_2 at potentials > 4.3 V (vs. Li/Li^+), as depicted in Eq. 8 [81, 97].

$$\mathrm{Li_2CO_3} - 2\,\mathrm{e^-} \rightarrow 2\,\mathrm{Li^+} + \frac{1}{2}\,\mathrm{O_2} + \mathrm{CO_2} \tag{8}$$

2.4 Striving for Safer Batteries

As described in section 2.1 electrolytes for LIBs are conventionally non-aqueous, organic solvent-based mixtures containing a Li salt. However, mechanical, electrical, and thermal abuse conditions such as deformation, overcharging, and overheating, respectively, can lead to undesired thermal runaways with the potential of explosions and fire. Hence, addressing the mentioned challenges has gained much interest within the industry [31, 144]. The replacement of liquid electrolytes with SEs is very attractive, especially due to their decreased flammability [145], high operating temperature range, thermal stability, absence of leakage, and high resistance to shocks and vibrations [146]. Even though the thermal stability of SEs makes them very attractive for high temperature or other aggressive environments [147], it comes with several material development challenges such as a need for compatible and thermally stable electrode materials. Additionally, in order to perform as good as liquid electrolytes, Li-ion-conducting inorganic materials used for SSBs should have high ionic conductivities with ion transference numbers close to unity, wide voltage window and be easy to fabricate on a large scale with low cost [30].

2.4.1 Classes of Solid Electrolytes

There are mainly two classes of solid electrolyte materials that fulfill the needed requirements: (I) crystalline inorganic electrolytes such as ceramics (Garnet-type, Perovskite-type, NASICON etc.) or glass-based electrolytes including glassy and glass-ceramic systems made of oxides and sulfides [149], and (II) organic dry polymer electrolytes such as the Li-ion conductive PEO, also called SPEs (see Figure 8) [147]. A main difference between these classes is their elasticity; while ceramics have high elastic moduli making them useful for rigid battery designs, organic

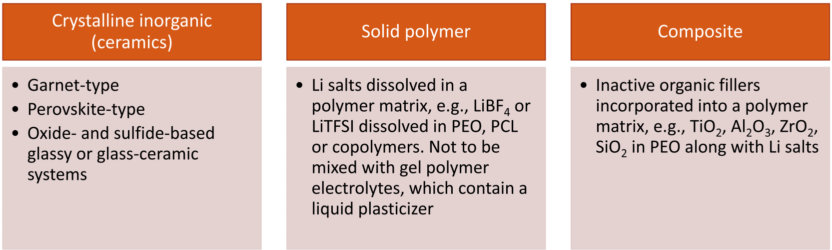

Crystalline inorganic (ceramics)	Solid polymer	Composite
• Garnet-type • Perovskite-type • Oxide- and sulfide-based glassy or glass-ceramic systems	• Li salts dissolved in a polymer matrix, e.g., $LiBF_4$ or LiTFSI dissolved in PEO, PCL or copolymers. Not to be mixed with gel polymer electrolytes, which contain a liquid plasticizer	• Inactive organic fillers incorporated into a polymer matrix, e.g., TiO_2, Al_2O_3, ZrO_2, SiO_2 in PEO along with Li salts

Figure 8: Classification of solid inorganic, polymer, and composite electrolytes for Li-ion batteries. For a more detailed classification, including liquid electrolytes, see Boaretto et al [148].

polymers have low elastic moduli making them useful for flexible battery designs [147, 150]. The latter is preferred, since it reduces the extent of fragmentation of the electrode materials [22].

The list of suitable SE materials complement each other and offer various advantages and disadvantages. For example, while ceramics show high conductivities at room temperature, organic polymer electrolytes such as PEO only have sufficient conductivities at elevated temperatures (70-80 °C). On the other hand, ceramic and glassy SE systems are often difficult to fabricate and come with expensive large-scale production costs, while it is easy to produce a polymeric large-area membrane [22]. When comparing the ionic conductivities, ceramic electrolytes possess high ionic conductivities and Li transference numbers close to unity ($t_{Li} \approx 1$) [151], while polymer electrolytes show low ionic conductivities with a low Li transference rate ($t_{Li} \approx 0.5$) [22, 152, 153]. To overcome these disadvantages, composite materials of ceramic and polymer electrolytes have been studied in recent years [12, 154–161]. Composite electrolytes show higher conductivities than dry polymer electrolytes, since the incorporation of ceramic fillers into the organic polymer host decreases the glass transition temperature (T_g) [162–164].

Commonly used polymer hosts are PEO, PCL, poly(vinyl chloride) (PVC), poly(methyl methacrylate) (PMMA), and poly(acrylonitrile) (PAN) [22].

Despite their lower ionic conductivity and Li transference rate, the advantages polymer electrolytes offer over ceramics, make them very interesting for SSBs.

2.4.2 Electrolytes Based on Block Copolymers

Among the different molecular polymer chains developed [165–167], PEO has become the benchmark SPE [168]. First proposed by Armand et al. in 1978 [169, 170], it has proven itself to be the most interesting SPE, because of its ether coordination sites, which allow for Li salt dissociation and complexation, while at the same time the flexibility of the backbone guarantees adequate ionic dynamics [171–173]. However, several studies have shown early on that the ionic transport depends closely on the segmental motion of the polymer chains (see Figure 9) [174–176], i.e., occurs mostly in the amorphous phase; LMBs incorporating a PEO electrolyte have therefore be operated at temperatures above the melting point of PEO (> 65 °C) [167, 173], with common operating temperatures being between 60-80 °C. At these temperatures the soft PEO polymer is a viscous liquid that is mechanically too weak to block the growth of Li metal dendrites upon cycling [173, 177, 178].

One way of increasing mechanical rigidity without compromising the ionic conductivity too much is the use PEO-containing block copolymers, which has been extensively studied in the literature [176, 179–183]. Block copolymers are formed of different covalently bound polymers where one block, A, provides the ionic conductivity, and the other block, B, provides other functionalities such as mechanical rigidity [167, 173, 176]. In particular, highly conducting polymer electrolytes based on block copolymers of polystyrene (PS) and PEO have been considered for electrochemical devices (see Figure 10) [166, 183–186]; these systems are further of great interest because of their self-assembly properties [173, 176, 183]. PS-PEO diblock copolymers doped with LiTFSI salt have been thoroughly studied by Balsara's group [176, 187, 188]. His group showed that with increased PEO chain length ionic conductivity also increases for symmetric diblock polymers, which is opposite to the behavior of a PEO homopolymer

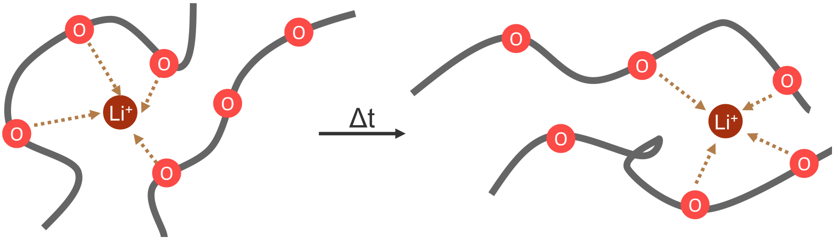

Figure 9: Schematic representation of the Li-ion conduction mechanism in PEO-based SPEs. The segmental rearrangement of polymer chains and concomitant change of the coordinating ligands result in a net forward motion of the lithium ion [26].

[173].

Copolymers based on PS and PEO have a unique lamella morphology resulting in a relatively high ionic conductivity of Li ions ($> 10^{-4}$ S/cm at 60 °C) and adequate mechanical properties at elevated temperatures [173, 184, 185]. Besides styrene, also alkyl (meth)acrylate derivates can be used as block B [189].

2.4.3 Brief Description of the Ion Conduction Mechanism

A preliminary necessity for the ion conduction in SPEs is the ability of the polymer matrix to dissolve/complex Li ions [165]. Hence utilized polymer chains should have sequential polar groups such as -O-, =O, -S-, or C=O [165, 183]. As briefly depicted in Figure 9 the polar groups of the polymer (shown for PEO polymer chains) forms a coordination complex around the Li ions; the motion of Li ions is assisted by the segmental motion and torsion around the C-C and C-O bonds of the polymer chain, which can be an intra- or inter-chain movement [191]. In a similar manner, ion clusters, made up of Li cations and Li salt anions, can also influence the Li ion movement [191, 192]. As mentioned previously, the ion conductivity for polymers is faster in the amorphous phase, i.e., above T_g. Besides segmental motion-assisted ionic conduction, ionic hopping-assisted ion transport is also possible in solid polymer batteries (SPBs) [166, 193, 194].

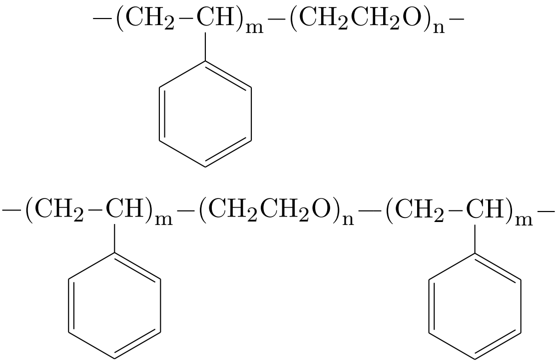

Figure 10: Chemical structures of a PS-PEO di- (top) and a PS-PEO-PS triblock (bottom) copolymers (m and n are the numbers of repeat units for the PS and PEO blocks, respectively). Block copolymers comprise two or more polymers linked together by covalent bonds. The immiscible polymer blocks induce a microphase-separation and self-assembly process that results in ordered block structures with periodically spaced domains [189, 190]. This way unique block copolymers with lamella morphology can be created.

The dependence of the ionic conductivity on the temperature follows two dominant conduction mechanisms: the Arrhenius-type and the Vogel-Tamman-Fulcher (VTF) type [165, 193, 195]. Ceramic or glassy materials show an Arrhenius-type temperature dependence of the conductivity as expressed in Eq. 9; with $\mathrm{E_a}$ being the activation energy (calculable from nonlinear least-squares fitting of the data from plots of log σ versus 1/T), and k the Boltzmann constant [165]. In these materials, ion transport occurs primarily via an ion hopping mechanism, which is decoupled from polymer chain motions, hence a linear behavior is expected in the conductivity vs. temperature graph [165, 193].

In SPBs or ionic liquids on the other hand, the curve is bent and is best expressed by the empirically derived VTF conduction mechanism expressed by Eq. 10; with σ_0 being a factor related to the number of charge carriers, B the pseudo-activation energy for the conductivity, and $\mathrm{T_0}$ the equilibrium $\mathrm{T_g}$, related to the kinetically measured $\mathrm{T_g}$ by $\mathrm{T_0} \cong \mathrm{T_g} - 50$ K [165, 193]. In SPBs a VTF behavior is usually observed above T_g [195].

$$\sigma = \sigma_0 \exp\left(-\frac{E_a}{kT}\right) \tag{9}$$

$$\sigma = \sigma_0 T^{-\frac{1}{2}} \exp\left(-\frac{B}{T - T_0}\right) \tag{10}$$

2.4.4 Seeo's Solid-polymer Battery Technology

The SPBs used within this thesis were based on the DryLyte technology developed by Seeo Inc., which enables energy-dense and safe SPBs (see Figure 11). First generation cells based on DryLyte solid polymer electrolyte offered specific energies of 220 Wh/kg [196, 197]. The latest generation of developed cells utilizing DryLyte is aiming at specific energies past the 300 Wh/kg mark and up to 400 Wh/kg, while offering high safety and long lifetime [196, 197]. The key attribute of the DryLyte solid-polymer technology is that it functions as both a mechanically rigid separator as well as electrolyte in order to allow the utilization of Li metal [196, 197].

A further key advantage of the DryLyte solid-polymer technology is that it allows the employment of a dual polymer electrolyte system in SPB cells. While the DryLyte solid-polymer layer acts as a separator and is made of a block copolymer, the so-called catholyte polymer, i.e., the polymer in which the cathode active material, Li salt, and conductive carbon is mixed, can be a completely different polymer. This dual electrolyte system allows the employment of different polymers on the cathode side, which enable the combination of a mechanically rigid and ionic conductive DryLyte separator with novel, high-voltage stable polymers on the cathode side [196, 197].

2.4.5 Deterioration Phenomena in SPBs and How to Overcome

For the practical application of SPBs, PEO, despite its low ionic conductivity at room temperature [165, 198], was believed to play a crucial part because of its low density, relatively good interface contact with the

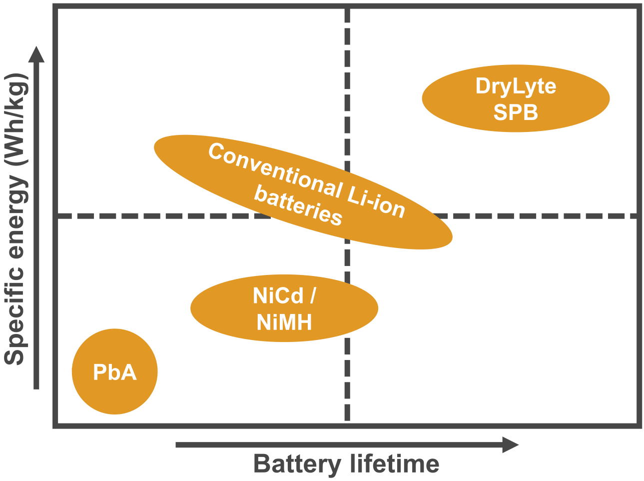

Figure 11: Comparison of specific energy and lifetime of different battery chemistries and SPBs enabled by DryLyte technology. Data for this graph obtained from Seeo Inc.

electrode, compatibility with Li metal, and also its good film forming probability [199–205]. Because of this most of the commercialized SPBs were built upon this technique. However, as briefly mentioned above, most of the commercialized SPBs have been utilizing low-voltage cathodes such as $LiFePO_4$, because the onset of the oxidative PEO decomposition was shown to be as low as 3.8 - 4.0 V (vs Li^+/Li) [199, 206–209]. Hence, the oxidative decomposition of PEO is often regarded as the main bottleneck for the application of Ni-rich cathodes such as NCA in SPBs, and detrimental when employing high-voltage cathode materials. Furthermore, the necessary elevated operating temperatures to overcome low ionic conductivity additionally narrow down the electrochemical stability window of SPBs [210, 211].

This oxidative decomposition of PEO takes place at the interface between cathode material and polymer electrolyte, which is why a lot of research has been devoted to stabilize and improve the interface between high-voltage, Ni-rich cathode materials and PEO-based electrolytes. Three

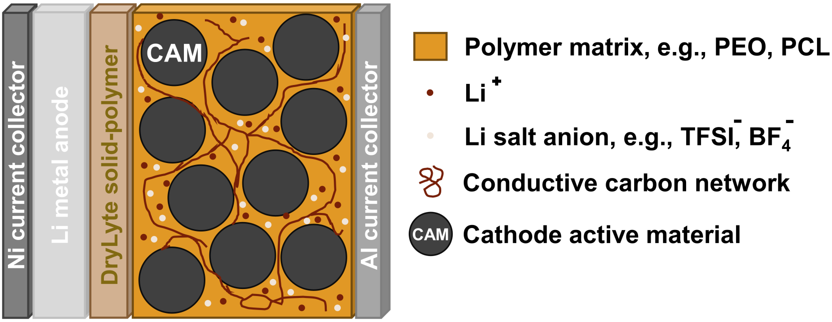

Figure 12: Structure of a solid-polymer cell with DryLyte. A 60 μm thick Li metal anode is sandwiched together with the DryLyte polymer film and a catholyte mixture made of a second polymer matrix that incorporates Li salt, conductive carbon, and the active cathode material that is coated on Al foil.

approaches to enhance this interfacial stability can be highlighted: (I) utilizing (ceramic) fillers, (II) coating the cathode active material, and (III) employing new polymer materials and Li salt matrices.

The utilization of (ceramic) fillers generally consists of a passive inorganic filler, e.g., Al_2O_3, SiO_2, ZrO_2, or lithium aluminum germanium phosphate (LAGP) embedded in an active polymer matrix [210, 212–215]. The synergy of the inorganic filler with the polymer matrix can enhance mechanical properties, interfacial stability, and increase ionic conductivity [167, 212]. Adding inorganic fillers can also modify local structures of polymer chains, decrease crystallinity, T_g, and be beneficial for the further dissociation of Li salts [215, 216]. Interfacial drawbacks can also be overcome using (oxide) surface coating layers on cathode materials, among others applied using atomic layer deposition (ALD) in order to control the exact layer thickness [198, 199, 217]. Further development of molecular layer deposition (MLD) has also made it possible to incorporate organic linkers or molecular fragments into the surface layer by eliminating the oxidizing precursor [217]. This way, not only inorganic (oxide) layers can be deposited, but also pure polymer films and organic-inorganic films [217]. Lastly, research on novel polymer/Li salt matrices has also been focused upon to advance the utilization of Ni-rich cathode materials in SPBs, whereby important new polymer materials have been developed as seen by a recent review by Lopez et al. [218]. PCL, to mention just one promising polymer material, has been considered early on as a very promising alternative for PEO [219, 220], and recently was demonstrated to have promising properties for the employment in SPBs [221, 222], especially when incorporated in form of block copolymers [222–224].

Besides all ongoing research effort, and plenty attempts being made towards combining (Ni-rich) high-voltage cathode materials such as LCO [198, 207, 217, 225], NMC [226, 227], $LiNi_{0.5}Mn_{1.5}O_2$ [228], in PEO-based SPBs [199], the exact origin of the electrochemical instability within SPBs has not yet been fully understood. Rarely studies focus on the influence of Li salts, which directly participate in the kinetic process of ion transfer and electrochemical reaction [210]; the addition of Li salts, often Lewis acids with moderate/strong acidity, can influence and trigger the degradation of the polymer matrix significantly [229]. LiTFSI, for instance, often utilized for PEO-based SPBs being beneficial in terms of solubility and ionic conductivity [167, 189, 218, 226, 230], has been shown to tend to decompose at the interface between polymer and cathode material [231]. However, due to the lack of focus on this matter, only very recently some light has been shed on the decomposition procedure and interaction of LiTFSI with the polymer matrix [199, 210]. Similarly, not much is known about the chemothermal stability of delithiated material in presence of certain polymers and/or Li salts, or the morphological-induced degradation on the particle level. Therefore, more research must be conducted on thermo-chemo-mechanical stability of SPBs in order to understanding this complex chemistry a little more.

3 Experimental Methods

3.1 Sample Preparation

3.1.1 Chemical Delithiation

Chemical delithiation has been widely used to prepare charged cathode active materials that are free of inactive components [232–238]. During the chemical delithiation process secondary cathode particles are uniformly exposed to the oxidant, avoiding any artifacts caused by heterogeneous electronic wiring and electrolyte wetting as would be when electrochemically oxidizing cathode active material embedded in an electrode [102]. While the delithiation process and Li distribution within the bulk and surface of the chemically delithiated samples can be different from electrochemically charged cathode materials in real electrodes, the process of chemical delithiation has been shown to result in a very similar delithiation state within the bulk and hence comparable SOCs [102]. Similarly, chemically delithiated NMC material was shown to be equivalent to electrochemically charged material [125].

Pristine NCA ($Li_1Ni_{0.8}Co_{0.15}Al_{0.05}O_2$), $LiNi_{0.6}Mn_{0.2}Co_{0.2}O_2$ (NMC622), and $LiNi_{0.8}Mn_{0.1}Co_{0.1}O_2$ (NMC811) cathode active materials of commercial grade were chemically delithiated to $Li_{0.3}Ni_{0.8}Co_{0.15}Al_{0.05}O_2$ ($Li_{0.3}$NCA), $Li_{0.3}$NMC622, and $Li_{0.3}$NMC811 through oxidation with a 0.1 M solution of nitronium tetrafluoroborate (NO_2BF_4) in acetonitrile for 24 hours in an Ar-filled glove box ($O_2 < 0.1$ ppm, $H_2O < 0.1$ ppm) at room temperature. In the following, the delithiation procedure is exemplary explained in detail for NCA (NMC622 and NMC811 were chemically delithiated in a similar fashion). Delithiated $Li_{0.3}$NCA powders were separated from the solution by filtering and centrifugation, and subsequently washed thoroughly with acetonitrile. Washed powders were dried overnight in a vacuum oven at room temperature. The Li ratio in NCA is governed by the ratio of NCA to NO_2BF_4 during the oxidation reaction (shown in Eq. 11).

$$\begin{gathered}\mathrm{Li_1Ni^{3+}_{0.8}Co^{3+}_{0.15}Al^{3+}_{0.05}O_2}\ (30\%) + \mathrm{NO_2BF_4}\ (70\%) \rightarrow \\ \mathrm{Li_{0.3}Ni^{3.875+}_{0.8}Co^{3+}_{0.15}Al^{3+}_{0.05}O_2} + \mathrm{Li_{0.7}BF_4} + \mathrm{NO_2}\uparrow\end{gathered} \tag{11}$$

The elemental stoichiometry was subsequently determined via inductively coupled plasma-optical emission spectroscopy (ICP-OES) (Thermo Scientifc™ iCAP™ 7000) to $\mathrm{Li_{0.3}Ni_{0.8}Co_{0.15}Al_{0.05}O_2}$. Phase purity and morphology were analyzed using X-ray diffraction (XRD) (Bruker D8 ADVANCE) and scanning electron microscopy (SEM) (JEOL JSM-7200F).

3.1.2 Preparation of NCA, Polymer, and Li Salt Blends

In an Ar-filled glovebox ($O_2 < 0.1$ ppm, $H_2O < 0.1$ ppm) $\mathrm{Li_{0.3}}$NCA was weighed into airtight, stainless steel coin cell cases, crimped, and subsequently double sealed in thermally stable pouches. Several batches for the individual sampling times were prepared. Similar to this, $\mathrm{Li_{0.3}}$NCA-Li salt compositions were prepared by first dissolving the respective Li salt in acetonitrile, and then adding delithiated NCA to the solution. The mixture was then vacuum dried in the glovebox antechamber, without exposing the material to air, and then weighed into airtight coin cells, crimped, and double sealed similar as described above. For $\mathrm{Li_{0.3}}$NCA-polymer and $\mathrm{Li_{0.3}}$NCA-polymer-Li salt mixtures, first the Li salt and/or polymer was dissolved in acetonitrile. The weight ratios of $\mathrm{Li_{0.3}}$NCA : polymer : Li salt was chosen to be exactly the same as used for the preparation of polymer cells (see section 3.1.3.1); $\mathrm{Li_{0.3}}$NCA : PEO : $\mathrm{LiBF_4}$, 77 : 20 : 3, wt%; $\mathrm{Li_{0.3}}$NCA : PEO : LiTFSI, 77 : 16 : 7, wt%; $\mathrm{Li_{0.3}}$NCA : PCL : $\mathrm{LiBF_4}$, 77 : 20 : 3, wt%. After full dissolution of the polymer and/or Li salt, delithiated NCA was added to the solution and in a final step, the solution was coated on Al foil. The coated sheet was then vacuum dried in the glovebox antechamber without exposure to air. A small disc was then punched and, similar as described above, crimped in an airtight coin cell case, and double sealed in a thermally stable pouch bag. Sealed samples were then transferred into temperature chambers outside of the glovebox and stored at 60, 80, or 90 °C and subsequently analyzed after certain storage times using soft L-edge XAS and hard K-edge XAS.

3.1.3 Cell Fabrication Procedure

3.1.3.1 Preparation of Polymer Cells

All solid-polymer cells as part of this work were manufactured on Seeo's facilities in Hayward (California, USA) utilizing their customized SPBs pilot production line (see Figure 13). Cost effective R&D-type pouch cells with a capacity of 50 to 100 mAh were used as a testing platform. The manufacturing process of the SPBs cells is very similar to the production process of conventional liquid electrolyte containing LIBs with a few differences: (I) no anode ink needs to be prepared and coated, since a Li metal anode is employed, (II) after coating the cathode on an Al current collector, a second coating of DryLyte is performed, (III) the liquid electrolyte filling step is omitted, since only solid-polymer is used, and (IV) a formation of the freshly built cells is not needed as for liquid electrolyte LIBs [196]. An overview of the electrode fabrication steps and the cell assembly is given in Figure 13b-c.

a) Electrode fabrication

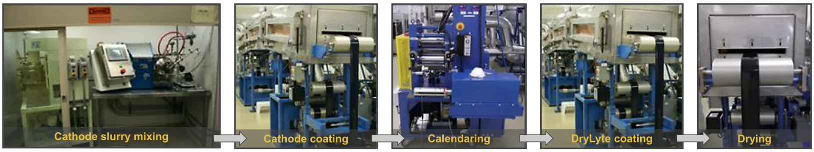

b) Cell assembly

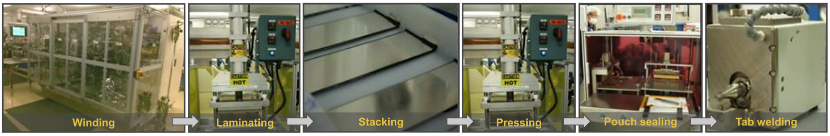

Figure 13: (a-b) Electrode fabrication and cell assembly overview of the pilot plant, which was used to manufacture all cells for this thesis. Utilized pictures taken by and courtesy of Seeo Inc.

Li//NCA-PEO and Li//NCA-PCL pouch cells were prepared as described in previous literature by the Balsara group and Seeo [187, 188, 239]. A DryLyte separator was used in combination with PEO or PCL binder (electrolyte), respectively. A common lab-scale procedure using PEO as the polymer matrix and LiTFSI is given in the following.

Commercial NCA cathode material and LiTFSI were dried overnight at 120 °C. The cathode solution was prepared by dissolving 23.06 g of PEO and 10.54 g LiTFSI in 321.46 g analysis grade cyclohexanone. 120 g of dried NCA and 6.4 g carbon black was then added to the mixture. The mixture was extensively mixed using a homogenizer for 45 minutes. The resulting slurry was immediately cast on carbon coated Al current collector foil and spread evenly using a doctor blade to achieve a loading of 4.5 mg/cm^2. The electrode was dried overnight under vacuum at 70 °C. Electrodes were punched into 10 cm^2 pieces and pressed on a DryLyte electrolyte film. A 60 μm Li metal anode was pressed on the other side of the DryLyte electrolyte. The cell stack was then assembled in a pouch cell with a Ni terminal on the negative electrode and an Al tab on the positive electrode. The pouch cell was then sealed in an Al-laminated pouch material using a vacuum sealer in a dry room for an air-free atmosphere.

3.1.3.2 Preparation of Liquid Cells

Li metal cells with liquid electrolyte were, except for the electrolyte, prepared with the same materials as used for the polymer cells, i.e., the same NCA material, same conductive carbon, and the same Li metal foil. The only difference to the solid-polymer counterpart was that battery-grade liquid standard electrolyte with 1.0 M $LiPF_6$ in EC:DMC:diethyl carbonate (DEC) (3:4:3, v/v), obtained from BASF, was used. Furthermore, liquid electrolyte containing cells were built with stainless steel coin cell cases and not in flexible pouch bags as for the solid-polymer cells.

3.1.4 Harvesting of Material from Cycled Cells

NCA particles were harvested from pristine, single-charged, and cycled cells. The polymer pouch cells were cut open using a ceramic knife in an Ar-filled glovebox ($O_2 < 0.1$ ppm and $H_2O < 0.1$ ppm). The metallic Li anode was carefully separated from the NCA cathode. Acetonitrile was used to dissolve and separate NCA particles from the solid-polymer electrode by centrifugation. After washing the harvested NCA cathode material several times with acetonitrile, the material was dried under vacuum for 48 hours and sealed and stored in an Ar-filled glovebox.

3.2 Electrochemical Characterization

Basic investigations of the components of LIBs and LMBs are typically carried out in various half-cell, full-cell, or symmetric-cell setups in either two-electrode or three-electrode configurations [240]. For example, full-cell setups in two-electrode configurations can be used to control the overall cell voltage, but not for monitoring single electrode potentials, whereas in a three-electrode configuration this would be possible[viii]. In the following only full-cell configurations of cells comprised of solid-polymer or liquid electrolyte were built since only the overall capacity fade and cyclability was to be determined.

3.2.1 Full-cell Cycling

The pouch cells were cycled with an Arbin BT2043 tester at 80 °C. Galvanostatic cycling was performed at a rate of C/6 referring to a practical capacity of NCA of 180 mAh/g between 3 and 4.2 V; this C-rate corresponds to a current density of 100 $\mu A/cm^2$. A stack pressure of 5 psi was applied during electrochemical cycling. No difference in electrochemical performance was found at higher stack pressures.

[viii] For an excellent overview about when to use which cell setup, for the electrochemical characterization of LIBs, see Nölle et al. [240].

3.2.2 Electrochemical Impedance Spectroscopy

Electrochemical impedance is usually measured by applying an alternating current (AC) potential to an electrochemical system (cell) and measuring the resulting AC current signal. The frequency dependence of the impedance can shed light on internal dynamic processes within the system.

A BioLogic VMP-300 potentiostat/galvanostat was used to carry out electrochemical impedance spectroscopy (EIS) measurements on full-cells prior to opening and harvesting of cycled cathode material. All measurements were carried out at 25 °C. To minimize differences coming from contact resistance, always the same channel with the same holder was used to collect EIS spectra. The applied frequency range was from 500 kHz to 10 mHz with a 10 mV AC amplitude.

3.3 Thermogravimetric Analysis-Mass Spectrometry

Thermogravimetric analysis-mass spectrometry (TGA-MS) is a thermal analysis technique. TGA isothermally measures the amount of weight change of a given sample as a function of temperature under a certain atmosphere, by carefully controlling the heating process and using a high precision balance. The resulting data provides information about phase transitions, absorption, desorption, and decomposition processes. Coupling it with a mass spectrometer and analyzing the evolving gases that leave the sample upon heating, additional information about the exact thermal behavior and sample decomposition can be obtained. TGA-MS was carried on a TA Instruments TGA 5500 instrument coupled to a TA Instruments Discovery benchtop quadrupole mass spectrometer for evolved gas analysis using 70% chemically delithiated NCA powder of the form $Li_{0.3}NCA$.

25.5 mg of delithiated NCA powder was weighed in a stainless steel crucible and transferred to the TGA-MS instrument with minimal exposure to ambient air. After sample insertion, the furnace was purged with Ar for 30 min at 25 °C to minimize trace amounts of ambient air during the measurement. The active material sample was heated from 25 °C to 450 °C at 10 °C min^{-1} with 10 min hold times at several discrete temperatures. The mass spectrometer was operated in multiple ion detection mode and recorded m/z of 2, 18, 19, 28, 32, 44 ions with a $<$ 10 s time resolution. Note that the $Li_{0.3}$NCA powder was stored in a glove box and the sample was transferred to the TGA-MS instrument in a closed container without exposure to ambient air.

3.4 Temperature-Controlled X-ray Diffraction

Temperature-controlled XRD can be used for *in-situ* investigations of phase transitions in tightly controlled temperature and/or humidity environments. Temperature-controlled XRD analysis was performed on a Panalytical X'Pert Pro diffractometer with monochromatized Cu K_α radiation equipped with an Anton Parr HTK 1200 hot stage. Scans were collected between 15 and 75° (2θ) at a rate of 0.0001° s^{-1} and a step size of 0.022°. Delithiated NCA powder was heated in air at a rate of 5 °C min^{-1} and the XRD patterns were recorded at a temperature step size of 50 °C with each temperature holding for 10 minutes before data collection.

3.5 Scanning Electron Microscopy Techniques

SEM is used for micro-morphological characterizations of various types of materials. A SEM by itself is capable of creating highly magnified images of materials using a focused beam of electrons. Atomic interactions by means of (in-)elastic scattering of the projected electrons with the target material result in secondary electrons providing micro-morphological insights into the material of interest. Very specialized techniques employing a broad ion beam (BIB) or focused ion beam (FIB) have become powerful tools providing cross-sectional information of entire specimen or even tomographic images of single cathode particles. Furthermore, coupling a SEM microscope with an energy-dispersive X-ray spectroscopy (EDS) detector results in unique instrument, capable of providing visual representation of the micro-morphology of the sample under investigation as well as the elemental composition.

3.5.1 SEM-EDS

SEM-EDS was conducted using a JEOL JSM-7200F Field Emission SEM equipped with an Oxford X-Max^{N} 50 Silicon Drift Detector system. SEM imaging was performed using an accelerating voltage of 5 kV at medium probe (5-7) currents using the secondary electron detector. EDS was conducted using an accelerating voltage of 20 kV at high probe currents (10-14).

3.5.2 BIB-SEM

Cross-sectional BIB-SEM imaging was utilized for pristine and cycled polymer cell cross sections of cells that were previously cut with a ceramic knife. A Hitachi High-Tech S-4800 microscope (accelerating voltage 1.5 kV) equipped with a Bruker AXS QUANTAX FlatQUAD System Xflash 5060FQ (accelerating voltage 5 kV) was used for this purpose. Prior to loading the specimen under an Ar gas atmosphere to the sample holder using an atmospherically isolated transfer vessel to prevent exposure to air, cross-sectional BIB milling was conducted using a JEOL IB-19520CCP.

3.5.3 FIB-SEM

FIB-SEM of delithiated and delithiated + heat-treated particles was performed using a Helios G4 dual-beam FIB. The heat treatment protocol was adjusted to be the same as used in the other experiments. Sectioning of particles was performed using gallium ions at 30 kV and imaging using electrons at 5 kV. The currents used for ion and electron beams were 26 pA and 0.1 nA, respectively. Secondary electron as well as back-scattered electron detectors were used for imaging. Serial-sectioning and SEM imaging was performed every 10 nm and the images were aligned and reconstructed to create a 3D volume of entire secondary particles.

3.6 Synchrotron Characterization Techniques

3.6.1 *Ex-situ* Soft and Hard XAS

Hard X-ray absorption spectroscopy (hard XAS) has been extensively used in materials science as well as in LIB research [241]. While the measurement of the TM K-edge can be useful to obtain information about bulk properties, its sensitivity to 3d electronic states of the TMs is less than the $L_{2,3}$-edges, which correspond to 2p-3d transitions [242]. More information on the 3d states can be obtained using surface dependent L-edge soft X-ray absorption spectroscopy (soft XAS). In comparison with hard XAS, the penetration depth of soft XAS is lower and strongly depends on the detection mode (see Figure 14). For example, while the auger electron yield (AEY) probes only the top 2 nm, the total electron yield (TEY) provides information up to 5 nm depth, and the fluorescence yield (FY) mode probes the subsurface, with a probing depth of about 50-100 nm [243, 244]. A combination of the bulk (K-edge) and surface (L-edge) analysis of TMs complement each other and provide insightful, depth-dependent information on the bulk and surface structure of secondary particles in cathode materials such as NCA. Due to the fairly large beam sizes (2 x 2 mm for soft XAS and 1 x 10 mm for hard XAS) the obtained picture of the nature of the samples is more accurate than techniques that focus on just a few particles [14].

As seen in Figure 14 (also see Figure 15a), Ni absorption edges in the soft XAS region result in two distinct peaks, L_3 and L_2, which correspond to transitions from the $2p_{3/2}$ and $2p_{1/2}$ orbitals into 3d orbitals, respectively. The nature of this splitting is related to the spin-orbit interaction of the core hole [245]. Further splitting into a multiplet structure of the L_3- and L_2-edges, as seen in Figure 14 and Figure 15, is due to crystal field effects and 2p-3d interactions [246]. The intensity ratio of the two peaks in the L_3-edge, namely $L_{3,\mathrm{high}}/L_{3,\mathrm{low}}$, is hereby proportional to the oxidation state of the absorbing species. To retrieve oxidation state information of the surface and subsurface, $L_{3,\mathrm{high}}/L_{3,\mathrm{low}}$ peak ratios are calculated and linked to reference standards with known oxidation states

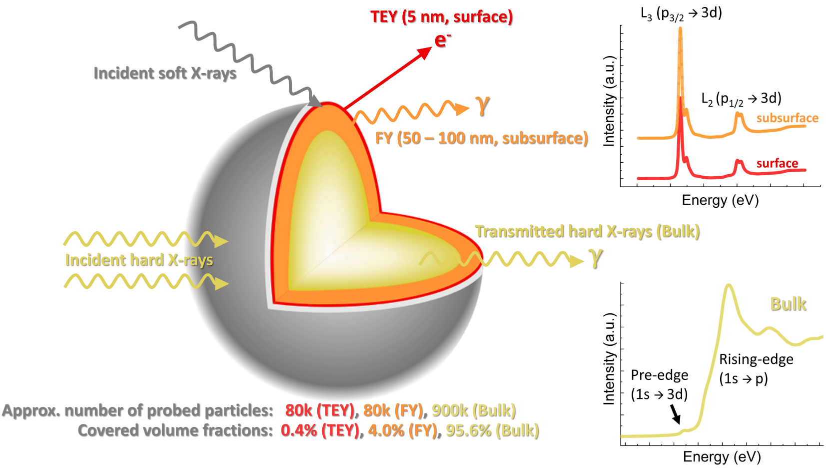

Figure 14: Schematic overview of soft and hard X-ray XAS. Soft X-rays (with energies of approx. 250-1200 eV) have a low penetration depth and are very surface-sensitive (up to 100 nm), hard X-rays (with energies > 5 keV) are bulk sensitive and traverse through the entire bulk material. This way, information on the oxidation state can be retrieved from the surface via soft XAS or the bulk via hard XAS.

and similar crystal structure (compare Figure 16a and b with Table 1) [247]. Examples for the change of the $L_{3,\mathrm{high}}/L_{3,\mathrm{low}}$ peak ratios are shown in Figure 15a for nickel oxide (NiO), pristine NCA, and chemically delithiated NCA, in which the Ni oxidation states are +2, +3, and +3.875, respectively. By relating $L_{3,\mathrm{high}}/L_{3,\mathrm{low}}$ peak ratios to reference substances with known Ni oxidation states, the $L_{3,\mathrm{high}}/L_{3,\mathrm{low}}$ peak ratio can be used to estimate the oxidation state of aged NCA samples. Hereby, a decrease in the ratio compared to the initial oxidation state is indicative of reduced Ni due to decomposition and possible oxygen loss.

In contrast to this, Ni absorption edges in the hard XAS region are a result of the excitation of metal 1s electrons into the continuum state or into valence orbitals [248]. In addition to the strong, dipole-allowed absorption edge containing information on the oxidation state of the absorbing metal, the absorption spectrum also contains a dipole-forbidden

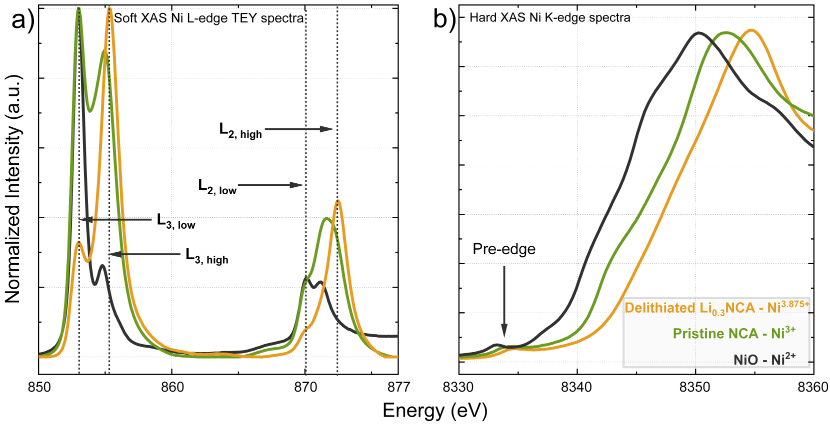

Figure 15: (a) Soft XAS derived TEY mode spectra for NiO (+2), pristine NCA (+3), and delithiated Li$_{0.3}$NCA (+3.875) showing the differences in the L$_3$ and L$_2$ peaks as a function of Ni oxidation state in the surface of the material. (b) Hard XAS absorption K-edge of the same substances show the bulk oxidation state dependency of the Ni K-edge.

transition of a metal 1s electron into a 3d orbital, resulting in a small but distinct pre-edge feature (see Figure 15b) [238, 249, 250]. The rising-edge is of particular interest, since it can be linked to the oxidation state of the absorbing TM species, i.e., shifts in the rising-edge absorption help to better understand oxidation state changes in the bulk material during aging and degradation [13, 15, 250–252]. As seen in Figure 15b and 16c, a higher Ni oxidation state leads to a higher K-edge absorption energy, i.e., shift to the right, than a lower Ni oxidation state, since the nucleus exhibits a stronger force on the remaining electrons. Additionally, the determined Ni oxidation state can then be used as a proxy for apparent oxidation state estimations as charge compensation comes primarily from the Ni in NCA, as reported in the literature [14, 253–255]. For this purpose, either the K-edge energy values for the top of the peak, the half-height of the rising edge at a normalized absorption value of 0.5. Or, as applied throughout this thesis, the K-edge energy values for the inflection point of the first derivative can be used and linked to the oxidation state [14, 255, 256].

Ni oxide	**Calculated Ni valence (in fully lithiated state)**
NiO	+2
NMC111	+2
NMC532	+2 2/5
NMC622	+2 2/3
NMC811	+2 7/8
NCA	+3

Table 1: Calculated Ni valence for different nickelates in the fully lithiated state, under the assumption, that cobalt is 3+ and manganese is 4+.

For soft XAS measurements, a thin layer of pristine NCA, as-prepared delithiated $Li_{0.3}NCA$ as well as all aged samples and standards (if powder), or a piece of 5 x 5 mm sample (if coated on Al foil) was spread or stuck onto a conductive carbon tape which was then attached to an Al sample holder inside an inert gas filled glove box. Measurements of the O K-edge, Co L-edge, and Ni L-edge were carried out at either the 33-pole, 1.27 Tesla wiggler beamline 10-1 or the bending magnet beamline 8-2 at the Stanford Synchrotron Radiation Lightsource (SSRL) with a spherical grating monochromator with 20 mm entrance spot. Data were collected at room temperature under ultrahigh vacuum (10^{-9} Torr), a 0.2 eV energy resolution and a 2 x 2 mm beam spot in a single load using TEY and FY detection modes.

Hard XAS data was collected in transmission mode using a Si (220) monochromator at SSRL beamline 2-2 and 4-1. Pristine NCA, as-prepared delithiated $Li_{0.3}NCA$ as well as all aged samples and standards (if powder) were dispersed on Kapton films for the measurements, while samples coated on Al foil were carefully transferred on Kapton films. Li//NCA-PEO polymer cells (pristine, single-charged, and cycled) were used as-prepared during the measurement. All sample handling was conducted in an Ar-filled glovebox ($O_2 < 0.1$ ppm, $H_2O < 0.1$ ppm).

Higher harmonics in the X-ray beam were rejected by detuning the Si (220) monochromator by 40% at the Ni K-edge. Energy calibration was accomplished using the first inflection points in the spectra of Ni metal foil reference at 8332.8 eV. X-ray absorption near edge structure (XANES) data were analyzed by Sam's Interface for XAS Package (SIXPACK) [257], with the photoelectron energy origin (E_0) determined by the first inflection point of the absorption edge jump. Prior to data acquisition, samples were mounted into a sample box with flowing inert gas.

3.6.2 Full-field Transmission X-ray Microscopy

Many X-ray (nano-) imaging and X-ray spectroscopic methods provide complementary data on the micro- and even nano-scale structure for hierarchically complex materials [258, 259]. While electron-based methods come with the benefit of atomic scale resolution, the advantage of X-ray (nano-) imaging techniques are increased X-ray penetration depth and the possibility of imaging thick samples, even in *in-situ* working conditions [259]. An X-ray imaging technique of particular interest is hereby transmission X-ray microscopy (TXM), which can be utilized with either soft or hard X-rays. In fact, TXM is employed at many research facilities around the world helping with material science as well as biomedical research questions [260]. Among others, possible benefits of synchrotron TXM (nano-) imaging include 3D tomography, absorption quantification, and chemical identification via X-ray fluorescence and XANES imaging [258]. In both, soft and hard TXM (for comparison see Table 2), the synchrotron X-rays can be utilized to not only get morphological data, but also XAS data, providing additional information about the chemistry [259]. Due to the capability of covering larger volumes in thick samples, especially hard X-ray-based high-resolution full-field transmission X-ray microscopy in 2D or 3D (2D-FF-TXM or 3D-FF-TXM, respectively), which can collect multiple pixel arrays with wide fields of view on the order of tens of microns, is used for energy material related studies [134, 241, 244, 259]. Especially the combination of TXM and XANES for chemical imaging and 3D nano-tomography, allows for

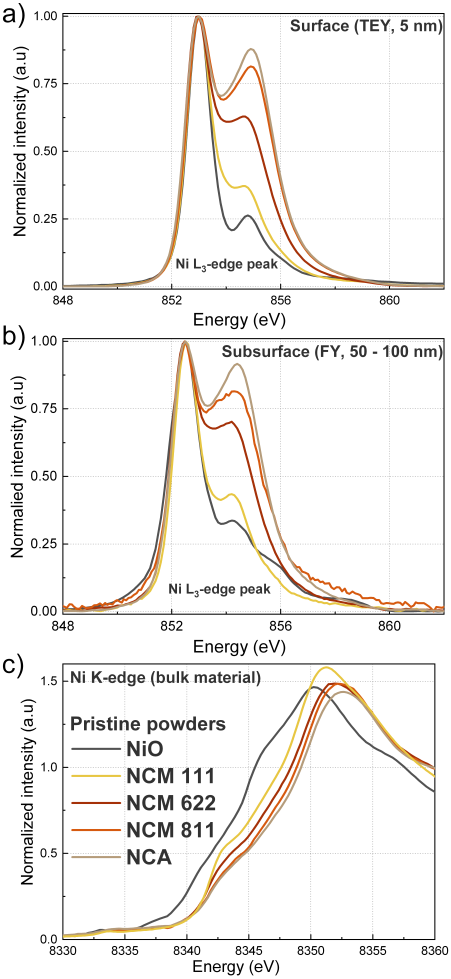

Figure 16: (a) and (b) Superimposed spectra of pristine Ni-rich oxides and NiO for TEY and FY mode (only L_3-edge shown here), respectively. $L_{3,\text{high}}/L_{3,\text{low}}$ peak ratios are proportional to average oxidation states of Ni. (c) Ni K-edge XANES spectra of pristine Ni-rich oxides and NiO. With increasing oxidation state of Ni, a shift towards higher energy values is observed.

in-situ mesoscale (nano-) imaging of complex, hierarchically structured functional materials, and provides new insights into the inerplay of morphology and chemical composition [259].

	Soft X-ray	Hard X-ray
Spatial resolution	10-30 nm	10-40 nm
Energy resolution	E/Δ=2500-7500	E/Δ=1000-10000
Energy range	200-2000 eV	4000-13000 eV
Data collection	Single energy	Single energy
Detection modes	Transmission Fluorescence Electron yield	Transmission Fluorescence
Sample thickness	50 nm-20 micron	100 nm-100 micron
Beam damage	High	Some

Table 2: Differences between soft/hard X-ray (nano-) imaging methods. Table adapted with permission from Andrews et al. [259].

A synchrotron TXM setup consists of a wiggler, mirrors, monochromators, condensers, zone plates and a charge-coupled device (CCD). At the SSRL beamline 6-2c, X-rays are generated via a 56-pole 0.9 Tesla wiggler, pass through a collimating mirror M_0 and a monochromator to tune the energy (operation range 2.1 keV to 17.0 keV) of the incident X-rays (see Figure 17) [258, 260]. After passing through another mirror (M_1) to focus the beam down to a few hundreds of microns, the X-rays pass through a mirror pitch feedback (MPF) system that stabilizes the beam coming out of the toroidal mirror M_1, and condenses it down to the sample of interest [260]. Finally, transmitted X-rays pass through a zoneplate system onto a Peltier-cooled CCD [260]. The FF-TXM (nano-) imaging techniques utilized for this thesis are 3D nano-tomography, which provides detailed information on the morphology, and 2D/3D XANES mapping to retrieve 2D/3D chemical phase maps for Ni via linear combination fitting to known references. A schematic overview of how maps and tomographic images are constructed via FF-TXM-XANES is given in Figure 18.

TXM imaging was performed at the described 56-pole wiggler beamline

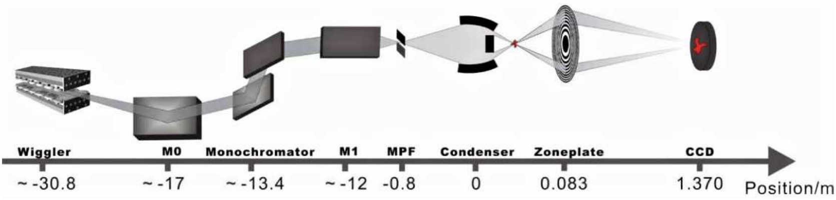

Figure 17: Schematic representation of the TXM setup installed at the SSRL beamline 6-2c. Reproduced with permission from Liu et al. [260] © The Optical Society.

6-2c at the SSRL. Sample powders were carefully dispersed in cylindrical quartz capillaries (100 μm in diameter and 10 μm in wall thickness) and carefully mounted to the beamline sample holder. Slow and steady He gas flow was applied to the capillaries to prevent air exposure; how the sample is introduced to the TXM experimental station can be seen in Figure 19. The X-ray energy was tuned to Ni K-edge and then focused onto the sample by an elliptically shaped capillary condenser providing illumination for a field of view (FOV) of approx. 30 x 30 μm^2. 2D transmission images (0.5 s exposure time, 5 repetitions, binning 2, 1024 x 1024 pixels) were collected from 8313 to 8394 eV with a minimum step size of 1 eV. This way a spatial resolution of roughly 30 nm can be achieved. To remove distortions caused by the flux and beam instabilities, concurrent acquisition of reference images at each energy was also performed through an open area of the sample (outside the capillary) with the same imaging configuration. The repetitions in exposures were carried out to enhance the dynamic range of the existing CCD and, subsequently, improve the signal to noise ratio in the data.

For the *in-situ* heated samples (see section 4), two-dimensional full-field transmission X-ray microscopy (2D-FF-TXM) images were first acquired at room temperature, upon heating, images were collected in 50 °C intervals from 100 °C to 350 °C and lastly at 450 °C.

For TXM imaging of cathode particles harvested from cycled polymer cells (see section 6), the 2D transmission images were collected from

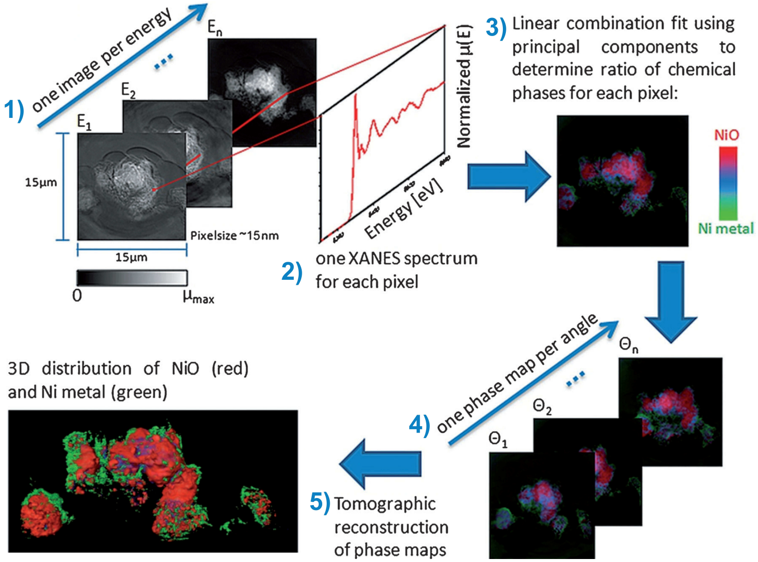

Figure 18: (1) One image is acquired in absorption contrast at each energy in the XANES scan. (2) XANES are constructed from each pixel plotting normalized absorption versus energy. (3) XANES from each pixel is fit to create a chemical phase map. (4) One phase map is generated at each angle in the tomographic scan. (5) The set of phase maps is used for tomographic reconstruction to retrieve three-dimensional chemical speciation. Reproduced with permission from Meirer et al. [261].

8100 to 8800 eV in 134 steps for each sample (0.5 s exposure time, 10 repetitions, binning 2, 1024 x 1024 pixels). Three-dimensional full-field transmission X-ray microscopy (3D-FF-TXM) tomography was performed by rotating the quartz capillaries from -90° to 90° with an angular step size of 1° and 58 different energy steps across the Ni K-edge. The tomographic reconstruction and data analysis were performed using TXM-Wizard. The effective 3D voxel size was 32.5 x 32.5 x 32.5 nm^3.

3.7 Data Processing and Plotting

Hard XAS raw data collected at beamline 2-2 and 4-1 at the SSRL facility was processed using the Demeter XAS Data Processing and Analysis

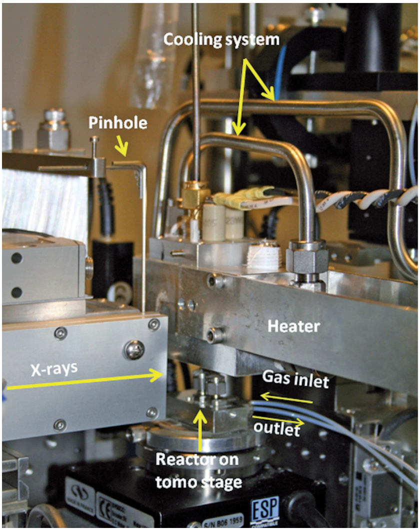

Figure 19: Overview of the *in-situ* TXM sample introduction setup installed at beamline 6-2c of SSRL at the SLAC National Accelerator Laboratory. Reproduced with permission from Andrews et al. [259].

software package comprised of the Athena, Artemis, and Hephaestus programs [262]. Additionally, Sam's Interface for XAS Package (SIXPACK) was also used to process and normalize hard XAS data [257].

Soft XAS raw data collected at beamline 10-1 at the SSRL facility was processed using the PyMCA (Python multichannel analyzer) software suite for the analysis of energy-dispersive X-ray spectra, developed by the Software Group of the European Synchrotron Radiation Facility (ESRF) [263].

TXM raw data collected at beamline 6-2c at the SSRL facility was processed using the TXM-Wizard program for advanced data collection and evaluation in full-field transmission X-ray microscopy [264].

Plotting of processed data was performed in the OriginPro software suite or Microsoft PowerPoint.

4 Thermomechanical Stability of NCA: Mesopore Formation and Oxygen Release

The current generation of Ni-rich layered oxides are primarily synthesized as spherical secondary particles comprising numerous densely packed primary grains (exemplary shown in Appendix Figure A.1) that are thermally unstable in their delithiated state. For example, a multitude of XRD studies have shown that the oxygen release upon heating in Ni-rich layered oxides takes place via a structural rearrangement of the material [86, 246, 250]. With rising temperature, the phase transition in layered oxides starts with a transition of the layered phase (R$\bar{3}$m) to a spinel phase (Fd$\bar{3}$m) and finally to a rocksalt phase (Fm$\bar{3}$m) [86, 250, 265], whereby more oxygen is released during the transition from the spinel phase to the rocksalt phase than for the first phase change from layered-to-spinel. Due to the hierarchically complex nature of the secondary particles, the aforementioned phase transitions can take place over a broad temperature range, whereby a coexisting of more than one phase, within the particles with heterogeneous spatial distributions, is possible. In addition, stresses due to repetitious Li (de-)intercalation, volume change due to the mentioned phase transition, and local heating also exist and can cause cracks (intergranular and intragranular).

Therefore, maintaining structural integrity of layered Ni-rich oxides is an essential factor that critically affects the performance and reliability of the operation of LIBs and LMB utilizing these cathode materials. It is of utmost importance to fully understand morphological changes happening upon thermal degradation of delithiated NCA in order to ensure the safe operation of the battery. Especially since prolonged operation involve repeated phase transformation, the build-up of mechanical stress, and the underlying structural and chemical complexity on the mesoscale could lead to very large local currents or provoke thermal spikes [244]. Moreover, the elevated operating temperature SPBs are subjected to

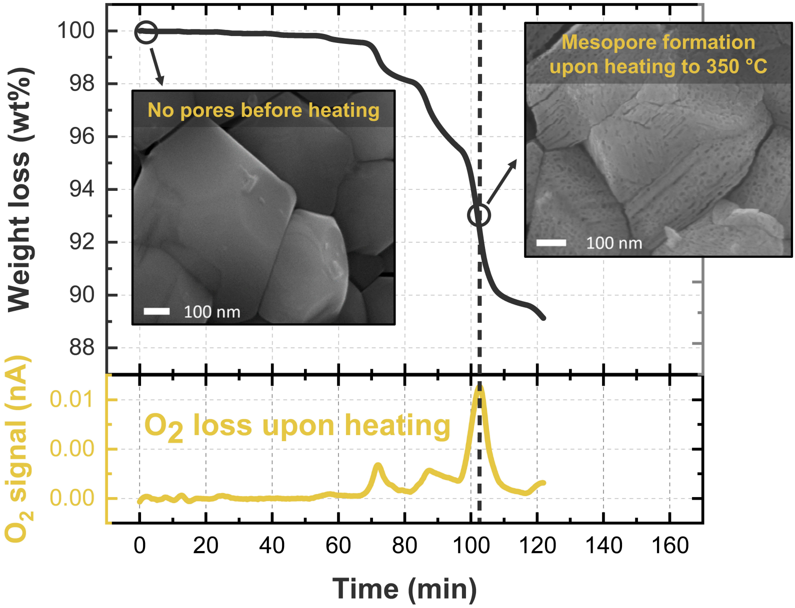

Figure 20: Overview of the oxygen evolution and mesopore formation observed for delithiated NCA upon heating from 25 °C to 450 °C (10 °C/min rate, 50 °C increments). Biggest mass loss correlates with a major oxygen release and mesopore formation.

make charged, i.e., delithiated, cathode materials incorporated into SPBs more prone to thermal decomposition and morphological changes, as has been also shown in the literature [211], wherefore it is crucial to understand when and where exactly the phase transitioning, oxygen evolution and concomitant reduction of Ni is happening on the single particle level.

To understand the sophisticated thermomechanical stability of delithiated NCA material on a single particle level, and shed light on the oxygen evolution that accompanies the structural changes, in this chapter the thermal decomposition, cracking and oxygen evolution of chemically delithiated $Li_{0.3}$NCA particles are systematically investigated upon heating from 20 to 450 °C. The multitude of simultaneous influences on the secondary NCA particle morphology during electrochemical cycling is simplified by investigating only the isolated temperature effect on the materials' morphology in absence of any electrochemical activity. This is conducted at temperatures that could be locally reached within the cathode due to localized currents, thermal spikes, or self-heating of formed Li dendrites [244, 266]. The results suggest that the delithiated NCA material undergoes a complex structural and chemical evolution at elevated temperatures via a continuous reduction of the Ni oxidation state, the release of oxygen, and phase transformation. However, most importantly, the release of oxygen also creates numerous mesopores throughout the analyzed particles, which is a new contribution to the literature and has not been reported yet. In addition, intergranular and intragranular fracturing at elevated temperatures are also found to possibly contribute to the degradation of the NCA cathode under these conditions.

4.1 Phase Transformations and Onset of Oxygen Evolution

To characterize and study the onset of the phase transformation and concomitant oxygen evolution, *in-situ* temperature-controlled X-ray diffraction (T-XRD) and TGA-MS were conducted using 70% chemically delithiated NCA material, i.e., $Li_{0.3}$NCA. For both techniques, freshly prepared $Li_{0.3}$NCA was used without any addition of polymer electrolyte, conductive carbon additive or Li salt. The exclusion of any electrode components other than the cathode active material allow the analysis of the thermal behavior of $Li_{0.3}$NCA alone, and avoid complications from the contributions of other electrode components.

The absolute thermal behavior of $Li_{0.3}$NCA is shown in Figure 21 using *in-situ* temperature-controlled XRD, which allows to obtain information on the thermal stress-dependent structural changes happening in the bulk material. The XRD patterns shown here were retrieved from $Li_{0.3}$NCA that was continuously heated to 450 °C (10 °C/min rate, 50 °C increments, 10 min hold at each temperature setting) and subsequently cooled to 25 °C (for the exact temperature profile see section 3.4). In good agreement with XRD data reported in the literature [246, 250, 267], no significant changes to the rhombohedral structure ($R\bar{3}m$, black) of NCA were observed below a temperature of 150 °C. Upon further heating past 150 °C, a layered-to-spinel phase transition ($R\bar{3}m \rightarrow Fd\bar{3}m$) is initiated that starts at about 200 °C and is completed at about 300 °C. The layered-to-spinel transition is indicated by the conjoining of (108) and (110) peaks and the accompanying reduction in the peak intensity ratio for the diffraction pair (003) and (104) of the rhombohedral structure as depicted in Figure 21. The observed changes suggest that significant migration of the TMs (Ni, Co, and Al) from the TM layer to the Li layer has taken place upon heating to about 250 to 300 °C. Subsequently, a second phase transitioning from the spinel to the NiO-type rocksalt phase ($Fd\bar{3}m \rightarrow Fm\bar{3}m$) takes place at temperatures above 300 °C. This can be noted by the decrease in $(311)_s$ and $(511)_s$ diffraction peak intensities. The intensities of the spinel phase peaks reached a maximum at about 300 °C, then declined to a very low level at 450 °C indicating that the spinel-to-rocksalt phase transition continued until 450 °C under these conditions. However, a strong reduction in the diffraction peaks of $(511)_s$ and the inversion of the peak ratio for the $(311)_s$ and $(222)_s$ peaks when heating from 300 to 350 °C indicate that the rocksalt phase is overtaking the presence of the spinel phase in the bulk material.

Gas evolution related to the phase transition in $Li_{0.3}NCA$ was analyzed in a similar manner as for T-XRD. $Li_{0.3}NCA$ in absence of any polymer, conductive carbon or Li salt was heated from room temperature to 450 °C as described in section 3.3. Figure 22 visualizes the associated mass loss (black) along with the utilized heating profile (grey), and the evolution of relevant gases like H_2O, O_2, and CO_2 (blue, orange, and brown, respectively). Overall, the sample lost approximately 10 wt% of its initial mass during heating to 450 °C. The mass spectrometry data reveals that the weight loss mainly coincides with the evolution of O_2 gas. At the transition from 200 to 250 °C and 250 to 300 °C only minor

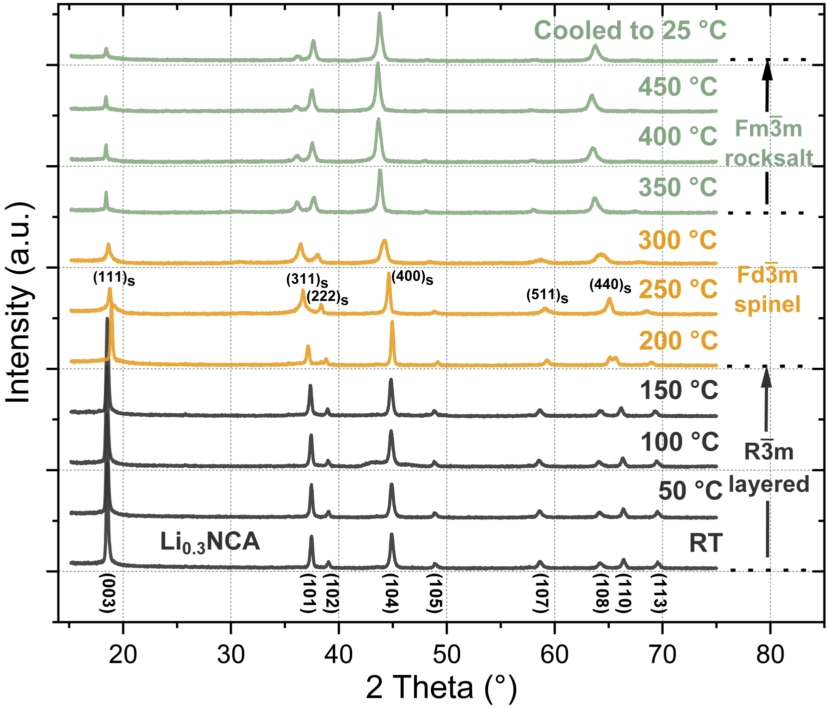

Figure 21: *In-situ* temperature-controlled XRD patterns of $Li_{0.3}$NCA upon heating. $Li_{0.3}$NCA was heated from 25 °C to 450 °C in 50 °C increments and a 10 °C rate. At each increment, the temperature was held to collect the corresponding XRD spectrum. Visible peak ratio variations and shifts indicate a phase transformation from layered (R$\bar{3}$m, black) to spinel (Fd$\bar{3}$m, orange) and spinel to NiO-type rocksalt (Fm$\bar{3}$m, green).

quantities of O_2 and H_2O are released, which account for 1.5 and 2.0 wt% mass loss, respectively, and are correlated to the layered-to-spinel phase transition. The majority of O_2 gas is released at the transition from 300 to 400 °C. This major O_2 evolution corresponds to a weight loss of approximately 6 wt% of the sample mass. Due to the absence of other mass signals in this temperature range this mass loss can be quantified very precisely. It is important to note that only little H_2O is released, mainly at a transition from 200 to 300 °C, with the majority being released at around 300 to 350 °C, and no water release at 100 °C.

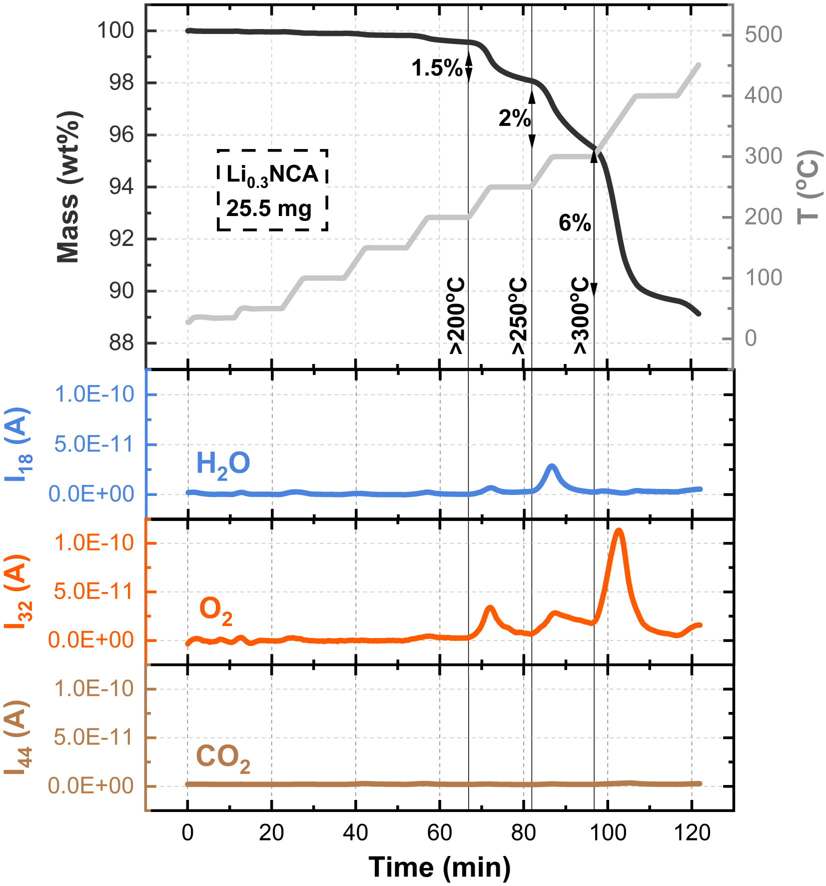

Figure 22: Gas evolution analyzed for $Li_{0.3}NCA$. $Li_{0.3}NCA$ samples were heated to 300 °C in 50 °C steps with a 10 °C/min rate (grey). Temperature was hold for 10 minutes at each step. After reaching 300 °C, samples were heated in 100 °C steps up to 450 °C. Sample mass loss (black) and evolution of H_2O, O_2 and CO_2 gases (blue, orange, and brown, respectively) were monitored during the heating process.

4.2 Chemical Phase Changes in Surface and Bulk

4.2.1 Soft and Hard XAS

Although T-XRD and TGA-MS give a very good insight into the bulk changes within the crystal structure, the phase transitions during thermal stress, and the concomitant release of oxygen, information on the local chemical changes and contributions of the Ni oxidation state to the observed phase transitions during thermal stress cannot be obtained this way.

Therefore, soft and hard XAS were applied to analyze the oxidation state changes happening in surface, subsurface, and bulk before and after subjecting $Li_{0.3}NCA$ to thermal stress, using the TM L-edge and K-edge XANES spectra. The TM L-edge spectrum (for Ni and Co) are based on dipole allowed transitions starting at the $p_{1/2}$ and $p_{3/2}$ energy levels into the empty 3d orbitals (eg*), and is, due to spin-orbit coupling of the core hole, split into two well separated energy bands namely, the L_3 edge ($2p_{3/2}$) and the L_2 edge ($2p_{1/2}$). Further, 2p-3d interactions and crystal field effects result in an additional splitting of these bands into a multiplet structures (for more details see section 3.6.1). Notably, the oxygen K-edge spectrum shows a transition from the O 1s core orbital to the unoccupied O 2p orbital [268], but the O K-edge XANES spectrum also reflects an unoccupied O 2p orbital character hybridized with TM 3d and 4sp orbitals [268–271]. This difference is important in understanding the variations between O K-edge, TM L-edge and TMs K-edge data.

Figure 23a shows the normalized O K-edge, Co L-edge, and Ni L-edge soft XAS spectra (left, middle, right panel, respectively). All constituents of NCA, where a change upon delithiation or heat treatment is expected, were subjected to a surface and subsurface oxidation state analysis using soft XAS, with an emphasis on the Ni oxidation state as the main charge compensator upon (de-)intercalation [272]. The changes upon chemical delithiation of NCA, resulting in 70% delithiated NCA, i.e., $Li_{0.3}NCA$ (orange), were compared with pristine NCA (black) and $Li_{0.3}NCA$ that underwent a similar heat treatment (blue) as described in section 4.1.

Comparing the soft XAS spectra, significant changes, in both, the surface and subsurface regions, were observed for the O K-edge and Ni L-edge spectra upon heat treatment. The O K-edge spectra of $Li_{0.3}$NCA before and after heat treatment is comprised of an intense absorption peak around 527.2 eV, which is associated with the lattice oxygen (metal-oxygen bond) in the layered oxide (oxygen 1s → metal 3d orbitals hybridized with O 2p). The broad peak features above 534 eV correspond to the O 2p → Ni 4sp transitions and other empty orbitals in this energy region. Moreover, the TEY spectra for pristine NCA showed another peak observed at 532.3 eV (marked with an asterisk), that is not observed in the FY spectra for the subsurface region of pristine NCA. Similar to the O K-edge spectra, notable changes were also observed for Ni L-edge spectrum before and after delithiation and also after heat treatment of $Li_{0.3}$NCA. First, an inversion of the L_3-edge ratio is visible (compare black and orange curves) in TEY- as well as FY-mode soft XAS. This is expected upon delithiation of pristine NCA, since the delithiation is oxidizing the Ni substantially (from 3+ to 3.875+). Upon heat treatment, this ratio changes again indicating a strong reduction for both the surface and subsurface. The change in L_3-ratio upon delithiation and subsequent heat treatment is depicted in Appendix Figure A.2b, and shows Ni oxidation state reduction at both probing depths. In order to quantify this reduction, several Ni containing oxide standards, namely NiO, NMC111, NMC622, NMC811, and NCA, were measured in a similar manner. The respective oxidation states of each standard was subsequently linked to the calculated $L_{3,\mathrm{high}}/L_{3,\mathrm{low}}$-ratio (see Appendix Figure A.3). After linear interpolation and fitting of the L_3-edge ratios to the oxidation states, the resulting correlation allowed to estimate the oxidation state of Ni in $Li_{0.3}$NCA heat-treated to 450 °C to 2.06+. In contrast to the O K-edge and Ni L-edge soft XAS spectra, the Co L-edge only showed very minimal changes happening within the surface and subsurface regions in $Li_{0.3}$NCA and heat-treated $Li_{0.3}$NCA samples. Only a small shoulder left of the L_3-peak in the TEY- and FY-mode spectra (marked with a plus sign in the middle panel of Figure 23a) indicates a slight reduction of the surface and subsurface Co^{3+} to Co^{2+}.

The oxidation state changes in the bulk were compared using Ni and Co K-edge hard XAS, which correlates the changes in the absorption edge to the changes in the average oxidation state of the absorbing atoms in the bulk material as described in the literature [250, 252, 273]. With Ni being the main charge compensator [272], the significant changes between pristine NCA, as-prepared $Li_{0.3}NCA$, and heat-treated $Li_{0.3}NCA$ were observed for the Ni K-edge. The Co K-edge, similar to the surface and subsurface, only showed little signs of redox activity for the bulk. The normalized Co and Ni K-edge XANES spectra for pristine NCA (black), $Li_{0.3}NCA$ (orange), and heat-treated $Li_{0.3}NCA$ (blue) as well as NiO (green), which is shown as a reference, are visualized in Figure 23b. In hard K-edge XAS, a forward shift to higher edge energies (in eV) indicates an increased oxidation state of the atom absorbing nucleus. Since the core electrons are more strongly bound to the nucleus in an oxidized state, their photo-ionization requires higher photon energies. In contrast to this, a shift to lower edge energies indicates a decreased oxidation state or reduction. The entire Ni K-edge clearly shifts from higher to lower energies in the order of as-prepared $Li_{0.3}NCA$, pristine NCA, and heat-treated $Li_{0.3}NCA$, indicating a strong reduction in the Ni oxidation state upon heating. This strong edge shift (2.97 eV) between as-prepared $Li_{0.3}NCA$ and heat-treated $Li_{0.3}NCA$ illustrates that the average oxidation state of Ni decreases significantly. Using the edge position defined by the photoelectron energy origin (E_0) [238], changes happening between the samples can be quantified and linked to oxidation states when proper references are used for correct oxidation states. In addition, the K-edge energy position relates linearly to the SOC of a real battery, which makes it possible to use the quantified Ni oxidation state as a proxy for pseudo SOC estimations as reported in the literature [65, 253–255, 274]. Hence, for quantification purposed and an easier comparison, edge energies for each sample were extracted from normalized K-edge XANES spectra using the 1^{st} inflection point of the Ni K-edge. While the edge energy for heat-treated $Li_{0.3}NCA$ is 8340.98 eV, the edge energies of NiO, pristine NCA, and as-prepared $Li_{0.3}NCA$ are 8340.32 eV, 8342.10 eV, and 8343.95 eV, respectively. Since the oxidation states for NiO, pristine NCA, and as-prepared $Li_{0.3}$NCA are exactly known, videlicet 2+, 3+, and 3.875+, a linear fitting was calculated and used to determine the oxidation state in the bulk of heat-treated $Li_{0.3}$NCA to 2.01+ (see Appendix Figure A.2a). In comparison to the strong shift in the Ni K-edge, the total observed energy shift towards lower energies in the Co K-edge spectra between as-prepared $Li_{0.3}$NCA and heat-treated $Li_{0.3}$NCA is only 0.5 eV.

4.2.2 2D-FF-TXM

2D-FF-TXM was used to visualize the lateral spatial distribution of the Ni oxidation state over an isolated secondary $Li_{0.3}$NCA particle upon *in-situ* thermal treatment to 450 °C. Using the beamline 6-2c of the SSRL, a series of 2D Ni K-edge XANES maps were collected as a function of the temperature (see Figure 24a-h). Note that unlike for 3D projections, the displayed 2D projections of the particle represent the averaged oxidation state over the depth of the spherical particle. The acquired 2D XANES maps show that the spatial distribution of the Ni oxidation state exhibits continuous overall reduction with increasing temperature as indicated by the evolution of the color-coded maps in Figure 24a-h. The red areas in panels a-d indicate that overall a higher oxidation state of Ni is present, while the visually drastic color change within panels e-g (compared to a-d) indicate significant changes that are occurring. The heterogeneity in the maps, on the other hand, highlights the complexity of the reaction at the mesoscale [275], where the grain boundaries and defects are populated. To better capture the dynamic evolution of the thermally driven chemical evolution on a single particle level, differential 2D Ni K-edge energy maps were calculated, as shown in Figure 24i-o. How the differential maps are calculated is hereby illustrated by the arrows below panels a-h, i.e., the first arrow (b-a) indicates that the map shown in panel i is a result of the subtraction of the map shown in panel a from the map shown in panel b. Doing so, two critical temperature transitions become now apparent on the calculated differential maps, namely the 200 - 250 °C and the 300 - 350 °C regions (Figure 24l and n). These differential

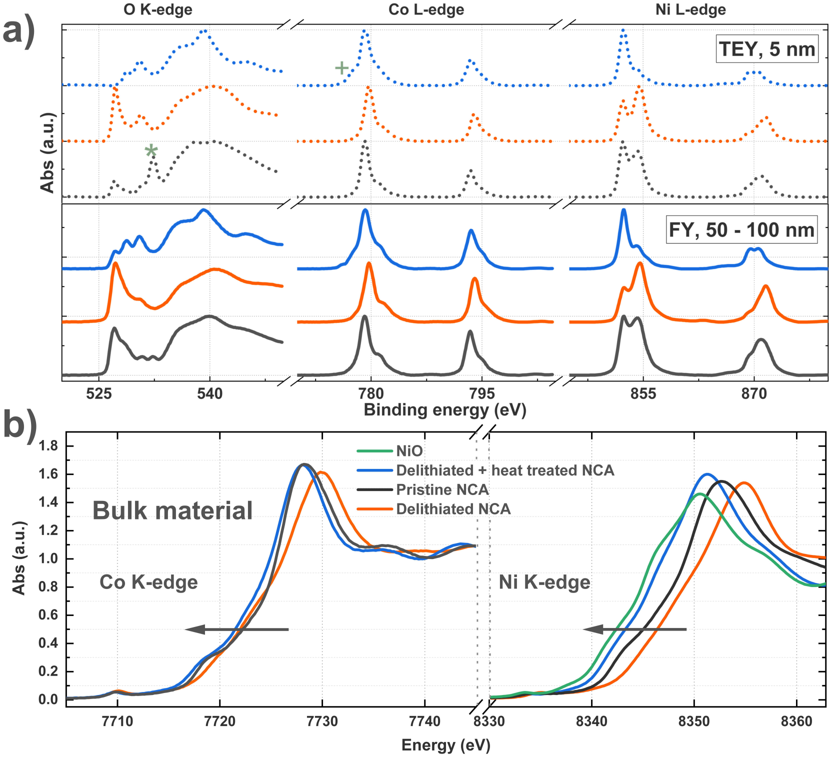

Figure 23: (a) Soft XAS O K-edge, Co L-edge and Ni L-edge spectra for pristine NCA (black), as-prepared $Li_{0.3}NCA$ (orange), and heat-treated (25 °C to 450 °C, 10 °C/min rate) $Li_{0.3}NCA$ powders (blue). Peak marked with a green asterisk in the O K-edge spectrum is associated with Li_2CO_3; plus sign in the Co L-edge spectrum is indicating slight reduction in Co. (b) Normalized Co and Ni K-edge XANES spectra of pristine NCA, as-prepared $Li_{0.3}NCA$, and heat-treated $Li_{0.3}NCA$; NiO (green) shown as a reference for Ni 2+.

maps show dark blue coloring and represent a strong negative shift of the Ni K-edge energy (see color-coded legend on the right side), which indicates a significantly higher degree of reduction that happened when transitioning from 200 to 250 °C and from 300 to 350 °C. Although not visually very distinguishable, another major energy shift is highlighted by plotting the energy distributions, namely 250 to 300 °C (see panel p). To get a better feel for the energy distributions of all visualized maps, the probability distributions of the Ni K-edge energy and the differential energy distributions of the XANES maps were plotted in Figure 24p and q, respectively. The energy distributions in panel p for the maps visualized in a-h confirm a monotonic reduction of the Ni oxidation state upon heating, while again highlighting two of the major shifts toward lower energies that appear upon heating from 200 to 250 °C and from 300 to 350 °C. In accordance with this, the probability distributions of the differential maps offer comparable information, although here the energy shift from 250 to 300 °C is not as pronounced. A very interesting finding to point out is that there are positive components in the probability distributions of the differential maps when closely looking at panel q, which is not to be confused with the continuous shift to lower Ni K-edge energies as visualized in panel p.

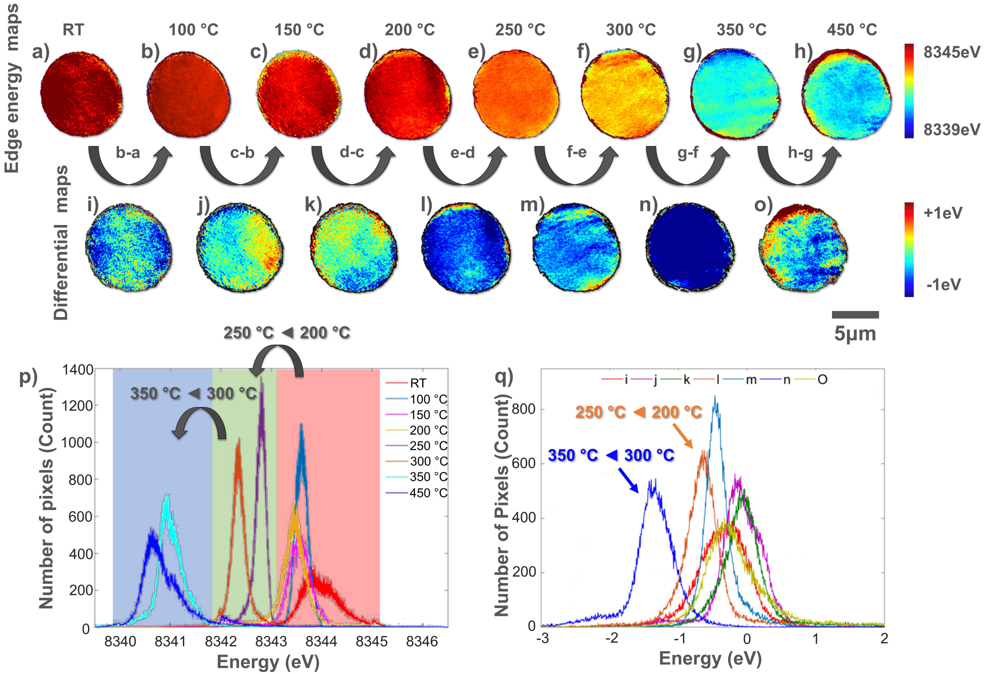

Figure 24: *In-situ* 2D Ni K-edge XANES mapping over a single NCA particle upon heat treatment to 450 °C. Panels (a-h) show the evolution (reduction) of the Ni oxidation state with their corresponding energy distributions of shown in panel (p). Panels (i-o) show the differential Ni K-edge energy maps, with their corresponding energy distributions shown in panel (q).

4.3 Particle Morphology

4.3.1 Surface Mesopores

Besides the phase transformations and concomitant chemical phase changes in surface and bulk, i.e., reduction of Ni, and the evolution of oxygen, the morphology in surface and bulk was also investigated and linked to each of the changes. For this, scanning electron microscopy (SEM) and focused ion beam (FIB)-SEM was utilized. The focus was not just set on the surface, but also the cross-section and the exact happenings inside of the bulk material upon heat treatment. Several as-prepared $Li_{0.3}$NCA as well as heat-treated $Li_{0.3}$NCA particles (450 °C) were subjected to a thorough surface SEM study and FIB-SEM tomography to highlight morphological changes throughout the particle and visualize the impact of oxygen evolution on the core, subsurface, and surface of the particle.

Figures 25a-b show the surface structure of as-prepared $Li_{0.3}$NCA. No major structural changes were introduced by the chemical delithiation process compared to pristine NCA, although slightly widened intergranular gaps on the surface could be seen for as-prepared 70% delithiated NCA compared to pristine NCA in a fully lithiated state. As-prepared $Li_{0.3}$NCA particles that were subjected to a heat treatment to 450 °C developed extensive mesopores on their surface as depicted in Figures 25c-d. Independent of the size of secondary particles, mesopores could be found on all heat-treated $Li_{0.3}$NCA particles of all sizes (see Appendix Figure A.4). To find the critical onset temperature at which the observed surface mesopores are formed, multiple batches of as-prepared $Li_{0.3}$NCA were heat-treated to various upper temperatures with a heating profile as used for TGA-MS and T-XRD. The critical temperature for the surface mesopores evolution was hereby found to be in the range 300 to 350 °C. The surface structures for three individual batches of as-prepared $Li_{0.3}$NCA heated to the upper temperatures of 150, 250, and 350 °C can be found in Appendix Figure A.5. The evolution of mesopores was not found to occur below 300 - 350 °C. Careful observation furthermore

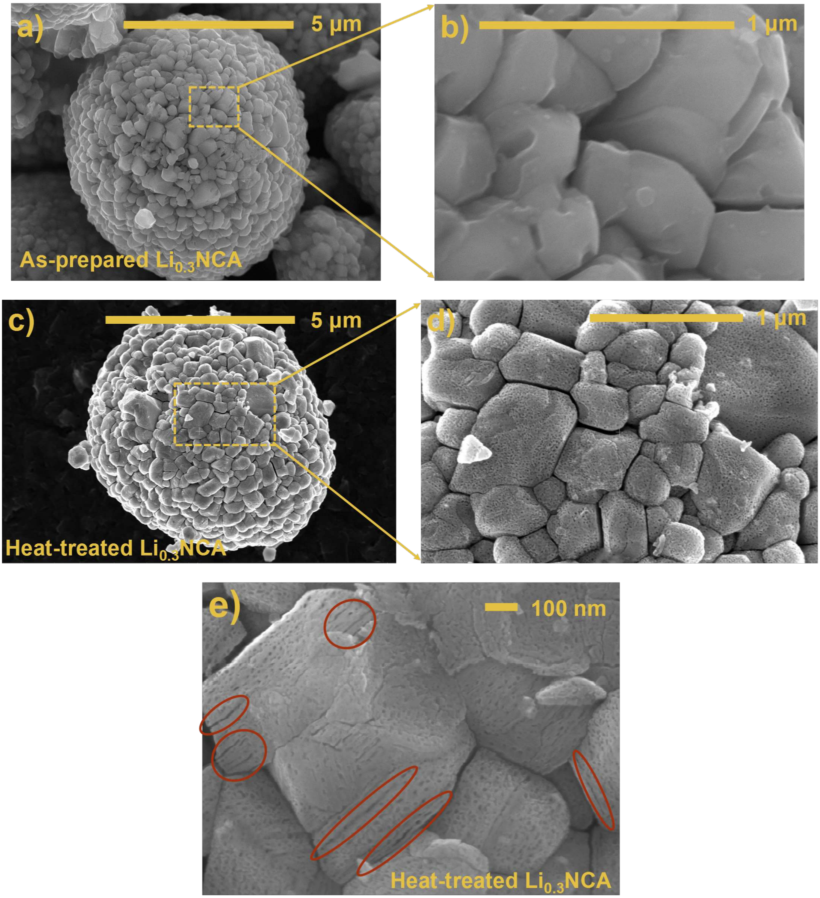

Figure 25: (a) Surface morphology of an as-prepared Li$_{0.3}$NCA particle with the marked area magnified in (b); no major morphological changes were observed on as-prepared chemically delithiated NCA. (b) Surface morphology of a heat-treated (450 °C) Li$_{0.3}$NCA particle with the marked area magnified in (d); in contrast to as-prepared Li$_{0.3}$NCA an extensive amount of uniformly distributed mesopores were visible on the surface. (e) Mesopores seem to appear along intragranular cracks (red circles).

revealed the formation of intragranular cracks within primary particles, with the majority of intragranular cracks showing parallel alignment (see Figure 25e). Further, a widespread presence of mesopores appearing preferably along these intragranular cracks was noticed.

4.3.2 Bulk Mesopores

As observed for the surface, the bulk also showed the formation of mesopores throughout the entire particle structure. Figure 26 shows the cross-section of several particles after FIB milling captured via SEM in two different detection modes. The entire cross-section (a-d) as well as highly magnified areas of different particles (e-h) highlight that mesopores are present ubiquitously throughout the bulk. Along with the mesopores, intergranular as well as intragranular cracks were visible for the particles after heat treatment to 450 °C. Upon closer look, intragranular cracks showed similar parallel alignment as seen on the surface, alongside mesopores appearing around the intragranular cracks. That mesopores and intragranular cracks are not just appearing in the very center of the bulk was confirmed via step-wise FIB milling of entire as-prepared $Li_{0.3}$NCA and heat-treated $Li_{0.3}$NCA particles, and subsequent SEM analysis of the resulting cross-section (FIB-SEM tomography). The results were visualized in videos and are available online (links to the videos can be found in the Appendix). That as-prepared $Li_{0.3}$NCA particles do not show any sign of intragranular cracking or mesopores was confirmed in Video A.1 [276]; only slightly larger intergranular gaps were observed for as-prepared $Li_{0.3}$NCA when comparing to pristine NCA. For heat-treated $Li_{0.3}$NCA, however, mesopores were found to be distributed throughout the entire particle alongside intragranular cracks (see Video A.2 [277]). Besides the observed and analyzed evolution of mesopores and intragranular cracking upon heat treatment throughout the bulk of the particle, another interesting finding was that crack volumes within heat-treated $Li_{0.3}$NCA particles seem to shrink due to the evolution of mesopores. All as-prepared $Li_{0.3}$NCA particles showed larger intergranular crack voids compared to their heat-treated $Li_{0.3}$NCA counterparts (see Figure 27).

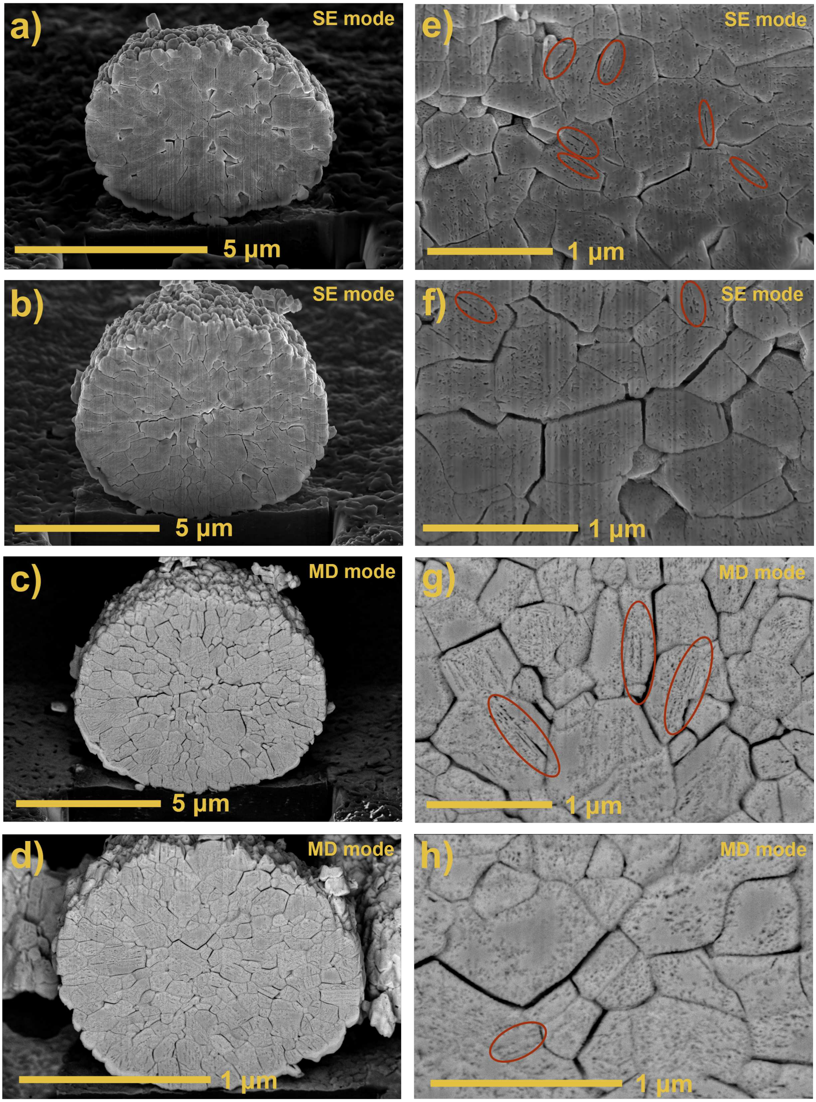

Figure 26: (a-d) Cross-sectional SEM images for several heat-treated $Li_{0.3}NCA$ particles after focused ion beam milling indicating a homogenous distribution of mesopores. (e-h) High magnifications of cross-sections show how mesopores appear along intragranular cracks (red circles) and throughout the entire particle.

This observation holds true for all analyzed as-prepared and heat-treated $Li_{0.3}NCA$ particles when comparing the intergranular crack void area, with the difference being especially distinct in the core of the particles.

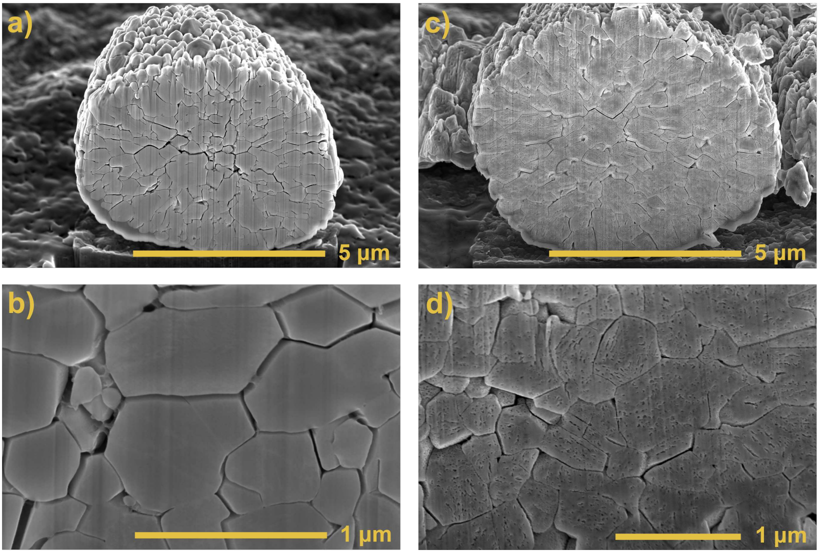

Figure 27: Cross-sectional SEM images after FIB milling for, (a) an as-prepared $Li_{0.3}NCA$ particle with the corresponding high magnification of the cross-sectional image shown in (b), and (c) a heat-treated $Li_{0.3}NCA$ (450 °C) particle with the corresponding high magnification of the cross-sectional image shown in (d).

4.3.3 Intergranular Crack Volume Decrease

To quantify the observed differences and to see how mesopores affect the intergranular crack volume, 2D slices of as-prepared and heat-treated $Li_{0.3}NCA$ particles with fixed cross-sectional areas were analyzed using a machine-learning algorithm. The Trainable Weka Segmentation (TWS) machine-learning tool for microscopy pixel classification was used for this purpose, circumventing a manually annotation of structural features of interest. The TWS project combines the very popular image processing toolkit Fiji [278], with machine learning algorithms of the Waikato Environment for Knowledge Analysis (WEKA) [279]. A brief overview of how the machine-learning algorithms were utilized is given below, more information on the detailed functionalities of the open-source software can be found in Arganda-Carreras et al [280]. To segment input image data of interest, in this case 2D grayscale images of entire cross-sections of FIB-milled as-prepared and heat-treated $Li_{0.3}NCA$ particles, the TWS algorithm transforms the segmentation problem into a pixel classification problem [280]. For this, a set of training input pixels, which have been labeled, is represented in the feature space and used for a selected classifier [280]. Once trained, it can be used to classify completely new image data that is fed to it (a schematic overview is given in Appendix Figure A.6), whereby all methods that are available in WEKA can also be used in TWS. Among other these include several supervised classification algorithms as well as clusters and regression algorithms [280].

After successfully training the classifier it was used to calculate the crack area in the 2D slices retrieved via FIB-SEM from as-prepared and heat-treated $Li_{0.3}NCA$. Although the quantitative information retrieved from cross-sections is 2D, i.e., an area, it is reasonable to assume that a larger crack area also implies a larger crack volume fraction, if two slices with same cross-sectional area are compared, which was one of the constraints as described above. In fact, when comparing as-prepared and heat-treated $Li_{0.3}NCA$ with similar cross-sectional areas, the total crack area of heat-treated $Li_{0.3}NCA$ particles was found to be smaller than that of the as-prepared $Li_{0.3}NCA$ particles (see Figure 28c and d). This indicates that mesopore evolution results in increased void volume within primary particles and thus decreased crack volume within the secondary agglomerate. The expansion of primary grains, which has been quantified for milled particles with very similar total cross-sectional areas in Figure 28, shows a significant reduction of the total crack area from 5.8% (as-prepared $Li_{0.3}NCA$) to 3.6% (heat-treated $Li_{0.3}NCA$). This calculation was repeated for pairs of as-prepared and heat-treated $Li_{0.3}NCA$ secondary particles with similar cross-sectional areas. On average, calculated crack area for as-prepared $Li_{0.3}NCA$ particles resulted in 5.3%, while heat-treated $Li_{0.3}$NCA particles showed a crack area of 4%.

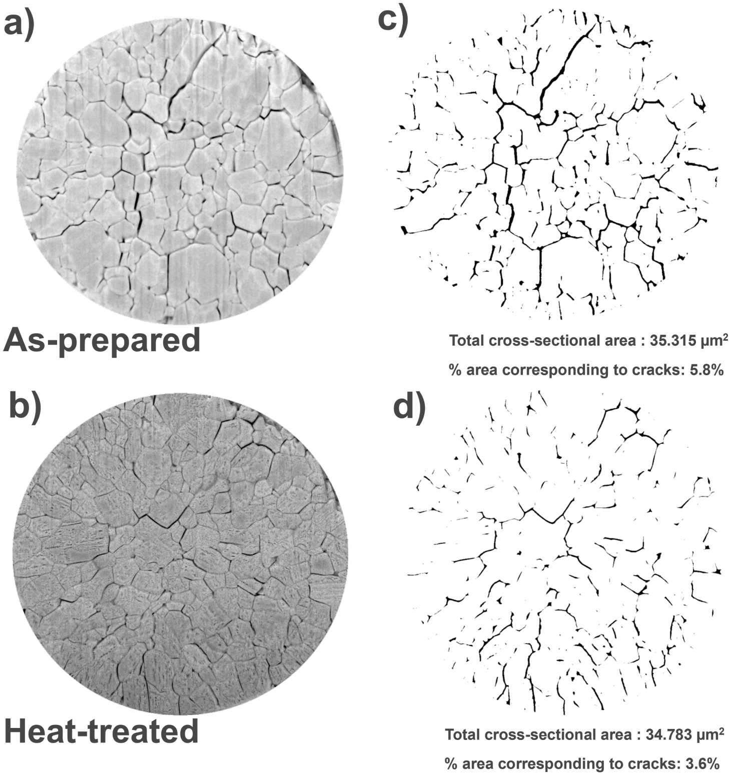

Figure 28: (a-b) Cross-sections of as-prepared and heat-treated $Li_{0.3}$NCA particles of similar total cross-sectional areas used to determine crack area using a machine learning algorithm, respectively. (c-d) Binary maps for the calculated crack area for the respective particle shown in (a) and (b).

4.4 Interpretation and Discussion

Although the thermal stability of Ni-rich layered oxide like NCA has already been studied in the literature [103, 281–284], a highly delithiated state of the cathode that equals an electrochemically (over-)charged state in a real application, has not been subjected to extensive studies, in which the thermomechanical interplay of Ni reduction, oxygen evolution, phase transformation, and particle morphology have been set on the focus. In fact, often times the cathode material under investigation is not delithiated to a state that would correspond to a highly discharged state in a real application; only a few studies, for example, by Nam et al. [250, 267], Yoon et al. [246, 285], or Belharouak et al. [234, 286, 287], have focused on studying NCA or NMC in highly delithiated states, primarily using T-XRD, TGA-MS, or accelerating rate calorimetry (ARC), but without correlating the thermal stability of highly delithiated NCA to the morphological changes. The results presented above show how phase transformation with concomitant Ni reduction, oxygen evolution via mesopores, and shrinkage of intergranular cracks are all in interplay, but more importantly, how the oxygen at higher temperatures, i.e., under thermal runaway conditions, can escape via mesopores within bulk and surface, which is one of the fundamental findings.

4.4.1 Correlation of Phase Transformation and Oxygen Evolution

When comparing T-XRD and TGA-MS data, the results are in very good agreement and indicate that NCA in a highly delithated state shows good short-term thermally stability up to a temperature of 200 °C. This can be concluded from the presented results, since no significant gases were released by the highly delithiated material below 200 °C as seen in the TGA-MS data, and no major structural changes below 200 °C were observed as seen in the T-XRD data, except for a small conjoining of the (108) and (110) reflections to form the $(440)_S$ peak, characteristic for the spinel phase. However, since the full $(440)_S$ peak only appears at 250 °C, this indicates, that the first phase transformation ($R\bar{3}m \rightarrow Fd\bar{3}m$) is happening in the range between 200 to 250 °C. In fact, the TGA-MS data reveals that the first oxygen release peak's maximum is reached at 250 °C, with an onset temperature of the oxygen evolution at 200

°C. Various onset temperatures of significant oxygen release have been reported in the literature such as 130 °C for NMC811 [86], 180 °C for charged $Li_{0.33}NCA$ [250], and around 200 °C for charged $Li_{0.1}NCA$ [288]. The presented TGA-MS results indicate an onset temperature for oxygen release of 200 °C for $Li_{0.3}NCA$ in absence of any composite electrode material such as (polymer) electrolyte, Li salt, or conductive carbon.

The major oxygen loss with an onset at 300 °C corresponds to the second phase transition (spinel, $Fd\bar{3}m$ → rocksalt, $Fm\bar{3}m$), and nicely correlates to the T-XRD data. More oxygen is released during this second phase transition compared to the first transition (layered, $R\bar{3}m$ → spinel, $Fd\bar{3}m$), which is consistent with a study by Nam et al., who have theoretically calculated the stoichiometry and oxidation state changes upon phase transformation of $Li_{0.33}NCA$ [250]. Analogously, the theoretical oxidation states for $Li_{0.3}NCA$ were calculated according to the observed layered-spinel-rocksalt phase transition as depicted in Eq. 12 and 13, and a general relationship for the oxygen release and reduction of Ni deduced (see Eq. 15). It is important to note that for all calculations a fixed oxidation state of 3+ is assumed for Co and Al, respectively, and that the oxidation state is not affected during (de-)lithiation of NCA; since Ni is the main charge compensator as discussed before, and Co does not show significant oxidation state changes, this constraint is justified.

$$\begin{aligned} \mathrm{Li_{0.3}Ni^{3.875+}MO_2}\ (\mathrm{R\bar{3}m}) &\rightarrow \\ \mathrm{Li_{0.3}Ni^{3.3+}MO_{1.77}}\ (\mathrm{Fd\bar{3}m}) + 0.115\ \mathrm{O_2} & \end{aligned} \tag{12}$$

$$\begin{aligned} \mathrm{Li_{0.3}Ni^{3.3+}MO_{1.77}}\ (\mathrm{Fd\bar{3}m}) &\rightarrow \\ \mathrm{Li_{0.3}Ni^{2.2+}MO_{1.33}}\ (\mathrm{Fm\bar{3}m}) + 0.22\ \mathrm{O_2} & \end{aligned} \tag{13}$$

For the sake of simplicity, Co and Al have been omitted from the NCA formula and are denoted as M (a schematic overview about the general formula is depicted in chapter 5, Eq. 15). Eq. 12 is related to the layered-to-spinel, and Eq. 13 to the spinel-to-rocksalt phase transformation, respectively. According to the theoretical calculation, more oxygen is released for the spinel-to-rocksalt phase transformation [250], in accordance with the obtained TGA-MS results. The results so far nicely demonstrate the linkage of the observed phase transformation of $Li_{0.3}$NCA and the distinct oxygen evolution, and is in good agreement with what has been communicated in the literature [250].

The absence of any gases at around 100 °C also speak for a very high level of dryness of the investigated sample, since the TGA-MS data shows no H_2O release at this temperature. The presence of H_2O at 100 °C is attributable to physisorbed water. It was shown previously that LiOH powder decomposes to Li_2O at 400 °C as indicated by Eq. 14 [289].

$$2\ \mathrm{LiOH} \rightarrow \mathrm{Li_2O} + \mathrm{H_2O} \tag{14}$$

LiOH surface contaminants or -OH groups on NCA's oxide surface may, however, decompose at a lower temperature. Hence, the H_2O release at the 200 to 250 °C and 250 to 300 °C transitions could originate from LiOH impurities or -OH groups on the surface of the sample [142]. There are no quantifiable amounts of CO_2 released during heating to 450 °C. Li_2CO_3 was shown to decompose only at 700 °C [289]. Thus, it is not possible to make a statement about the presence of Li_2CO_3 impurities on the NCA surface by only looking at the TGA-MS results. As described below, the presence of Li_2CO_3 can be confirmed via the O K-edge spectrum.

4.4.2 Ni Reduction Compensating the Oxygen Loss

The obtained oxidation state in surface, subsurface and bulk showed a reduction of Ni throughout the entire heat-treated particle to almost the level of Ni^{2+} as in NiO-type rocksalt. Furthermore, with an oxidation state of 2.06+ in the very surface, and 2.01+ in the bulk, determined via fitting of obtained spectra to known standards, the heat-treated $Li_{0.3}$NCA particle showed a homogeneously distributed oxidation state from surface to core. From the results it is clear that the Ni reduction throughout the entire particle is very severe and that the main charge compensation upon oxygen loss is stemmed by Ni, with Co showing little redox activity. That Co is reducing a bit in surface and bulk is represented in the Co L-edge soft XAS spectra by a shoulder, which appears for heat-treated $Li_{0.3}$NCA. In the Co K-edge hard XAS spectrum this appears in form of a very small edge shift of 0.5 eV to lower energies upon thermal stress. Previously it was shown that Co indeed is redox-active in Ni-rich layered oxides at high states of overlithiation [290], and that bulk Co can also play a role in compensating oxygen loss upon thermal stress within NCA [291]. The very small shift as observed herein is therefore indicative of that thermal decomposition is also affecting Co sites within the lattice, but not as much as observed for Ni. The small activity at Co sites during continuous heating to 500 °C was previously explained in the literature by a migration of Co cations into the adjacent tetrahedral sites during the first layered-to-spinel phase transition, and a subsequent further migration into adjacent octahedral sites that originally lay in the Li slab in the layered structure during the second spinel-to-rocksalt phase transition [250]. Ultimately, however, the degradation via layered-spinel-rocksalt phase transition upon thermal stress, and a concomitant permanent loss of oxygen is mainly compensated by the reduction of Ni.

The O K-edge spectrum reveals that the surface of as-prepared $Li_{0.3}$NCA might contain Li_2CO_3 impurities, indicated by the sharp peak at 532.3 eV. That Li_2CO_3 impurities are found on Ni-rich layered oxide materials has been previously discussed in the literature [292, 293]. Since Li_2CO_3 is mostly found on the outmost surface of the particle, the corresponding peak appears only in the surface-sensitive TEY mode (5 nm probing depth). During the delithiation process, the native Li_2CO_3 layer on the pristine NCA surface is washed away, resulting in an amplification of the lattice oxygen peak at 527.2 eV, and a subsequent reduction of the Li_2CO_3 peak. Comparable to the Ni L-edge spectra, there is also a significant change observed in the O K-edge spectra in both the surface and subsurface regions upon heat treatment. Notably, the remarkable decrease in the lattice oxygen peak at 527.2 eV and evolution of the peak at 539.2 eV, which is attributed to the formation of divalent Ni at the surface and subsurface. Along with the determined Ni oxidation state for the entire particle these observations clearly indicate that a NiO-type rocksalt phase is formed at the surface and subsurface upon heat treatment.

Finally, the image of the thermal decrepitation acquired via a series of 2D-FF-TXM imaging measurements sheds light on the interplay between phase transitioning, oxygen release, and Ni redox. Two distinct temperatures, at which the main Ni reduction is happening, are highlighted, namely 200 to 250 °C and 300 to 350 °C. Another important information obtained from 2D-FF-TXM is the charge distribution in its initial state before heat treatment, as well as how it evolves during the heating procedure. From the energy map observed in Figure 24a, it appears that the oxidation state of Ni, i.e., Ni K-edge energy, is very homogeneous. Further, it is visible that the energy distribution at most stages is very narrow and Gaussian, although the initial energy distribution of the as-prepared $Li_{0.3}NCA$ particle might seem slightly broader and hence appear heterogeneous when comparing to the energy distributions at higher temperatures. Although little literature is available on the topic of heating-induced local Ni redox changes for Ni-rich layered oxide systems, one study from Wei et al. highlighted how 50% electrochemically delithiated NMC622, in the form of $Li_{0.5}NMC622$, has a very heterogeneous charge distribution [244]; besides being very broad, the reported energy distribution for the as-prepared $Li_{0.5}NMC622$ was also negatively skewed [244]. Compared to this, the obtained energy distribution for the chemically delithiated $Li_{0.3}NCA$ here can be classified as homogeneous, and it can be assumed that the chemical delithiation is a very reproducible way for generating homogeneously delithiated cathode materials. A look into the energy distributions upon heating shows that a continuous overall reduction of Ni is happening throughout the particle after hitting the 200 °C threshold. Two major ‘jumps’ from 200 → 250 °C and 300 → 350 °C can be visually assessed. The first is correlated with the layered-to-spinel, and the second with the spinel-to-rocksalt phase transitions, respectively. At the first transition the average edge energy reduction is -0.66 eV, and at the second it is -1.42 eV, i.e., -2.08 eV in total. However, between 250 and 300 °C, an additional reduction of -0.46 eV is happening, due to the still ongoing and not fully completed layered-to-spinel phase transition and accompanying oxygen loss. This sums up to a total energy shift of -2.54 eV. With the total shift calculated via hard XAS to be 2.97

eV, this means, that most of the Ni reduction has been completed when heated to 350 °C. In fact, the energy distributions only show a final reduction from 350 to 450 °C, with an ultimate negative edge energy shift by 0.37 eV, summarizing the total observed Ni K-edge energy shift via 2D-FF-TXM to -2.91 eV (compare to -2.97 eV as obtained via hard XAS). With the energy distributions getting broader at 350 and 450 °C, a more heterogeneous charge distribution can be concluded, which is visually confirmed by the final Ni energy map at 450 °C. At this stage the phase transitions and Ni reduction might slow down or become more complicated.

Probability distributions of the differential edge energy show mostly symmetric peaks with peak locations at negative values, reflecting the described Ni reduction. However, especially at the very early stages of the heat treatment process, positive components are observed in the probability distributions of the differential edge energies. The positive components suggest local Ni oxidation, possibly due to thermal redistribution of Li ions as previously observed for NMC compounds [244]. As described by Wei et al., the local Ni oxidation within the cathode particle could be a result of Li migration-induced protrusions appearing on the surface of the particle [244].

4.4.3 Thermomechanical Interplay: Evolution of Mesopores

Besides undergoing a series of structural and chemical phase changes at elevated temperatures, experimental results related to the particle morphology suggest that thermal stress on the charged NCA cathode also involve the development of microporosity and particle cracking.

A first important discussion point is the observed slightly larger integranular gaps in the as-prepared, chemically delithiated $Li_{0.3}$NCA. Chemical delithiation has been widely used to prepare delithiated cathode materials with comparable delithiation grades similar to electrochemically charged cathodes. The process of chemical delithiation is advantageous, since larger quantities of chemically delithiated cathode active material can be prepared easily; additionally, the chemically delithiated material is free of any inactive components such as polymer, Li salt or conductive carbon that would be present in a real electrode. During the process of chemical delithiation, the cathode particles are uniformly delithiated, since the procedure is a wet chemical one, unlike in a real cathode where heterogeneities can be present due to bad covering of particles with electrolyte, or electrical disconnection [102]. Although sometimes it is debated that chemical delithiation results in unwanted particle cracking [102], the morphological insight into the analyzed as-prepared 70% chemically delithiated $Li_{0.3}$NCA shows intergranular gaps that are comparable to those that evolve during electrochemical delithiation of cathode materials. For comparison purposes, the exact morphology of a pristine NCA particle has been analyzed using FIB-SEM tomography; see tomography Video A.3 (mirror mode) and A.4 (captured via through-lens detector (TLD)) [294, 295]. At high delithiation grades, it is expectable that due to the well-known anisotropic lattice volume change some intergranular microcracks can be generated in Ni-rich layered oxides, as this has been investigated quite thoroughly in the literature [80, 89, 296–300]. As recently demonstrated by Park et al. for NCA with Ni fractions ≥ 0.88, microcracks are created upon charging to high cut-off voltages whereby the extent of cracking was more severe with increased Ni content and upper cut-off voltage; upon discharge, evolved intergranular cracks closed back fully for NCA with lower Ni fractions and when discharged to very small lower cut-off voltages, while gaps remained for material with higher Ni contents [80]. The observed slightly larger gaps between primary grains, i.e., intergranular microcracks, can therefore be attributed to a low lithiation grade similar to microcracks in an electrochemically delithiated cathode.However, the extent of intergranular cracks for a Ni fraction of 0.8 upon delithiation was not at all as severe as for Ni fractions ≥ 0.88 [80]. Hence, for Ni-rich layered oxides like NCA in which microcracks at high delithiation states and very high Ni fractions ≥ 0.88 are known to happen because of the anisotropic lattice volume change, chemical delithiation is a viable path. This way large quantities of cathode material, in a state where the extraction of Li is perfectly controlled and homogeneous, without altering the morphology in a different way as it would be with an electrochemical delithiation procedure, can be obtained.

The most important discussion point is the observed evolution of mesopores upon heat treatment that happens in surface and bulk, which has not been reported in the literature. The observed mesopores in surface and bulk strongly suggest that oxygen escapes via mesopores under thermal abuse conditions, whereby the evolution of mesopores is initiated at the transition from 300 to 350 °C. Notably, this temperature transition was shown to release most of the oxygen involving the biggest mass loss, cause the biggest negative shift in the Ni K-edge, i.e., greatest reduction, and the phase transition from spinel-to-rocksalt. This signifies that the mesopore formation is linked to the second phase transition at which also more oxygen is released, and Ni is stronger reduced, compared to the first phase transition, as demonstrated via theoretical calculations shown in Eq. 12 and Eq. 13. The oxygen release related to the first phase transition from layered-to-spinel occuring mainly from 200 to 250 °C did not cause any kind of pore formation; similar to the oxygen release as a result of the ongoing layered-to-spinel transition from 250 to 300 °C, which also did not show any pore formation. This means that small quantities of oxygen might be released slowly via existing microcracks, while a large amount of oxygen creates mesopores due to pressure that builds up within primary particles and a more abrupt release, because of the much larger oxygen amount. The formation of mesopores and densification of the material is also in accordance with the much higher density of the NiO-type rocksalt phase. This densification is also shown by the reduced crack area/volume. On average, a 1.3% smaller intergranular crack area was calculated for heat-treated particles in comparison to as-prepared $Li_{0.3}$NCA particles. Even though the calculated change in crack area cannot be directly translated into a change in the crack volume fraction, the attempt was made to calculate the volume fraction that is associated with the mesopore formation by using an ‘apparent crack volume’ obtained from the 2D binary maps and the mass loss; the details of the calculation can be found in Sheet A.1 [301]. While the result is quite sensitive to the density of the different NCA phases after heat treatment, this calculation gives a rough idea of the mesopore volume. Assuming that the NCA particles after heat treatment consist of a delithiated layered phase, a disordered rocksalt phase, intergranular cracks and mesopores, the mesopore volume fraction would be between 10% and 20%. Observed mesopore formation is significantly different from electrochemical cycling-induced surface degradation of layered Ni-rich oxides, which involve reaction of the cathode surface with the electrolyte and surface oxygen loss. The latter has been shown to cause stronger electrolyte decomposition than purely potential driven electro-oxidation of electrolyte, since singlet oxygen is released from the cathode surface at 80% delithiation of layered oxides reacts readily with electrolyte [105, 108, 302, 303]. Potential-induced oxygen loss starts at the surface and subsurface region, while the bulk mainly stays intact [100, 110, 243]. In this so-called core-shell model, which will also be explained in more detailed in chapter 5, the degradation of layered oxide materials is initiated by a transition from a layered phase to a spinel phase. Ultimately, the surface of the secondary particle transforms to the rocksalt phase, the subsurface to a spinel phase, while much of the core remains in the layered phase [110, 243, 283, 284, 304]. In the absence of electrolyte, the observed mesopores clearly show the evolution of oxygen from the surface as a result of thermal abuse. Further, the evolution of mesopores due to oxygen loss and concomitant phase transition is not limited and observed only for the surface, but also the subsurface and the bulk of the delithiated $Li_{0.3}$NCA particles submitted to thermal stress.

Besides the shrinkage of the intergranular crack volume due to mesopore formation, parallel intragranular cracks were also observed within primary grains along which many mesopores were found to form. This phenomenon might be similar to a study by Pengfei et al., who have observed that intragranular cracks in overcharged NMC111 are predominantly parallel and propagate along the (003) plane [131].

5 Chemothermal Stability of NCA in SPBs: Influence of Polymer and Li Salt

Thermal stability of Ni-rich cathode materials has been investigated extensively using a variety of techniques like ARC [305], XRD [306], time-resolved XRD [98, 237], differential scanning calorimetry (DSC)/TGA [237, 286, 306], and transmission electron microscopy (TEM) [307]. However, the focus in many of the mentioned studies has been rather the high temperature stability of the Ni-rich cathode materials under investigation. If the next-generation of high energy dense and safe batteries are going to utilize Ni-rich cathode materials and SPEs, it is of crucial interest to investigate their chemothermal stability at the operating temperatures relevant to SPBs. Since most of the commercially available dry solid-polymer batteries operate at elevated temperatures of > 60 °C [165, 166], the degradation of Ni-rich cathode materials (such as NCA) in contact with a conducting polymer electrolyte and Li salt needs to be quantified. In the best case, a differentiation of the degradation between surface and bulk needs to be made.

Therefore, in this chapter the degradation of NCA induced by the presence of individual electrode components, i.e., polymer and Li salt is investigated. The influence of polymer and Li salt combinations on the chemothermal NCA degradation at operating temperatures of SPBs is also studied along with the long-term thermal stability of delithiated NCA ($Li_{0.3}$NCA) using *ex-situ* synchrotron-based hard and soft XAS. As described in section 3.6.1, these techniques allow to probe the bulk and surface oxidation states of secondary NCA particles independently from each other. Hereby, the reduction of Ni on the surface, subsurface, and in the bulk of secondary NCA particles are studied and directly related to aging time, temperature, the presence of polymer electrolyte such as PEO or PCL, and/or Li salt such as $LiBF_4$ or LiTFSI.

Based on the polymer and/or Li salt accompanying the delithiated $Li_{0.3}$NCA, i.e., that is in contact with chemically delithiated NCA material, reduction of Ni at the surface, subsurface, and bulk occurs to varying extents, starting at the surface, and propagating into the bulk material. The obtained results give an idea about how the degradation, in the form of a reduced Ni valence, is strongly correlated to temperature, time, and whether the NCA material is in contact with polymer and/or Li salt. With the gained understanding of how the reduction of Ni is influenced by the presence of certain polymers and/or Li salts, solid-polymer cells are built and the relative stability is directly demonstrated by electrochemically cycling Li//NCA-PEO-LiTFSI and Li//NCA-PCL-LiBF$_4$ cells. A summary of how the presence of a certain polymer and Li salt is influencing the reduction of Ni is given in Figure 29.

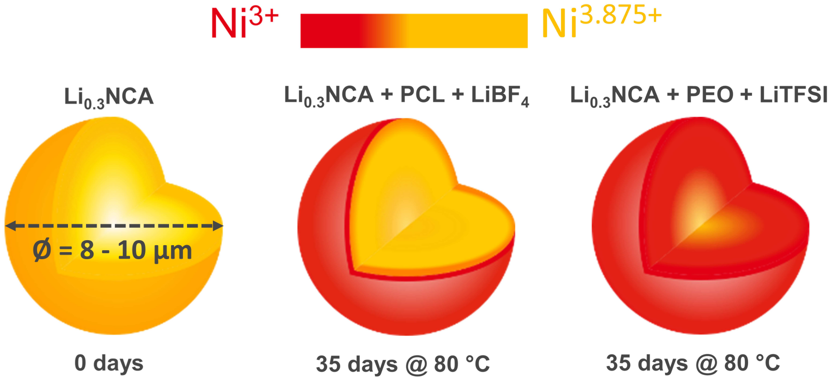

Figure 29: Schematic overview of the influence of the polymer/Li salt presence on the reduction of Ni in delithiated secondary NCA cathode particles. Storing delithiated Li$_{0.3}$NCA particles at 80 °C for 35 days shows significantly differing Ni reduction behavior in surface and bulk in presence of PEO-LiTFSI and PCL-LiBF$_4$

5.1 Intrinsic Stability of $Li_{0.3}$NCA at Elevated Temperatures

5.1.1 Surface Stability

Pristine NCA of commercial grade was chemically delithiated 70% (for details see section 3.1.1) to $Li_{0.3}$NCA using nitronium tetrafluoroborate (NO_2BF_4). The as-prepared delithiated $Li_{0.3}$NCA material was subsequently aged through storage at different temperatures and for various times. After pre-defined times, e.g., 2, 7, 14, 35, 49 days, aged $Li_{0.3}$NCA samples were taken out of their vacuum sealed pouch bags from the respective temperature chambers and analyzed using Ni L-edge soft XAS and Ni K-edge hard XAS. At first, only chemically delithiated $Li_{0.3}$NCA samples without the presence of any polymer and/or Li salt were analyzed. The TEY- and FY-mode derived L_3-edge peak ratios were calculated and interpolated to L_3-edge peak ratios of nickelate standards in order to quantify the respective Ni valence state as briefly described below.

Appendix Figures A.3a-b depict the L_3-edge peak ratio changes happening for $Li_{0.3}$NCA at the surface, i.e., TEY-mode (orange, 5 nm) and subsurface, i.e., FY-mode (green, 50-100 nm), for samples stored between 2 and 49 days at 60 - 90 °C. The calculated TEY and FY L_3-edge peak ratios were correlated to previously determined L_3-edge peak ratios of pristine nickelate standards (shown in Figures 16a-b) and as-prepared delithiated $Li_{0.3}$NCA (see Figure 15) with known valence states. A linear interpolation, as depicted in Appendix Figures A.3c-d, between the known valence state of nickelate standards and the TEY and FY L_3-edge peak ratios was established. With the established interpolation, TEY and FY L_3-edge ratios of aged samples can subsequently be used to calculate the apparent oxidation state.

To relate the determined Ni valence state to the SOC of a real polymer battery, as-prepared $Li_{0.3}$NCA (30% lithiated, Ni = 3.875+) and pristine NCA (100% lithiated, Ni = 3+) were used analogously for a fully charged polymer battery (4.2 V) and a fully discharged polymer battery (3.0 V). This way, the determined L_3-edge ratios can also be used to get an idea about the SOC changes or the degree of aging happening in regards to a real battery.

The resulting apparent oxidation states (and concomitant degree of aging) within the surface and subsurface for aged samples are shown in Figures 30a-b. The continuous drop of the Ni valence state with increased storage time indicates that $Li_{0.3}$NCA exhibits a strong temperature- and time-dependent reduction of the Ni valence, both at the surface (TEY, 5 nm) and the subsurface (FY, 50-100 nm). Reduction at the surface (TEY) is slightly higher than in the subsurface (FY). The observed Ni valence reduction correlates to a degree of aging $< 20\%$, both in the surface and subsurface of $Li_{0.3}$NCA at 60 °C, while $> 50\%$ aging, i.e., a stronger Ni reduction, were observed at 80 and 90 °C after 49 days of storage.

In addition to the degradation observed within the first 49 days, a long-term storage and aging was carried out for $Li_{0.3}$NCA samples. $Li_{0.3}$NCA in no contact with polymer and/or Li salt were additionally stored and aged for a total time of four months and one year. Since most of the commercially available SPBs, typically employing $LiFePO_4$ cathodes, operate at 80 °C [30, 308, 309], long-term aging was only carried out at 80 °C. Appendix Figure A.7 shows the apparent oxidation states and the correlated degrees of aging for $Li_{0.3}$NCA samples stored for up to 1 year at 80 °C. Similar as observed for the surface and subsurface stabilities for samples stored up to 49 days (see Figure 30a and b), FY derived apparent oxidation states (green data) show that there was less reduction upon storage at the subsurface than at the surface (orange data). This implies that the top surface of the cathode particles (probed by TEY) is always more reduced than the subsurface (probed by FY), which is due to surface reconstruction as mentioned in section 2.3.3.3. However, interestingly, TEY derived peak ratios of long-term (4 months, 1 year) aged samples were very similar to the ratios for samples stored for a total time of 49 days, which indicates that not much further reduction of the Ni valence state happens after 49 days of aging: Similar to samples analyzed after 49 days of storage at 80 °C, the Ni valence in $Li_{0.3}$NCA samples is reduced $> 50\%$, and this way much more aged than $Li_{0.3}$NCA samples stored at 60 °C. However, the average apparent Ni oxidation state for the surface and subsurface after 1 year is approximately 3.38+ (approx. 54% degree of aging), and hence not much different from samples stored at 80 °C for 49 days.

5.1.2 Bulk Stability

Figure 30c shows the normalized Ni K-edge XANES spectra for $Li_{0.3}$NCA stored at 80 °C for up to 1 year along with as-prepared $Li_{0.3}$NCA and pristine NCA shown as references (XANES spectra of samples aged at 60 and 90 °C can be found in Appendix Figure A.8). As indicated in section 3.6.1, a shift of the Ni K-edge towards lower energies, as shown in Figure 30c, indicates a reduction of the X-ray absorbing Ni atoms in the bulk material. After extracting the Ni valence states from the Ni K-edge spectra, it is apparent that within the first 49 days only little reduction of the Ni valence is happening in the bulk of the material as visualized in Figure 30d. However, long-term storage of $Li_{0.3}$NCA for 4 months and 1 year show significant shifts of the Ni K-edge to lower energy values, i.e., lower Ni valence. This has been quantified using the linear relationship between the Ni K-edge energy and the oxidation state (see Figures 16c for hard XAS spectra of common Ni-rich layered oxide standards), and put into relation of pristine NCA (Ni = 3+) and $Li_{0.3}$NCA (Ni = 3.875+) (see dotted lines). Besides no clear trend in reduction of the Ni valence for the first 49 days, the results further depict that the Ni valence reduction within the bulk material is independent of the storage temperatures. Thus, the clear trend originally observed with the surface-sensitive techniques (Figures 30a-b and Appendix Figure A.7) is not reflected in the bulk. Only samples subjected to 4 months of aging at 80 °C show a clear reduction in the measured Ni oxidation state, which does not substantially change further when samples are kept at 80 °C for 1 year. This observation is in good agreement with the findings from chapter 4, where the short-term thermal stability of $Li_{0.3}$NCA at 200 °C was shown.

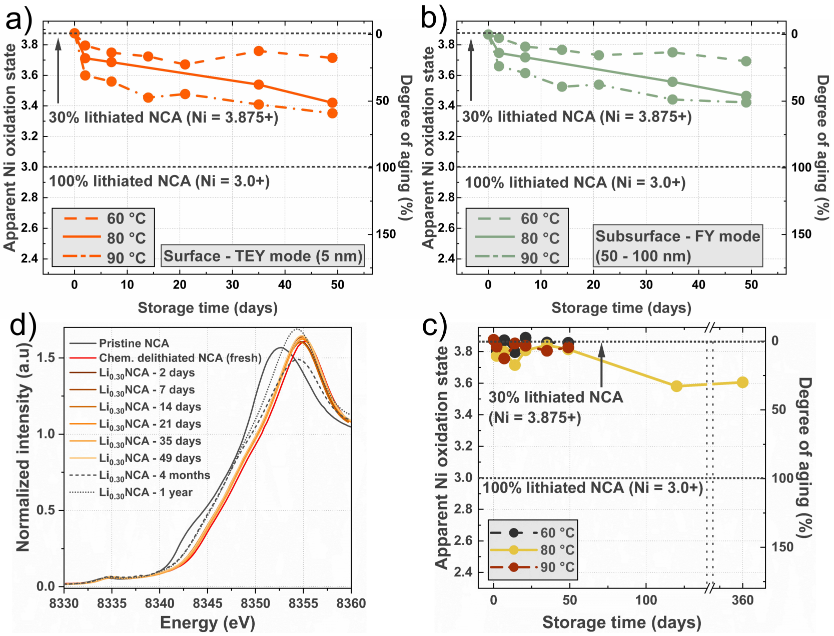

Figure 30: (a) and (b) Ni valence states and concomitant degrees of aging for Li$_{0.3}$NCA samples aged at various temperatures for up to 49 days, derived via interpolation. (c) Ni K-edge XANES spectra for pristine NCA, as-prepared Li$_{0.3}$NCA, and Li$_{0.3}$NCA stored at 80 °C for various times. (d) Ni bulk oxidation state and degree of aging as a function of storage time and temperature. No significant reduction of the bulk Ni valence state is apparent within the first 49 days of storage. Reduction is only apparent for samples stored for several months.

5.2 Stability of Li$_{0.3}$NCA in Presence of PEO and Li Salt

Since composite cathodes for SPBs do also contain other constituents besides the cathode active material, namely polymer, Li salt, and conductive carbon, it is important to also study the degradation happening within the cathode active material in presence of these components. Although it was demonstrated very recently that an interfacial protective coating covering the carbon/SPB interface is necessary for the high-voltage stability of PEO-based SPBs [198], in the following only the influence of the blended polymer and Li salt on the degradation are analyzed, since those are of primary importance.

Therefore, the degradation of $Li_{0.3}$NCA blended with polymer, Li salt, or both was studied. For this purpose, several cathode mixtures consisting of $Li_{0.3}$NCA blended with polymer, $Li_{0.3}$NCA blended with polymer (PEO) plus Li salt (either $LiBF_4$ or LiTFSI), or with these salts alone, were prepared and subsequently stored at 80 °C for 35 days. Weight ratios for each tested composition (see section 3.1.2) were based on real mixtures used in SPBs in order to mimic typically employed SPB compositions. Valence state changes at the surface, subsurface, and in the bulk of secondary $Li_{0.3}$NCA particles were quantified using soft XAS and hard XAS like the procedure described above. Unlike for $Li_{0.3}$NCA in absence of any other cathode component, which was also stored for up to 1 year, all following composite mixtures of $Li_{0.3}$NCA and polymer and/or Li salt were only stored for a maximum time of 35 days and always at 80 °C, for the sake of sample manageability. Additionally, it is important to note here, that the chosen storage conditions and storage time of 35 days are harsh. To give an example, over a time frame of 2 years, for a battery, which is charged once a day and spends approx. 1 hour at a highly charged (delithiated) state, the total time spent at this state would sum up to about 30 days. As learned from the section above, and the thermal stability of NCA studied in chapter 4, only very little bulk degradation would occur in this period within the NCA material itself, although the surface would show extensive reduction. Furthermore, since most commercially available SPBs are operated at around 80 °C, the storage temperature was fixed to 80 °C.

5.2.1 Surface Stability

Figure 31a shows the reduction happening at the surface (TEY, orange) and subsurface (FY, green) for $Li_{0.3}$NCA powder in combination with PEO alone. After 35 days of storage at 80 °C, the surface and subsurface of $Li_{0.3}$NCA with PEO indicate an apparent Ni oxidation state of 2.53+

and 2.83+, respectively, way below the valence of pristine NCA (3+). In comparison, for $Li_{0.3}$NCA in the absence of polymer and Li salt, after 35 days of storage, the apparent Ni oxidation state at the surface and subsurface were 3.54+ and 3.55+ (see Figures 30a-b). A much faster reduction of Ni located at the very surface of $Li_{0.3}$NCA particles is observed for $Li_{0.3}$NCA in presence of PEO.

In contrast to this finding, the presence of $LiBF_4$ alone (Figure 31b) seems to even benefit and opposes the reduction of Ni at the surface and subsurface. The reduction is less severe than in presence of PEO alone (Figure 31a) or for $Li_{0.3}$NCA without any polymer or Li salt (Figures 30a-b). With a Ni oxidation state of 3.66+ at the very surface and 3.72+ at the subsurface for $Li_{0.3}$NCA in contact with $LiBF_4$, this indicates that $Li_{0.3}$NCA is stabilized by the presence of $LiBF_4$. In fact, among the least reduction is seen in presence of $LiBF_4$ out of all tested active material, polymer, and/or Li salt combinations; a complete set of valence states for each combination can be found in Appendix Table A.1. In contrast to this, with LiTFSI, the reduction of Ni at the surface to 2.66+ and at the subsurface to 3.17+ is more severe, but not as severe as for $Li_{0.3}$NCA in contact with only PEO polymer.

A very interesting observation was made for the case of $Li_{0.3}$NCA combined with PEO and $LiBF_4$ or LiTFSI as seen in Figure 31c. No matter if PEO is combined with $LiBF_4$ or LiTFSI salt, in both cases the reduction in surface and subsurface is never as severe as for the case of $Li_{0.3}$NCA + PEO only. Furthermore, the Ni valence of $Li_{0.3}$NCA-PEO-LiTFSI in the surface and subsurface is barely different from the case of $Li_{0.3}$NCA-LiTFSI, which is especially true when comparing the Ni valence states for the subsurface regions (compare Figure 31b with 31c). In comparison, the reduction is more severe for $Li_{0.3}$NCA-PEO-$LiBF_4$ than for $Li_{0.3}$NCA in contact with only $LiBF_4$.

To summarize the results in a simple way, the surface and subsurface stabilities of $Li_{0.3}$NCA in contact with PEO, $LiBF_4$ or LiTFSI, or both after 35 days at 80 °C can be arranged in the order:

$Li_{0.3}NCA\text{-}LiBF_4$ > $Li_{0.3}NCA$ > $Li_{0.3}NCA\text{-}PEO\text{-}LiBF_4$ > $Li_{0.3}NCA\text{-}PEO\text{-}LiTFSI$ $\gtrsim$ $Li_{0.3}NCA\text{-}LiTFSI$ > $Li_{0.3}NCA\text{-}PEO$

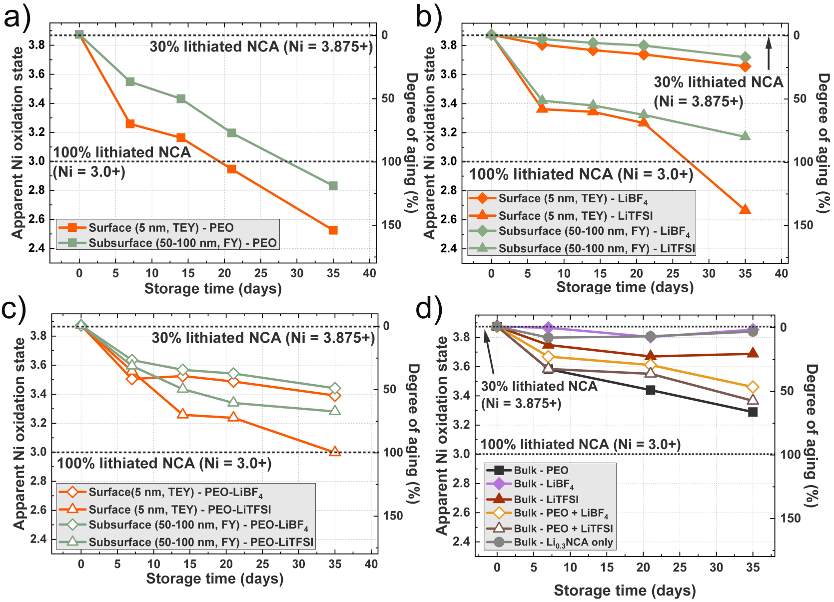

Figure 31: TEY (orange) and FY (green) Ni L_3-edge ratio derived apparent Ni oxidation states and the correlated degrees of aging for $Li_{0.3}$NCA in combination with (a) PEO, (b) Li salts, and (c) PEO and Li salts stored at 80 °C. (d) Ni oxidation state and degree of aging for the bulk $Li_{0.3}$NCA material after 35 days of aging at 80 °C in combination with PEO, Li salts, and both. $Li_{0.3}$NCA in absence of polymer and/or Li salt shown as reference.

5.2.2 Bulk Stability

When looking at the bulk stabilities presented in Figure 31d, the Ni bulk oxidation state of $Li_{0.3}$NCA degraded the most when in contact with PEO (black). When PEO and Li salts were used in the mixture, the degree of aging was not as great as with PEO only, whereas PEO-LiTFSI (brown), showed higher degrees of aging than PEO-$LiBF_4$ (yellow). The obtained bulk stabilities follow the observed degradation trend for the surface and subsurface as analyzed using soft XAS. In keeping with that trend, the bulk, like the surface and subsurface regions, showed excellent stability and minimal reduction for $Li_{0.3}NCA$ mixed with $LiBF_4$ alone (purple). Surprisingly, the bulk materials also show little degradation with LiTFSI (red), while the surface and subsurface showed a very drastic reduction happening within 35 days. Hard XAS spectra from which the bulk Ni valence states were extracted from can be found in Appendix Figure A.9.

In summary, the bulk stabilities of $Li_{0.3}NCA$ in contact with PEO and $LiBF_4$ or LiTFSI after 35 days at 80 °C can be arranged in the order:

$Li_{0.3}NCA\text{-}LiBF_4 \approx Li_{0.3}NCA > Li_{0.3}NCA\text{-}LiTFSI > Li_{0.3}NCA\text{-}PEO\text{-}LiBF_4 > Li_{0.3}NCA\text{-}PEO\text{-}LiTFSI > Li_{0.3}NCA\text{-}PEO$

5.3 Stability of $Li_{0.3}NCA$ in the Presence of PCL and $LiBF_4$

5.3.1 Surface Stability

To see how $Li_{0.3}NCA$ in combination with a different polymer electrolyte degrades and exhibits similar degrees of degradation (with and without Li salts), instead of PEO, PCL was used and combined with $Li_{0.3}NCA$ in a similar manner as seen above. Note that since $Li_{0.3}NCA$ blended with $LiBF_4$ showed the most promising results in terms of oxidative stability, PCL was only blended with $LiBF_4$ unlike for the PEO case, where both Li salts were analyzed.

When comparing the Ni valence reduction for $Li_{0.3}NCA$ blended with only PCL or PEO polymer (Figure 32a), the Ni valence reduction seems to be less severe when $Li_{0.3}NCA$ is in contact with PCL. The surface and subsurface regions for the $Li_{0.3}NCA$ particles expressed a reduction from the initial oxidation state of 3.875+ to 3.33+ and 3.45+, respectively, much less than for the PEO case (2.53+ and 2.83+ at the surface and subsurface, respectively). $Li_{0.3}NCA$ also showed improved stability with

PCL-$LiBF_4$ compared to PEO-$LiBF_4$ (see Appendix Table A.1); after 35 days of aging, $Li_{0.3}NCA$ in a matrix of PCL-$LiBF_4$, only showed a reduction of the initial oxidation state to 3.62+ and 3.69+ for the surface and subsurface, respectively. PEO-$LiBF_4$, in comparison, showed a Ni valence reduction within the surface and subsurface down to 3.39+ and 3.44+, respectively. This indicates that PCL in combination with $LiBF_4$ is almost two times more chemothermally stable than PEO-$LiBF_4$ in contact with the highly oxidizing $Li_{0.3}NCA$. In fact, $Li_{0.3}NCA$ in contact with PCL-$LiBF_4$ showed to retain the Ni valence in surface and subsurface almost as good as for the case of $Li_{0.3}NCA$-$LiBF_4$ (TEY = 3.66+, FY = 3.72+). To see the gap between the worst and best performing polymer and Li salt combination, i.e., PEO-LiTFSI and PCL-$LiBF_4$, the surface and subsurface Ni valence retention for each case were plotted against each other as depicted in Figure 32b. Comparing the worst and best performing polymer-Li salt combination one can see that the difference in Ni reduction is more than twice.

In summary, the surface and subsurface stabilities of $Li_{0.3}NCA$ in the presence of PEO or PCL, and Li salt can be arranged in the order:

$Li_{0.3}NCA$-$LiBF_4$ $\approx$ $Li_{0.3}NCA$-PCL-$LiBF_4$ $>$ $Li_{0.3}NCA$ $>$ $Li_{0.3}NCA$-PEO-$LiBF_4$ $>$ $Li_{0.3}NCA$-PCL $>$ $Li_{0.3}NCA$-PEO-LiTFSI $>$ $Li_{0.3}NCA$-LiTFSI $>$ $Li_{0.3}NCA$-PEO

5.3.2 Bulk Stability

The observed surface and subsurface stabilities with PCL could also be seen when analyzing the degradation in the bulk material. Figure 32c shows that the average Ni valence state in the bulk material is reduced to 3.73+ for $Li_{0.3}NCA$ in contact with PCL-$LiBF_4$ after 35 days, while the Ni oxidation state for $Li_{0.3}NCA$ in presence of PEO-LiTFSI dropped to 3.37+, respectively. A comparison of the values obtained for the degree of aging, in analogy to a fully dicharged (fully lithiated cathode, Ni = 3+, 3.0 V) and a fully charged (fully delithiated cathode, Ni = 3.875+, 4.2 V) battery, a roughly three times higher stability of PCL over PEO also in terms of the bulk oxidation state retention is the result. From the presented results the chemothermal stability and the presence of a differing polymer, Li salt, or their combination, has a significant impact on the reduction of Ni and hence degradation of the cathode active material. It is important to emphasize here that all this happens *ex-situ*, i.e., without subjecting the cathode active material to any kind of electrochemical (de-)lithiation process.

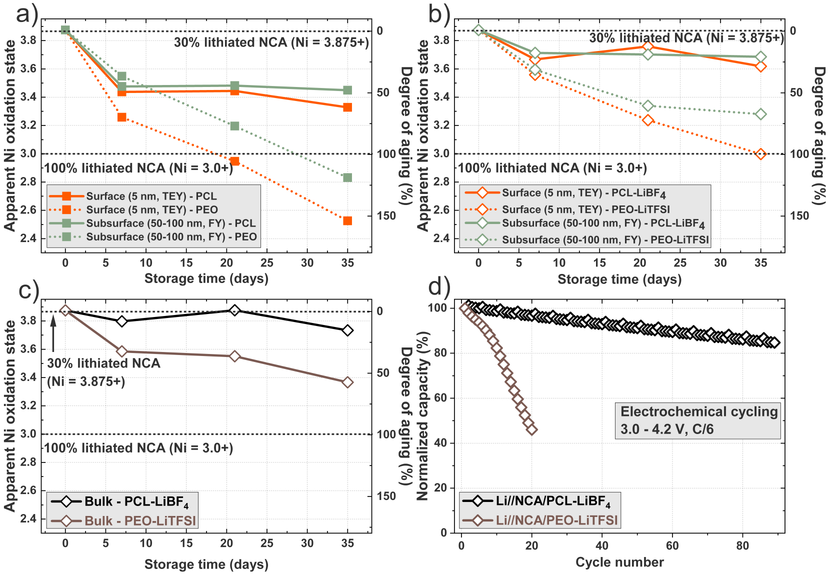

Figure 32: (a) TEY (orange) and FY (green) Ni L_3-edge ratio derived apparent Ni oxidation states and the correlated degrees of aging for $Li_{0.3}$NCA in combination with PCL or PEO. (b) Ni oxidation state and degree of aging for $Li_{0.3}$NCA blended with PCL-$LiBF_4$ or PEO-LiTFSI. (c) Ni oxidation state and degree of aging for the bulk of $Li_{0.3}$NCA blended with PCL-$LiBF_4$ or PEO-LiTFSI. (d) Normalized capacities for NCA polymer cells embedded in a PCL-$LiBF_4$ (black) and PEO-LiTFSI (brown) polymer matrix.

5.3.3 Electrochemical Cycling Stability

The improved stability and delayed Ni reduction of $Li_{0.3}$NCA in presence of PCL (compared to PEO) was also reflected in the electrochemical cycling of Li//NCA-PCL-$LiBF_4$ cells. Figure 32d compares the capacity retention of Li//NCA-PCL-$LiBF_4$ cells compared to Li//NCA-PEO-LiTFSI cells cycled at a rate of C/6 and 80 °C. While the PEO cell shows significantly reduced capacity within the first 20 cycles, the PCL cell could be cycled well over 80 times with $> 80\%$ capacity retention; note that both polymer cells utilize the DryLyte separator. This promising result shows that the use of PCL as a polymer matrix for SPBs coupled with NCA is promising, and that the chemothermal stabilities are directly reflected in the electrochemical performance of SPBs.

5.4 NMC Cathodes in Presence of PCL and Li Salt

The previous findings showed that the employed polymer matrix and Li salt not only have an influence on the *ex-situ* Ni reduction, i.e., without any electrochemical (de-)intercalation activity, but also show that PCL is a very promising polymer material to be considered as a host matrix, as also shown by Bergfelt et al. [223]. As discussed in section 2.3.3.1, NCA is considered as one of the cathode materials of choice for the next generation of LIBs and LMB to come. However, it is also important to study if the results up to this point, i.e., a more stable cathode material in a highly delithiated state and less Ni reduction in the presence of PCL, can also be transferred or applied to other promising cathode materials like NMC622 or NMC811. More importantly, it is necessary to study how the Ni content, as the main charge compensator upon delithiation, influences the chemothermal stability at the surface, subsurface, and bulk of Ni-rich cathode materials.

Therefore, to see if the enhanced chemothermal stability of $Li_{0.3}$NCA in contact with PCL and $LiBF_4$ is also transferable to other commercially relevant Ni-rich layered oxide materials, blends of chemically delithiated NMC622 ($Li_{0.3}$NMC622) and NMC811 ($Li_{0.3}$NMC811) with PCL and/or

$LiBF_4$ were prepared as described in section 3.1.2. An overview of the surface and bulk oxidation state retention of Ni in $Li_{0.3}$NMC622 and $Li_{0.3}$NMC811 is given in Figure 33. It is relevant to note that unlike for $Li_{0.3}$NCA, in $Li_{0.3}$NMC622 and $Li_{0.3}$NMC811, the Ni oxidation states in a 70% chemically delithiated state are differing from valence state of Ni (main charge compensator), due to the replacement of Al with Mn in NMC materials. In a fully lithiated state, Ni valence states in $Li_{0.3}$NMC622 and $Li_{0.3}$NMC811 are 2.66+ and 2.88+, respectively, as opposed to 3.83+ and 3.75+ in a 30% lithiated state.

5.4.1 Surface Stability

From Figures 33a and d it is visible, that the surface stability of $Li_{0.3}$NMC622 is better when in contact with $LiBF_4$ or PCL-$LiBF_4$ compared to that of $Li_{0.3}$NMC811 with the same combinations. Especially striking is the very strong reduction of the Ni valence in the surface of $Li_{0.3}$NMC811 in contact with PCL alone. Comparing the full composite, i.e., cathode active material blended with PCL-$LiBF_4$, the surface Ni valence state of $Li_{0.3}$NCA, $Li_{0.3}$NMC622, and $Li_{0.3}$NMC811 was determined to 3.62+, 3.63+, and 3.40+, respectively, after a storage time of 35 days at 80 °C, with $Li_{0.3}$NMC811 showing 23% more aging than $Li_{0.3}$NMC622 (see Appendix Table A.1). The observation for the subsurface is similar to that of the surface of the material. Although here the strong degradation of $Li_{0.3}$NMC811 in contact with only PCL was not as strong as exhibited for the surface (compare Figures 33d and e), but still almost twice as high as for $Li_{0.3}$NMC622. The retained Ni oxidation state in the subsurface for $Li_{0.3}$NCA, $Li_{0.3}$NMC622, and $Li_{0.3}$NMC811 blended each with PCL-$LiBF_4$ and stored for 35 days at 80 °C was determined to be 3.69+, 3.46+, and 3.38+, respectively. Noticeably is that both $Li_{0.3}$NMC622 and $Li_{0.3}$NMC811 exhibit very similar Ni valence retentions in the subsurface when in contact with PCL and $LiBF_4$ throughout the entire storage period (compare diamonds in Figures 33b and e). Interestingly, for NMC622 with only $LiBF_4$ salt the reduction of Ni in the subsurface was not as strong as observed for

NMC811 with $LiBF_4$.

5.4.2 Bulk Stability

The bulk stabilitites of $Li_{0.3}$NMC622 and $Li_{0.3}$NMC811 are very much comparable to the bulk stabilities observed for $Li_{0.3}$NCA and do not show any significant differences. For example, in presence of only $LiBF_4$ salt, the bulk Ni oxidation states in $Li_{0.3}$NCA, $Li_{0.3}$NMC622, and $Li_{0.3}$NMC811 are 3.85+, 3.80+, and 3.67+, similarly, in presence of both PCL and $LiBF_4$, the Ni valence states are 3.73+, 3.72+, 3.72+, respectively. In the case of being blended only with the polymer host PCL, the reduction in the bulk Ni valence is similar to the behavior observed for the surface and subsurface, i.e., a strong reduction within 35 days at 80 °C for the case of $Li_{0.3}$NMC811 (Ni valence of 3.06+), and comparable reduction of Ni within the bulk of $Li_{0.3}$NCA and $Li_{0.3}$NMC622 to 3.50+ and 3.60+, respectively.

5.5 Interpretation and Discussion

5.5.1 Inherent Stability of Delithiated NCA

The observed reduction and concomitant degradation of Ni located in the surface and subsurface of $Li_{0.3}$NCA particles (Figure 30) can most likely be explained by a core-shell model. In this model it is assumed that the degradation of layered oxide materials is initiated by a phase transition from the layered phase to a spinel or rocksalt phase from surface to bulk. This phenomenon, sometimes referred to in the literature as surface reconstruction (see section 2.3.3.3) [100, 310], happens due to rearrangement of TM atoms but also triggered by lattice oxygen release, as previously reported in the literature [65, 100, 110, 243, 311]. Highly delithiated cathode materials are especially prone to this phase transition [125, 311]. This phase transformation and the resulting spinel/rocksalt surface layers influence the charge-transfer resistance negatively, limit Li transport and diffusion, and finally prevent the intercalation of Li.

Here, the chemically delithiated $Li_{0.3}$NCA undergoes structural trans-

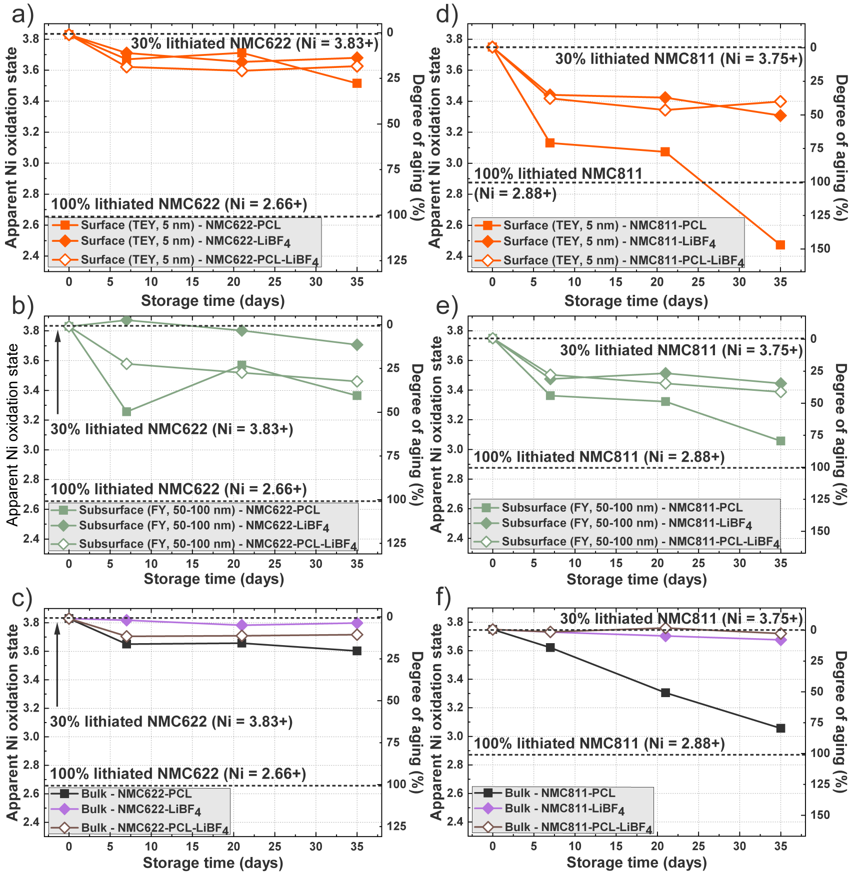

Figure 33: (a) and (b) Ni valence states and correlated degrees of aging for $Li_{0.3}$NMC622 in combination with PCL, $LiBF_4$, and both stored at 80 °C for up to 35 days, respectively. (c) Ni bulk oxidation states and correlated degrees of aging for $Li_{0.3}$NMC622. (d) and (e) Ni valence states and correlated degrees of aging for $Li_{0.3}$NMC811 in combination with PCL, $LiBF_4$, and both stored at 80 °C for up to 35 days, respectively. (f) Ni bulk oxidation states and correlated degrees of aging for $Li_{0.3}$NMC811.

formations at elevated temperatures involving, among others, oxygen evolution and reduction of Ni. Since the reduction of Ni in the surface and subsurface was almost always more severe than in the bulk, one can conclude that the phase transformation, manifested in the reduction of Ni, starts at the surface and propagates into the bulk material with prolonged aging time, which is in good agreement with the literature [311]. This is further fortified when comparing the surface stabilities (probed via TEY soft XAS) with subsurface stabilities (probed via FY soft XAS). The reduction found in Ni located at the very top 5 nm of secondary cathode particles was almost for every case higher than that for Ni located in the top 50-100 nm subsurface. In chapter 4 it was shown with TGA-MS that the onset of oxygen evolution from $Li_{0.3}NCA$ occurs at around 200 °C. Although the $Li_{0.3}NCA$ samples in absence of any polymer and Li salt were stored at temperatures of 60 - 90 °C, it cannot be ruled out that a small amount of oxygen escapes from the surface or subsurface at these temperatures and long storage times. This release of oxygen from the surface would then initiate the decomposition at the surface, with concomitant propagation of the phase transformation to the bulk. Furthermore, the release of oxygen from the crystal lattice may be exacerbated at a low partial oxygen pressure, i.e., the storage in an inert atmosphere as was done for all samples. The observed degradation of $Li_{0.3}NCA$ via the release of oxygen, creation of vacancies within the oxide material and accompanying Ni valence reduction is schematically shown in Eq. 15 (also see Eq. 12 and 13 in chapter 4 for a numerical example).

$$\begin{gathered} Li_{0.3}Ni_{0.8}^{3.875+}Co_{0.15}^{3+}Al_{0.05}^{3+}O_2 \rightarrow \\ Li_{0.3}Ni_{0.8}^{(3.875-y)+}Co_{0.15}^{3+}Al_{0.05}^{3+}O_{(2-\frac{2}{5}y)} + \frac{y}{5}\,O_2 \end{gathered} \tag{15}$$

The core-shell model has been widely accepted in the literature and has established itself as the model to explain the structural layered-spinel-rocksalt phase transitioning occurring in layered Ni-rich materials [111, 312, 313]. As mentioned in section 2.3.3.3, the layered-spinel-rocksalt phase transitioning is energetically favored meaning that the layered phase will ultimately transform to a rocksalt phase under degrading and harsh conditions, however, this does not happen in a fast manner due to kinetic reasons [111]. Since the surface is more exposed to degrading conditions, for example by being in contact with the electrolyte, the surface material generally is more prone. Therefore the layered-to-rocksalt transition can start here by oxidation of lattice oxygen and concomitant TM migration and reduction [107, 265, 283]. The resulting rocksalt phase in the surface prevents further transformation of the layered phase in the bulk due to separation of the layered phase from the degrading conditions by the isolating rocksalt surface layer [111, 314].

The observed degradation of the bulk of the delithiated cathode can be explained in several way. As shown in chapter 4, upon heating, the entire material releases oxygen. This would trigger a phase transformation from layered-to-spinel or layered-to-rocksalt also in the bulk, which has also been observed in the literature [86, 267, 282]. Although, due to the lower temperatures at which the samples were stored, this transformation would not happen immediately but over the course of the storage, which was also observed. One additional possibility is the formation of the so-called ‘anti-core-shell’ structure as shown by Zhang et al. [111] for NCA material: oxygen from within the bulk of the particles can migrate to the surface that results in localized areas of reduced oxygen concentration in the bulk [111]. The layered phase subsequently transforms to rocksalt domains [111]. This formation of rocksalt regions within the bulk of NCA can be an alternative pathway to the formation of the traditional core-shell structure [111]. However, while the formation of a core-shell structure with an inactive rocksalt surface could hinder the outgoing oxygen diffusion, and hence the formation of rocksalt domains in the bulk [111], the formation of rocksalt domains inside the bulk would not prevent further formation of a rocksalt surface layer.

5.5.2 Influence of Polymer and Li salt

Surface and bulk stabilities of $Li_{0.3}$NCA demonstrate the poorest chemothermal stabilities in presence of PEO. A plausible explanation for this is the well-established poor oxidative stability of PEO above 4 V, as discussed in the literature on polymer cells [315]. As previously noted,

$Li_{0.3}NCA$ is equal to electrochemically delithiated NCA at a potential of 4.2 V vs. Li^+/Li. At this highly delithiated state, PEO in contact with highly oxidizing $Li_{0.3}NCA$ can be irreversibly oxidized and hence lead to a reduced Ni valence. Although it is important to mention that the onset voltage at different temperatures for this reaction were reported and found to be rather sluggish [316, 317].

The harsh reduction of Ni in the bulk material in presence of PEO could also be related to the aforementioned oxygen vacancy diffusion from surface to bulk and the oxidation of PEO. Upon oxidation of PEO electrons are released which can travel throughout the entirety of the spherical NCA particle. Hence, once the surface Ni of the particle has been reduced via PEO oxidation, a lot of PEO is still left being the host matrix of the composite electrode. Therefore the PEO oxidation can continue, resulting in more electrons that can travel through the particle into the bulk and continue reducing Ni there. It has to be added that, although no significant short-term oxygen evolution was observed below 80 °C in the TGA-MS measurements in chapter 5, the evolution of oxygen coming from the bulk can still be possible when considering the long storage times. Another, more speculative, explanation of the bulk degradation are radical reactions with the PEO polymer chain, abstracting oxygen from the lattice structure of surface NCA. The so created oxygen vacancies would initiate a diffusion of oxygen from the bulk to the surface vacancies, leaving behind an oxygen depleted bulk region that can undergo a phase transformation. One would have to keep in mind the diffusion limitations of oxygen vacancies at the employed storage temperatures, since the diffusion of oxygen vacancies generally occurs only at high temperatures. Nevertheless, as seen with the formation of the anti-core-shell structure [111], this vacancy diffusion is still possible. The question of how polymer chain radicals are formed was already often addressed in the literature. For example, a very small concentration of radical sites are always present within the polymer, which can start a radical chain reaction [318]. As proposed by a theoretical study by de Saint Claire, these radical sites in PEO polymer can react with molecular oxygen forming hydroperoxides [318]. In a second step, the generated peroxide radicals will then react with side chains of the polymer (intermolecular mechanism), forming further side chain radicals within the polymer [318]. Eventually, hydroperoxide species undergo a thermal dissociation (monomolecular) forming alkoxy radicals and hydroxyl radicals (see Appendix Figure A.10) [318]. Radicals created by this way can continue degrading the PEO polymer, as well as abstract oxygen from the NCA lattice structure. This speculative view on the bulk degradation in presence of PEO is supported by studies that have shown that PEO stored at 80 °C in an inert atmosphere does not change the structure. However, PEO stored under the same temperature in air degraded through oxidation [319]. This is also supported by the fact that oxygen can be trapped in voids of fresh PEO polymer [320].

An interesting finding is the fact that when $Li_{0.3}NCA$ was only mixed with $LiBF_4$ or LiTFSI salts without polymer, less Ni reduction was obtained in the $Li_{0.3}NCA$-$LiBF_4$ blend compared to $Li_{0.3}NCA$-LiTFSI. Furthermore, using only $LiBF_4$ as an additive showed the least degradation in surface, subsurface, and bulk. The use of $LiBF_4$ results in good cyclability of liquid electrolyte containing LIBs, but is also known to reduce parasitic reactions and increase performance of batteries at high operating voltages and a wide temperature range [321–327]. In the performed *ex-situ* experiments here, i.e, where the cathode does not undergo electrochemical cycling, $LiBF_4$ could still slow Ni reduction due to passivation effects. For example, $LiBF_4$ is an ate complex of lithium fluoride (LiF) + boron trifluoride (BF_3), which separates into its original composition at high temperatures and hence shows endothermic behavior [328]. More importantly, a recently disclosed patent application showed how the surface of NMC cathodes can be passivized using $LiBF_4$ in order to prevent decomposition upon exposure to ambient conditions and moisture [329]. In their disclosure, the authors treated NMC material with $LiBF_4$ dissolved in acetonitrile similar to the procedure described in here. An oxyfluoride layer was observed on the surface of treated NMC particles, indicating passivation, confirming the hypothesis. LiTFSI, in contrast, has a lower thermal stability with an onset initial temperature at which free acid bound to the salt is released at 36 °C, as shown by Lu et al. [328]. The higher amount of free acid bound to LiTFSI released at lower temperatures in the form of HF could explain the severe surface degradation observed, since HF within fluorine containing electrolyte is known to attack cathode particles forming lithium or transition metal fluorides [330–333]. The discussed results are in good agreement with a recent study by Fu et al. [210].

For blends combined with both, PEO and Li salt, their specific effects seem to compensate each other. While PEO shows to degrade and reduce Ni as described above, the salts seem to compensate the effect. This is especially true for $LiBF_4$, whereas LiTFSI shows to have a little stabilizing effect on the harsh degradation in presence of PEO. Again, this result is in excellent agreement with the recent study by Fu et al. [210], published after the described chemothermal experiments were conducted. The authors show how the oxidative decomposition of the $TFSI^-$ anion and further interaction with the PEO polymer matrix in Li//NMC811 full-cells cause continuous damage to the interfacial stability, and therefore a constant capacity drop [210]. In their approach to effectively counter the drastic degradation seen for for NMC811 in a PEO-LiTFSI matrix, the authors, similar as shown in this thesis, utilize an alternative Li salt, namely, lithium bis(oxalato)borate (LiBOB). Ultimately, the bottleneck of the catholyte seems to be the interface between the active material and the polymer host and how well a passivation of the cathode material is possible by the utilized Li salts. In accordance with Fu et al., Nie et al. have also shown very recently that electrochemical cycling in a voltage window of 3.0 - 4.2 V in Li//LCO-PEO-LiTFSI full-cells, but also to higher cut-off voltages, can lead to the formation of hydrated $TFSI^-$ anions (HTFSI) by a dehydrogenation reaction of PEO. This very strong acid was shown to react with metallic Li on the anode side via a crossover process and generate H_2 gas [199]. Furthermore, a surface catalytic effect of LCO was also shown to substantially facilitate the degradation of PEO [199]. As mentioned in section 2.4.5, coatings of the cathode material can be beneficial as has been observed in the literature [198, 207, 225–227].

5.5.3 A Promising Polymer Matrix: PCL

The reduction of Ni in $Li_{0.3}NCA$ was less severe when blended with PCL, compared to PEO. The main reason for this is the high electrochemical stability against oxidation [166]. For example, Zhang et al. have previously shown how a SPB utilizing a PCL/succinonitrile (SN) polymer can be subjected to an upper cut-off voltage of 4.5 V and shows long-term stability at this voltage [221]. Fonseca et al. have also shown an oxidative stability of up to 5.0 V for the SPE combination of PCL/$LiClO_4$ [220], however, with very limited performance in combination with a Li metal anode and $LiNiCoO_2$ cathode [219]. Furthermore, Bergfelt et al. studied several PCL polymer matrix combinations, among others bare PCL, a block copolymer made of styrene and caprolactone, and a block copolymer made of styrene, caprolactone and trimethylene carbonate. While it was not possible to cycle cells based only on a PCL matrix, which is because of the inability of the PCL electrolyte to passivate the Li metal anode by itself, the triblock copolymer electrolyte showed very promising results at 40 °C and a charge rate of C/5 [223].

The presented *ex-situ* experiments (without electrochemical cycling and in absence of Li metal) show clear benefits of PCL for storage at 80 °C. Also from the *in-situ* conditions as seen in Figure 32d, the conclusion can be made that PCL can possibly pave the way for utilizing Ni-rich cathodes such as NCA in SPBs. PCL also helps to overcome the interfacial degradation that is often considered the bottleneck of SPBs in combination with Ni-rich cathode materials [198, 207, 210, 225], without a need for surface modifications. However, always with a possible way of passivating the Li metal anode. Since all cells utilize the DryLyte separator a dual electrolyte system as presented here, or similar approaches such as a triblock copolymer employed by Bergfelt et al., make this possible. This is not only true for NCA, but also can be transferred to other commercially interesting Ni-rich cathode materials like NMC622 and

NMC811 (see Figure 33). Noticeably, the best stabilities were observed for a lower Ni content as in NMC622, which is due to the fact that with increasing Ni content layered Ni-rich cathode materials become thermally less stable [103]. Especially when in contact with only $LiBF_4$ salt, $Li_{0.3}$NMC622 showed to be highly stable at the surface, subsurface, as well as bulk, possibly due to a possible oxyfluoride layer that is formed. Here, both the higher thermal stability due to lower Ni content, as well as the stabilizing effects and passivation of the oxyfluoride layer result in minimal degradation and reduction of Ni.

To what extent the hypothesized radical reaction plays a role for PCL is unclear. Although from the presented results it is clear that an oxidative degradation of the polymer and inadequate surface passivation seem to be the bottleneck for the difference in PEO and PCL degradation, even with sluggish kinetics.

6 Chemomechanical Stability of NCA in SPBs: Mesoscale Interplay

Analyzing the thermomechanical stability of NCA at high delithiation states provided fundamental knowledge about the exact procedures that happen under thermal stress conditions. The study of the chemothermal stability gave insights into how different polymer and Li salt combinations as well as time and temperature affect the chemical degradation. From this it can be concluded that a complex chemo-thermo-mechanical interplay exists over a wide range of length scales within SPBs. Ultimately, the interdependent structural complexity and chemical heterogeneity collectively govern the local (mesoscale) chemistry and, as a result, critically influence the cell level performance.

In the previous chapters, the focus was set on the materials level and *ex-situ* conditions, i.e., without electrochemical activity. In this chapter, the focus is set on a full-cell working example to understand the chemomechanical interplay of the NCA cathode in SPBs. In order to understand what the main cause for the limited performance is when Ni-rich cathode materials are utilized in SPBs, the polymer Li salt combination that showed the biggest degradation in chapter 5 is analyzed thoroughly, i.e., a Li//NCA-PEO full-cell with LiTFSI salt. Specifically, the morphology and SOC heterogeneities within single secondary NCA particles harvested after electrochemical cycling are investigated, whereby substantial heterogeneities in the Ni valence state (a proxy for SOC) and a loss of structural integrity within the particles are observed.

The experimental results with full-cells show how severe mesoscale, intergranular cracks within NCA particles, cast in a PEO-LiTFSI catholyte, develop after only few cycles. The formation of mesoscale cracks causes a loss of ionic and electrical contact within cathode particles, triggering increases in local impedance and rearrangement of transport pathways for charge carriers. This eventually leads to deactivation of sub-particle level domains in the solid-polymer cell. The obtained information is used to estimate the diffusion deterrent via a numerical model that calculates the disruption in the Li diffusion pathways caused by cracking, and the corresponding impact on primary grain accessibility within the secondary particles. The findings highlight the importance of proper mesoscale strain and defect management in solid-polymer Li batteries.

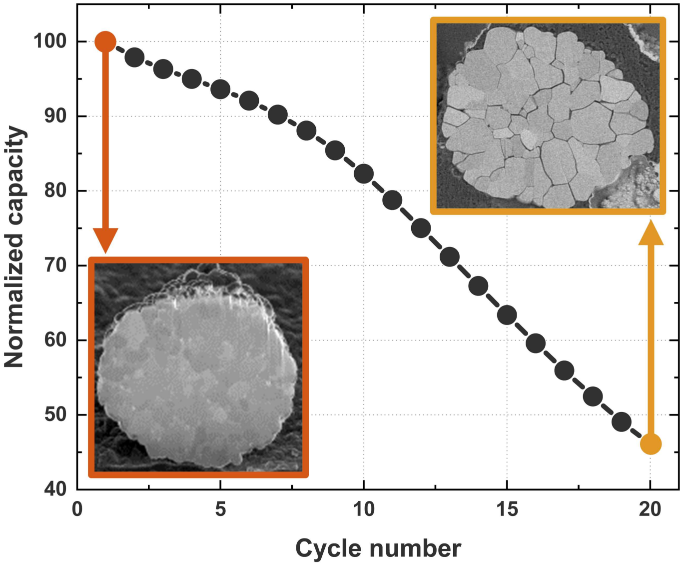

Figure 34: Overview of the capacity fade and mesoscale, intergranular cracks developed in Li//NCA-PEO-LiTFSI cells after only 20 cycles (C/6 rate) at 80 °C.

6.1 Electrochemical Cycling

Figure 35a shows the capacity fade for three Li//NCA-PEO-LiTFSI SPBs upon cycling at a rate of C/6 at 80 °C. After only 20 cycles, a significant drop in capacity was observed for all cycled cells (180.36 mAh/g → 83.09 mAh/g) equal to an average loss of 54% of the initial capacity. Cycling with decreased current density to minimize kinetic effects (C/100, cycle 21) resulted in partial recovery of the lost capacity, whereby a total of 72% of the initially lost capacity could be regained. However, a significant part of the capacity was irreversibly lost and could not be regained (also see Figure 35b). A closer look at how exactly the discharge capacity is fading with increased cycle number, it is visible that for all cells a continuous loss of capacity is visible up to cycle number eight. From cycle number nine onwards, a more steep loss of capacity can be observed.

To support the slow rate cycling measurements, EIS analysis was performed as shown in Figure 35c, which additionally revealed an increase in the first semicircle after only 20 cycles. Quantitatively, an increase of impedance by a factor of more than two was observed ($69.46\ \Omega\mathrm{cm}^2 \rightarrow 153.95\ \Omega\mathrm{cm}^2$). For comparison purposes, Li//NCA cells with the same materials as used in the solid-polymer full-cells were built and cycled with liquid electrolyte (see Figure 35d). For this purpose, the same NCA material, conductive carbon, and Li metal foil were used, only a battery-grade liquid electrolyte was used (for details see section 3.1.3.2). Compared to the solid-polymer NCA-PEO-LiTFSI full-cell, the Li//NCA cells with liquid electrolyte retained 90% of its capacity after 140 cycles. This demonstrates that the obtained capacity loss is not related to the utilized cathode material or Li metal foil, but to the overall cell chemistry and the solid-polymer.

6.2 Synchrotron Characterization Techniques

6.2.1 Bulk XANES Characterization

As discussed in the previous chapters, the Ni redox is the main charge compensator for Li insertion/extraction in NCA, meaning that it can be used as a proxy for SOC in the electrode, as also described in the literature [272]. Hence, to help disambiguate the origin of the drastic capacity loss, hard XAS experiments were conducted at the beamline 4-1 at SSRL to investigate the Ni oxidation state in the bulk cathode material. Figure 36a visualizes the Ni K-edge spectra of as-prepared (pristine) cells, cells charged a single time to 4.2 V, and cells cycled repeatedly (21 cycles; 20 cycles at C/6, last cycle at C/100) and stopped at a fully charged state, i.e., 4.2 V. Ni K-edge spectra collected from the as-prepared cells and

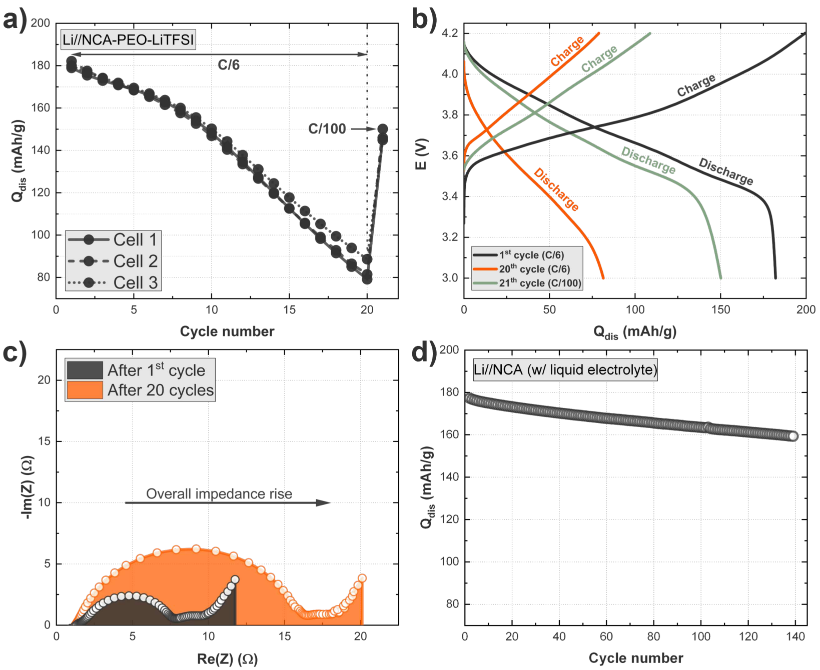

Figure 35: (a) Specific discharge capacities for three Li//NCA-PEO-LiTFSI full-cells as a function of the cycle number cycled at C/6 and 80 °C (last point refers to C/100 slow rate discharge). (b) Charge/discharge curves for the 1st (black), last (20th, orange), and 21st (green) charge/discharge at C/6, C/6, and C/100, respectively. (c) Nyquist plot for a single-charged NCA-PEO-LiTFSI (black) and a cell after 20 cycles (orange) collected at 25 °C. (d) Cyclability plot of a Li//NCA cell containing liquid electrolyte.

cells charged a single time were used as reference spectra for the reduced and oxidized states of Ni, respectively. While the Ni valence state in as-prepared cells is 3+, the Ni valence in single-charged cells is 3.875+. In contrast, the Ni K-edge for cells cycled 20 times appears in between the Ni K-edge for as-prepared and single-charged cells, suggesting a decrease in the average bulk Ni oxidation state in the charged electrodes after 20 cycles. To quantify the visible shift to lower edge energies, a linear fit of the difference of the edge energies between all spectra was calculated and linked to the known oxidation states of Ni. The result shown in Figure 36b depicts that the bulk Ni oxidation state is 3.62+, and therefore roughly 30% reduced after electrochemical cycling of NCA-PEO-LiTFSI full-cells for 20 cycles.

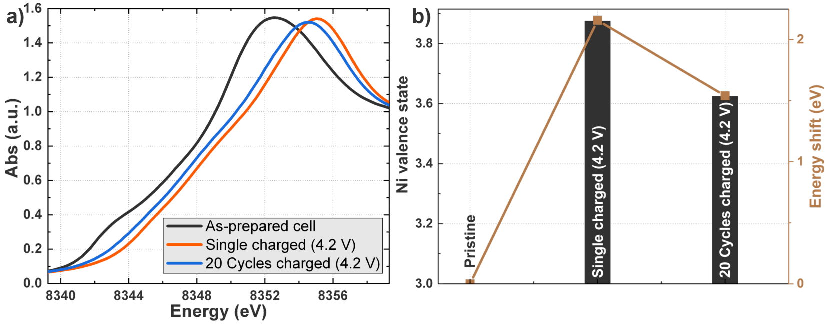

Figure 36: (a) Ni K-edge spectra for pristine, single-charged, and cycled NCA-PEO-LiTFSI full-cells. The Ni absorption edge for full-cells after 20 cycles is shifted to the left indicating that the Ni valence state is reduced compared to cells only charged one time. (b) Ni K-edge energy shift and the concomitant Ni valence state as a result of linear fitting.

While the hard XAS measurement gives an idea about the overall decrease of the Ni oxidation state, it is hard to link the observed Ni reduction to a certain degradation phenomenon. For instance, analyzing the thermomechanical stability upon thermal stress showed how the phase transformation and oxygen evolution are linked to a very strong reduction in the Ni valence state. However, the reduction of Ni in the full cells is not as severe as under thermal abuse conditions. Furthermore, it is not quite clear to what extend the elevated temperature of 80 °C, and how much the high voltage the cells are exposed to, influence the capacity loss. A surface degradation of the cathode active material can be expected if the capacity is lost due to an irreversible oxidation of the polymer electrolyte at the interface with the cathode at high potentials. Also, mesoscale microcracks, especially for the case of a solid-polymer, where the electrolyte cannot really flow easily like a liquid electrolyte, ought to produce the opposite distribution, i.e., surface grains that are still connected to electrolyte will remain redox active, while disconnected grains deep in the particle bulk will not. Finally, delamination or corrosion of the current collector, while increasing the impedance of the cell overall, should not alter the redox activity profile within particles. Therefore, a special focus is set on the two- and three-dimensional distribution of the redox activity and particle morphology in NCA particles harvested from the solid-polymer full-cells. This provides more specific information as to probable origins of the observed capacity loss.

6.2.2 2D-FF-TXM

To identify any mechanical changes inside the secondary NCA particles cycled within a PEO-LiTFSI matrix, for example, in the form of (intergranular) microcracks, 2D-FF-TXM was utilized. With a nominal spatial resolution of around 30 nm, this technique can visualize the evolution of cracks within secondary particles. For statistical accuracy, a large number of secondary particles were imaged (see Figure 37a for a representative image and Appendix Figure A.11 for more particles), which were harvested from fully charged (4.2 V) NCA-PEO-LiTFSI cells after 20 cycles. The contrast in the images is directly proportional to the mass thickness of the particles and is color-coded to the absorption as seen in Figure 37a. The 2D projection images represent the accumulated absorption through the depth of the spherical secondary NCA particles. The overall intensity profile of all particles exhibits higher absorption near the core region due to the relatively larger thickness along the beam direction. An irregular pattern caused by the morphological changes can be clearly observed throughout almost all secondary NCA particles (also compare to Appendix Figure A.11). Severe cracking is particularly evident in the core regions of the harvested secondary particles, as highlighted in the two magnified views in Figure 37a. Although the projection images do not offer any depth resolution, the lateral spatial resolution of around 30 nm can still facilitate the observation of electrochemical cycling-induced

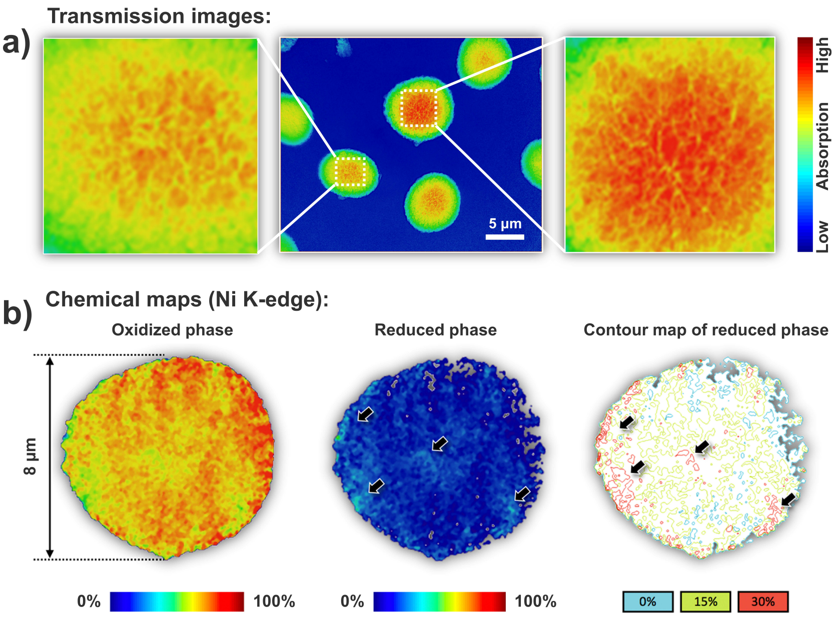

Figure 37: (a) Color-coded 2D-FF-TXM transmission images with enlarged areas for two secondary particles harvested from NCA-PEO-LiTFSI cells cycled 20 times. Due to the sphericity, the overall intensity profiles over the particles show a higher absorption in the core region. The irregular patterns, on the other hand, highlight the fine intergranular cracks developed upon electrochemical cycling. (b) 2D-FF-TXM chemical mapping of a cycled (20 cycles) and fully charged NCA particle harvested from NCA-PEO-LiTFSI full-cells. The spatial distributions of the oxidized phase (left panel) and the reduced phase (middle panel) highlight isolated regions within the secondary particle. The contour map of the reduced phase (right panel) shows the isolated regions in more detail.

cracks in the secondary particles, irrespective of the particle form, diameter, and sphericity. The observed morphological degradation might hinder ion diffusion leading to impedance growth and irreversible capacity loss. In order to understand how the fracturing influences the Li-ion migration within the secondary particles, 2D spatial distributions of the Ni oxidation states in the cycled cells were mapped via a series of 2D-FF-TXM-XANES experiments. Figure 37b offers a direct visualization of the 2D mapping of the XANES data over the Ni K-edge. The spatial distributions of the oxidized (left panel) and the reduced (middle panel) chemical species are calculated by means of linear combination fitting of the spatially resolved XANES data to the spectroscopic fingerprints of the two known principle chemical components, i.e., the Ni K-edge XANES spectra of particles from the single-charged and the pristine cells, respectively. Both maps are color-coded to the relative concentration of the respective species. For instance, for the oxidized phase (left panel), a 100% fit with the oxidized fingerprint derived from the single-charged cell is indicated by a dark red color and no fit by a dark blue color. Similarly, for the reduced phase map (middle panel), a 100% fit with the spectroscopic fingerprint used for fitting (pristine NCA) is indicated by a red color, no fit, by a dark blue color.

Although the analyzed NCA particles were harvested from disassembled NCA-PEO-LiTFSI full-cells in the fully charged state, the maps shown in Figure 37b illustrate that, in both the surface and the core regions within this particle (see black arrows in the middle panel), several domains remain partially discharged. For a better visualization, a contour map of the reduced phase over the investigated particle is shown in the leftmost panel. The contour lines are color coded to the relative concentration of the reduced phase, i.e., blue represents a relative concentration of 0%, green 15% and red 30%. While the entire particle seems partly reduced, the isolated red islands (more reduced) suggest that the partially deactivated domains are developed in a rather heterogeneous manner upon electrochemical cycling.

6.2.3 3D-FF-TXM: Single Particle Characterization

Due to the lack of spatial resolution along the beam direction, the correlation between the morphological degradation and the incomplete sub-particle domain charging is not obvious in the depth averaged 2D-FF-TXM-XANES imaging data. For better understanding of the chemomechanical interplay at the mesoscale (within the secondary NCA particle), 3D-FF-TXM-XANES experiments were carried out on harvested secondary NCA particles. As described in the literature [255, 261], this technique helps to reveal the 3D evolution of the cracks and their successive impact on the heterogeneous distribution of the Ni oxidation state and, thus, that of the SOC within single particles.

The results on a cycled and fully charged secondary NCA particle are shown in Figure 38. Figure 38a presents the 3D rendering of the X-ray nano-tomographic data of a single particle harvested in a fully charged state from a NCA-PEO-LiTFSI SPB after 20 cycles. A few virtual slices through different depth of the particle are highlighted in the middle panel to reveal more morphological details throughout the particle. Unlike for the 2D projection imaging data shown in Figure 37, each virtual slice derived from the 3D-FF-TXM measurement is of single-pixel (around 30 nm) thick. Isolated voids (highlighted by the orange circles) are scattered throughout the entire particle. Additionally, the interconnected crack network (blue arrows) is more distinct near the particle's core. The direct visualization indicates that the cracks likely originate in the core region of the particle and propagate toward the particle surface, as has been also discussed in the literature [334]. In addition to the relatively large crack network (blue arrows), fine and less visible crack patterns can also be observed throughout the particle. These fine cracks are less visible because they are likely near or beyond the spatial resolution limit of the 3D-FF-TXM.

As described above, the spatial resolution of the 3D-FF-TXM-XANES is limited to tens of nanometers, nevertheless, it is capable of correlative structural and chemical imaging, which can offer a direct evidence for the mesoscale interplay of the morphological and chemical evolutions. The electrochemical effect of cracking within the NCA particles is visualized in Figures 38b and c. As with the 2D chemical mapping shown in Figure 37, chemical maps for the oxidized and reduced phase were obtained for the entire NCA particle. This was done by fitting the extracted XANES spectra of every single voxel (32.5 x 32.5 x 32.5 nm^3) to the spectroscopic fingerprints of the pristine NCA and NCA harvested after charging a single time to 4.2 V. Virtual slices of the color-coded 3D renderings

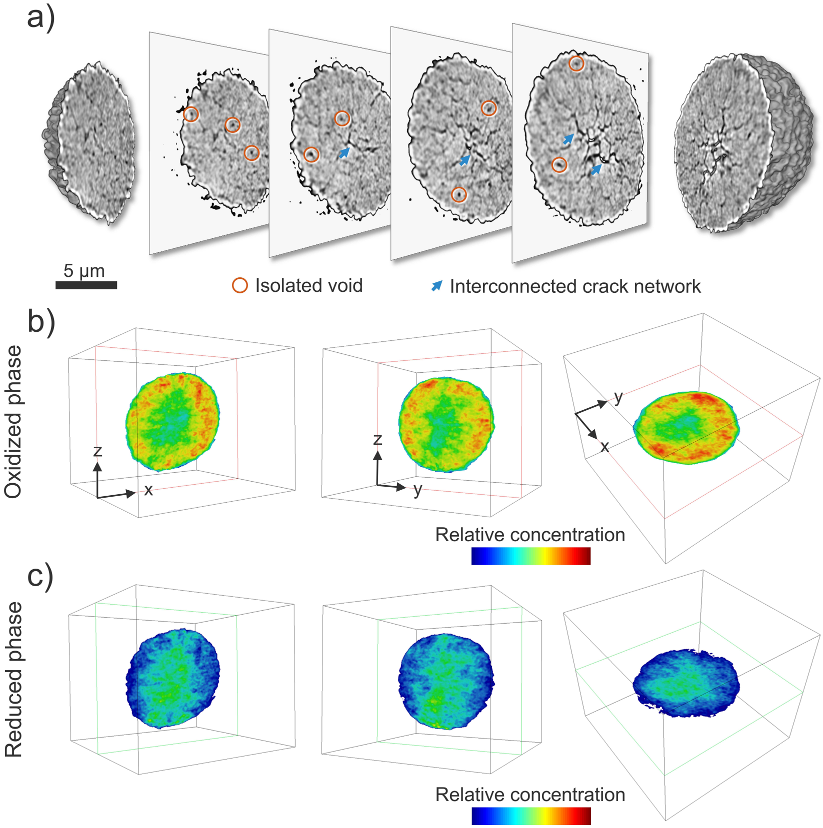

Figure 38: 3D chemical mapping of a cycled NCA particle harvested in the fully charged state (20 cycles) from a NCA-PEO-LiTFSI SPB. (a) 3D rendering of the X-ray nano-tomographic data of the particle collected at 8 keV with four virtual slices showing the complexity of morphological defects. Isolated voids are marked with orange circles, interconnected crack network is marked with blue arrows. (b) and (c) Chemical phase maps of the oxidized and the reduced phase, respectively, over the virtual slices in different orientations.

for the oxidized and reduced phase are illustrated in three orthogonal planes labeled XZ, YZ and XY. The virtual slices in Figures 38b and c depict that, while the particle shell is still electrochemically active, a significantly large, electrochemically less active core has formed after cycling. This observation provides a correlation between the cracks within the particle and the loss of electrochemical activity. The probability of isolation of primary grains within the core of the secondary particle by intergranular cracking is higher than for domains in the outer rim of the secondary particle. Important to note is also that Figure 38b also reveals considerably reduced redox activity in the outermost layer of the secondary particle as well as in the core. The XZ, YZ and XY planes that are shown resemble onions; the surface (a shell) and the core remain similarly reduced, while a layer of redox active NCA sits in between.

In addition to the chemical fingerprinting by means of linear combination fitting, the linear relationship between the Ni K-edge energy and SOC makes it possible to use the determined Ni oxidation state as a proxy for SOC estimations as described in chapter 4. Figure 39a visualizes the Ni K-edge energy distribution over the XZ virtual slice denoted in Figure 38b. The core of the virtual slice shows lower edge energy and SOC, while the value near the particle surface becomes higher, suggesting higher Ni oxidation state and SOC close to the particle surface, which is accordance with the chemical phase maps for the oxidized and reduce phases obtained via linear combination fitting. The depicted edge energy map in Figure 39a was used to calculate the SOC profile throughout the center of the depicted particle. The resulting SOC profile was subsequently linked it to the depth profile of the porosity, to obtain a more quantitative evaluation of the observed core-shell separation. Calculated depth profiles for the porosity and SOC from the 3D data are shown in Figure 39b. In this calculation, the pixels over the 3D volume are regrouped in layers with different depth from the particle surface. The average SOC and the corresponding standard deviation (visualized via error bars) for each layer of pixels is calculated to reveal the depth dependence of the SOC. Similarly, the porosity, which is defined by the volume ratio of the void space within the secondary particles, can also be retrieved by a threshold segmentation of the 3D grayscale map of the entire particle. The porosity is quantified by determining the number of void voxels and dividing this by the total number of voxels of the entire particle volume [134]. As previously mentioned, while the outermost particle shell is significantly reduced, likely due to an electrolyte-electrode interaction, the highest available SOC is in the particle subsurface. Past the subsurface, the SOC continuously decreases as the probing depth approaches the core. Comparing the subsurface SOC to the SOC obtained at the core, one can see a difference of about 20%. Worth noting is also the inverse relationship between the average SOC and the porosity within surface and core of the particle.

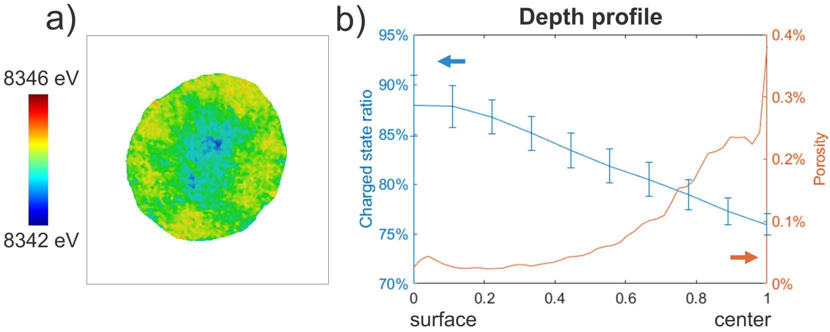

Figure 39: (a) Energy map over the XZ plane denoted in Figure 38b. Color-coding depicts oxidized Ni (red, high SOC) and Ni in a reduced state (blue, low SOC). A clearly reduced particle core in a lower SOC is depicted by the blue color in the very center.(b) Depth profile of the SOC and porosity over the investigated particle using the XZ plane denoted in Figure 38b.

6.3 Morphological Characterization

To further investigate the morphological properties of the cycled and fully charged secondary particles, high resolution BIB-SEM and FIB-SEM tomography were used. Both methods provide deeper morphological insight with a spatial resolution significantly higher than that of the 2D- and 3D-FF-TXM data. Several cross-sections of pristine pouch cells and cells that were cycled 20 times were prepared and probed using BIB-SEM at room temperature. In the same way, several secondary particles were harvested from pristine and cycled cells and subsequently probed using high resolution FIB-SEM tomography.

6.3.1 BIB-SEM Analysis

All analyzed cross-sectional BIB-SEM images derived from pristine cells do not show any kind of cracks, while almost all particles within cycled cross-sections show intergranular cracks. For statistical accuracy, many cross-sections of pristine and cycled cells were analyzed (see Appendix Figures A.12, A.13, and A.14 for pristine, and A.15, A.16, and A.17 for cycled cross-sections). While secondary particles in pristine cells only show densely packed primary grains, cross-sections derived from cells that were cycled 20 times show cracking throughout the particles, with relatively high crack volumes[ix] in the particle centers. Furthermore,

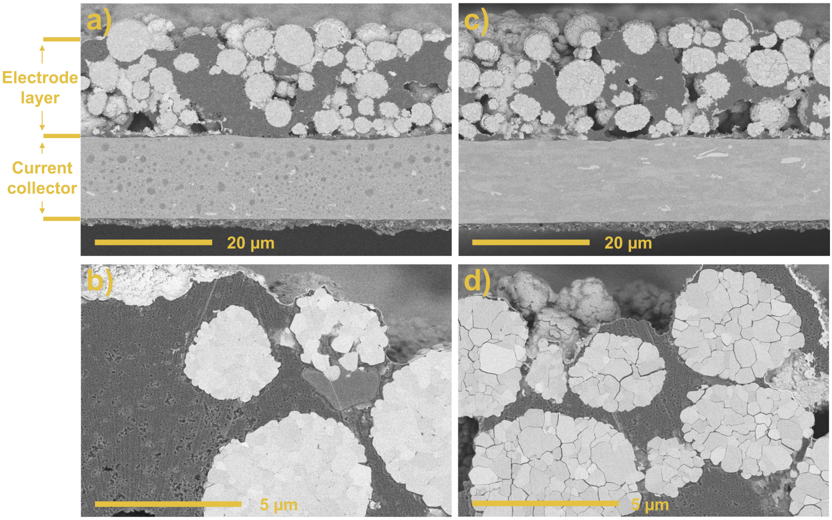

Figure 40: BIB-SEM observation of pristine and cycled (20 cycles) polymer electrode cross-sections. (a) SEM cross-sectional images for pristine NCA-PEO-LiTFSI electrode with higher magnification shown in (b). (c) SEM cross-sectional image for cycled NCA-PEO-LiTFSI electrode with higher magnification shown in (d).

[ix] The focus here was set on the crack volume and areas instead of crack lengths.

primary grains within the core seem to be more isolated due to the surrounding cracks than the grains closer to the surface of the particle, indicative that cracks originate in the center and propagate to the surface, as also suggested in the literature [111, 334], thereby particularly isolating primary grains in the core region of the particle.

6.3.2 FIB-SEM Tomography

The morphology throughout an entire particle, i.e., from surface to the core, was analyzed for pristine NCA particles and particles harvested after 20 cycles via FIB-SEM tomography. The corresponding hundreds of SEM images captured throughout the milling process for each particle were put together in videos. See Video A.3 and A.4 for the milling of pristine NCA particles in mirror mode and TLD mode, respectively [294, 295]; see Video A.5 and A.6 for the milling of harvested NCA particles after 20 cycles, respectively [335, 336].

The videos for pristine particles show that no gap in the grain boundary between primary grains within secondary particles is present; only the isolated voids, scattered throughout the entire particle, also seen in the 3D-FF-TXM results, are nicely visualized via the FIB-SEM tomography. In contrast to this, the cycled particles show intergranular cracks, but no intragranular gaps, or any kind of mesopores as a result of the elevated temperature or thermal spikes. Interestingly, the FIB-SEM tomography of cycled NCA particles did not show any polymer electrolyte penetrating the intergranular cracks and openings in the surface. Hence, assuming that there is no migration of polymer electrolyte filling intergranular cracks, a geometrical estimation of the increase in tortuosity of diffusion pathways and their effect on cell resistance can be estimated using FIB-SEM tomographs. For this reason, several particles of cycled cells were harvested and analyzed by serial-sectioning and imaging using FIB-SEM tomography. The so obtained secondary electron and backscattered electron images from serial sectioning were analyzed using a numerical model.

The utilized model to calculate the increase in crack-induced Li diffusion

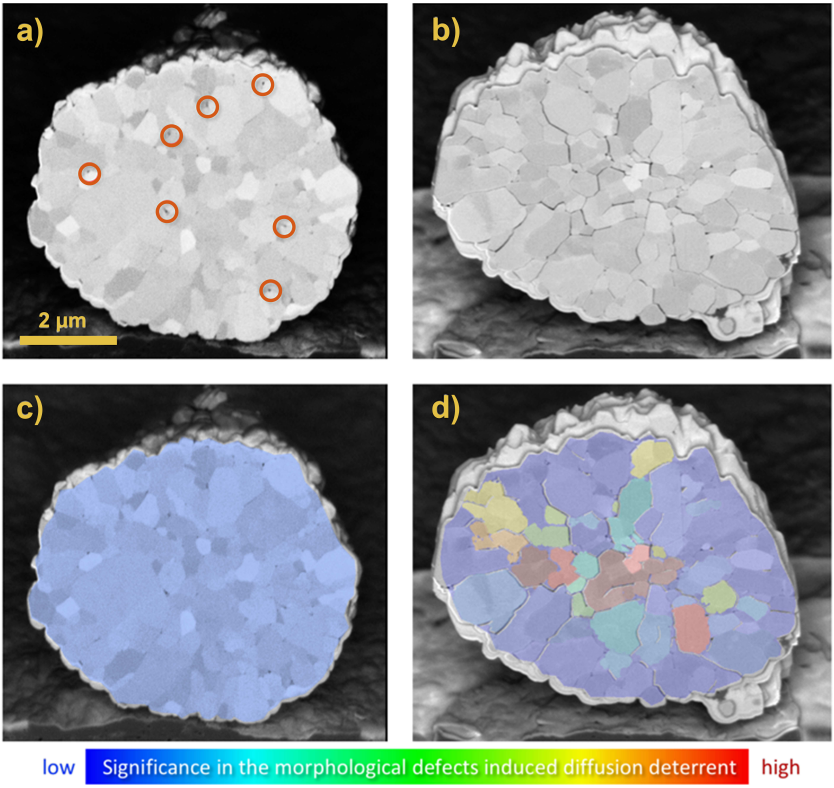

Figure 41: SEM cross-sectional images after FIB milling for (a) a pristine NCA secondary particle and (b) a harvested NCA secondary particle after cycling. Isolated morphological defects (see orange circles in panel (a)) are observed in the pristine particle, while interconnected cracks are observed in the cycled particle. Panels (c) and (d) are the corresponding slices color coded to the quantification of the degree of crack-induced diffusion deterrent for individual grains within the secondary particles.

pathways is based on a numerical algorithm developed by Xia et al. at the SSRL [134]. Although developed for tomographic data obtained from 3D-FF-TXM, the numerical model is readily applicable to FIB-SEM tomographic data as well, as described by the authors [134], and shown in this thesis. As seen in the FIB-SEM tomographs, in the pristine state, most of the primary particles are seamlessly connected. This is expected since most cathode materials of commercial quality are prepared via a co-precipitation and subsequent sintering at > 700 °C. Nevertheless, some small isolated voids are seen in the particle as highlighted by the orange circles. Compared to this, substantial intergranular cracks are observed for cycled particles, which has been summarized in Figure 41a and b, respectively. For the calculation of the crack-induced Li diffusion pathways, first the outer surface of the particle, where the charge transfer happens, is defined, and the identified surface pixels are assigned a value of 2 [134]. After this identification of surface pixels, a segmentation of the solid phase and crack voxels is conducted and values of 1 and -1 are assigned to each, respectively [134]. Lastly, the values for all solid phase voxels adjacent to the current front are reassigned, starting from the original surface of the secondary particle [134]. This iteration starts from the very surface voxel layer and moves inside of the secondary particle: (I) if the solid phase voxel is vertically adjacent to the current iteration front its value is set to x + 1, with x being the value of the current iteration front; (II) if the voxel is 2D diagonally adjacent to the current front its value is set to x + $\sqrt{2}$; (III) if the voxel is 3D diagonally adjacent to the current front its value is set to x + $\sqrt{3}$; (IV) after reassigning each value for the solid phase voxels, the iteration moves one front ahead and continues [134]. By numerically solving this ‘3D maze’ (as defined by the cracking pattern), starting from every single grain, the geometrically optimal Li diffusion pathway can be determined for every grain within the secondary particle.

The difference in the optimal diffusion length before and after the crack formation is presented in Figures 41c and d. The cracks effectively act as physical barriers that increase the tortuosity of Li diffusion in the active material. Here it is important to annotate, that Figure 41d is essentially a differential map, derived by calculating the absolute diffusion length for every grain before and after crack formation. It highlights the cracking-caused local differences in ionic conductivity. The color coding represents the degree of cracking-induced diffusion deterrent, and is not directly proportional to the absolute diffusion length for each individual grain. The calculated results shown in Figure 41c, on the contrary, illustrate that in pristine particles the pre-existing isolated voids have negligible impact on the Li-ion diffusion. The interconnected cracks, on the other hand, cause significant rearrangement of the Li diffusion pathway, increasing values of the diffusion deterrent as shown in Figure 41d. Generally speaking, the center of the particle is more severely impacted, in good agreement with the 3D-FF-TXM data presented above.

6.4 Interpretation and Discussion

6.4.1 Electrochemical Performance

The observed stark capacity loss led to the conclusion that evidently there exist degradation mechanisms in NCA-PEO-LiTFSI cells that lead to a more drastic capacity loss than for their NCA-PCL-$LiBF_4$ cell counterparts, but especially compared to their liquid cell counterparts.

Regained capacity upon slow rate cycling, which minimizes kinetic effects and, therefore, allows greater access to available capacity in regions of high impedance, along with the increased impedance, as a result of the EIS analysis, suggest an increase in the impedance of ion diffusion and electron transfer after 20 cycles. Ultimately, the greater part of these degradation mechanisms in the short-term are associated with impedance growth rather than simple decomposition of active material, and as seen in the morphology of the analyzed particles, are mainly a result of intergranular cracking and concomitant partial to full primary grain disconnection. Nevertheless, besides the mechanical failure of the NCA material via fracturing, thermal degradation of the active material at 80 °C [98, 337], the well-established electrochemical oxidation of the PEO electrolyte above 4 V [315], delamination of interfaces due to gas generation, and corrosion of the Al current collector [338], are all plausible mechanisms that may contribute to impedance growth and capacity loss.

Considering the thermal degradation at 80 °C and a cycling rate of C/6 it can be said that 20 full cycles take 10 days, at which, as shown in chapter 5, NCA in contact with PEO-LiTFSI shows higher Ni reduction (Figure 31) and concomitant degrees of aging than for NCA in contact with PCL-$LiBF_4$. This means that beside the morphological defects the reduction of Ni and attendant layered-spinel-rocksalt phase transition during electrochemical cycling does also contribute to the capacity loss. This is accelerated by the presence of PEO and LiTFSI, a combination that showed to be the most chemothermal deteriorating. Here it is important to emphasize that the layered-spinel-rocksalt transformation is a chemothermal effect rather than an electrochemical cycling-induced one, as extensively discussed in chapter 5. The chemothermal study and a comparison of the cycling stability of NCA embedded in a PEO-LiTFSI and a PCL-$LiBF_4$ matrix in the previous chapter further revealed that the oxidative stability of the utilized polymer matrix can possibly be influential on the electrochemical cycling. Therefore, the higher oxidative instability of PEO is expected to contribute to the irreversible loss of capacity, especially under active electrochemical cycling conditions, with a continuous sweep of the potential at the cathode side from high to low and back.

The absence of any kind of mesopores or intragranular cracks, as observed in chapter 4, is indicative that the electrochemical cycling at 80 °C does not cause any thermal spikes because of mechanical stress or repetitive phase transition within the material. A reduction of Ni because of thermal spikes above the operating temperature can therefore be excluded, when considering the results obtained in chapter 4.

6.4.2 Cycling-Induced Morphological and Chemical Changes

It may be expected that the different degradation mechanisms are varyingly pronounced throughout a single NCA secondary particle as well as a cell. The analysis of the 2D/3D distribution of redox-active Ni in cycled NCA particles, and the detailed analysis of the intergranular cracking provides some useful information on this. The reduction of the bulk Ni oxidation state suggests diminished charging of the cathode, which could be caused by a phase transformation, and/or disconnection and isolation of active material in the composite cathode. This is supported by the isolated regions of reduced Ni seen in the 2D-FF-TXM images (Figure 37). Furthermore, correlating intergranular cracks within the particle and the loss of electrochemical activity via 3D-FF-TXM suggest that the probability of isolation of primary grains within the core of the secondary particle is higher than for domains in the outer rim of the secondary particle. The resulting partially deactivated inner grains can no longer fully participate in the intercalation process, even when being charged with a very slow C-rate. Hence, totally disconnected primary grains are 'frozen' in a reduced Ni state, whereas partially connected primary grains can only pariticpate in the (de-)intercalation of Li when cycled very slowly. With this, the isolated regions of reduced Ni seen in the 2D-FF-TXM (Figure 37) and the large inactive core seen in the 3D-FF-TXM (Figure 38) can be explained.

For the very thin outer shell of reduced Ni, particularly seen in the chemical phase maps in Figure 38b, it can be hypothesized that the diminished redox activity in the shell and the core come from two different degradation phenomena. Reduction of the outermost layer, as previously discussed, is consistent with electrode-electrolyte interaction on the surface of secondary particles and the associated electrolyte decomposition and concomitant reduction of Ni as is also observed in conventional LIBs. In the case of PEO, which shows oxidative instability above 4 V, the surface reduction of the cathode particle might be more severe compared to conventional LIBs, which was particularly shown for the chemothermal stability in chapter 5. By contrast, the core of the particle does not interface directly with the polymer electrolyte. Although the migration of oxygen from the bulk could induce a Ni reduction via phase transformation in the bulk (see discussion in chapter 5), the tomographic and morphological data both suggest that the core is more severely affected by intergranular cracking. This causes (partial) isolation of primary particles near the core region. Although the electrochemical reaction driving force is applied externally, the core is not able to complete the delithiation process. The core-shell separation is clearly visualized by the 3D-FF-TXM-XANES (Figure 38) measurements that eliminate the uncertainty in the depth averaged measurements (2D, Figure 37).

How the described degradation phenomena causing the capacity loss transits throughout the particle is given by the SOC analysis. Since the SOC shows a continuous decrease, cracking seems to affect redox throughout the entire particle, despite the different distribution of the degradation mechanism. Losses seem to not be confined to the innermost region where the tomography shows the most severe cracking, which has to do with increased particle porosity throughout the particle's depth. Porosity is part of the structural reconstruction upon cycling and is especially prominent within the interconnected crack network shown in the core. The inverse correlation between depth profile of the SOC and that of the porosity is worth noting, as it provides strong and direct evidence for the loss of capacity through cracking. Increased porosity leads to disruption of Li diffusion pathways and hence makes sub-particle domains less electrochemically active. While the severe crack network is very distinct near the particle's center, the porosity calculations demonstrate an impact that clearly goes beyond the particle core.

6.4.3 Intergranular Cracking-induced Li Diffusion Deterrent

The rapid capacity fading observed during cycling of NCA-PEO-LiTFSI cells can be ascribed to the vigorous intergranular cracking observed in all analyzed cross-sections and single particle tomographies, as discussed above. This degree of cracking should lead to capacity fade, since contact between active regions is lost upon cycling and thereby spatial Li-ion transport pathways are deactivated. Although many studies have investigated particle-cracking-induced cathode degradation in LIBs with liquid electrolytes, not much is known about these phenomena in solid-polymer battery configurations. As liquid electrolyte can infiltrate cracks, diffusion may be preserved due to the migration of Li ions through newly developed active interfaces [134]. For similar reasons, Li and active material loss due to formation of these new interfaces may play a larger role. By comparison, loss of ionic connectivity is expected to dominate the system in solid-polymer batteries. Poor contact between solid electrolyte and the outer surface of the secondary active material particle may result in higher current density heterogeneity, thereby hastening the onset of stress-induced particle fracture compared to conventional liquid electrolyte-based cells. Poor effective diffusion of Li in the fractured particles without liquid electrolyte could further accelerate degradation as the better-connected portions of the particle experience ever increasing local current density.

To illustrate these phenomena a little more fully, Figure 42 summarizes the understanding of the impact of intergranular cracks on electron transportation and Li-ion diffusion pathways in secondary particles in liquid and solid-polymer cells. Panel a shows the geometrically optimal pathways for both charge carriers upon charging of the battery, while panel b shows the change in pathways in solid-polymer batteries upon intergranular cracking. While the geometrically shortest pathways are accessible by charge carriers in a pristine NCA particle, both electrons and Li ions (with several orders of magnitude slower migration than electrons) must detour along a more tortuous path in a fractured particle. It is hypothesized that, in contrast to solid-polymer-based cells, intergranular cracks in conventional LIBs are filled with liquid electrolyte that facilitates Li^+ transport via two charge transfer steps (host → electrolyte → host) at intergranular cracks (Figure 42c). To support this hypothesis, a SEM-EDS experiment was carried out with cycled NCA particles that showed extensive cracks on their surface. Harvested, cycled particles were soaked in 1 M $LiPF_6$ dissolved in a mixture of EC and DEC (50:50, v/v) for 3 days, and subsequently washed with salt free EC:DEC (50:50, v/v). The particles were then subjected to an EDS analysis to detect elements within intergranular cracks originating from electrolyte contact, which shows a clear P signal within intergranular cracks (see Appendix Figure A.18, which indicate, that electrolyte diffuses into the cracks of secondary NCA particles.

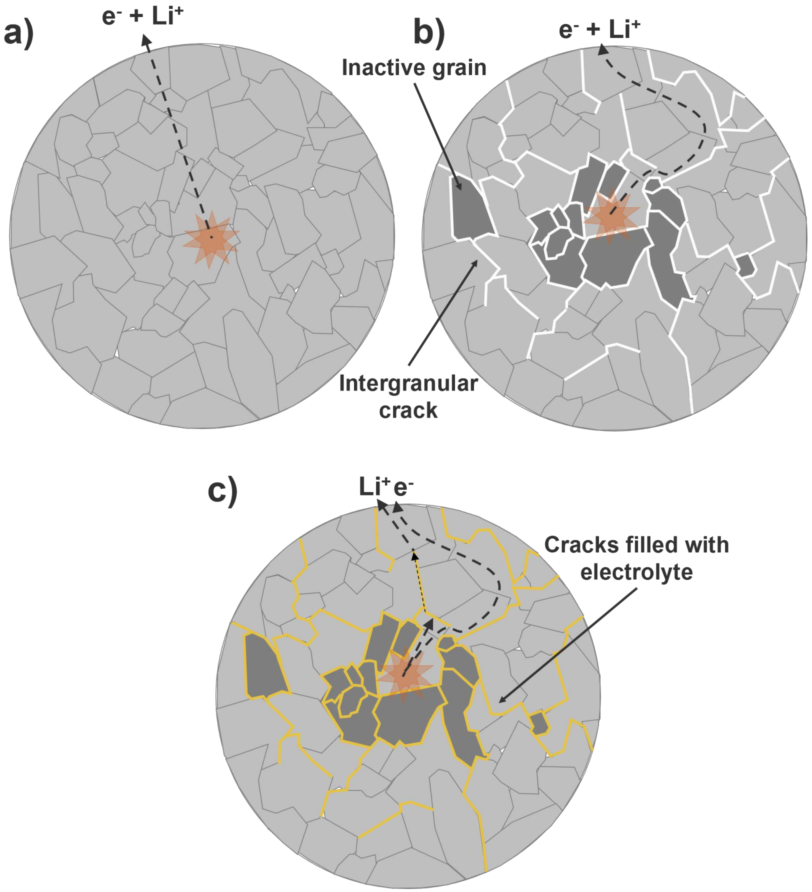

Figure 42: Schematic 2D models of secondary NCA particles. (a) Pristine secondary NCA particle. Charge carriers transport and diffusion can happen without any barriers and the shortest geometrically ideal paths are taken. (b) Secondary NCA particle with intergranular cracks in absence of electrolyte. Charge carriers get trapped within inactive grains and have to detour from the geometrically optimal path. (c) Secondary NCA particle with intergranular cracks in presence of liquid electrolyte. Electrolyte can fill the cracks and only electrons have to detour the cracks, while Li ions can still diffuse through the electrolyte-filled cracks.

In the case of liquid electrolyte, the Li-ion diffusion is faster than in a fractured particle embedded in a solid electrolyte, but the effective diffusivity is lower than in a pristine particle. However, the electrolyte does not conduct electrons, which leads to detouring of electrons due to barriers formed by the intergranular cracks. In addition, the additional charge-transfer resistance at the interfaces (host $\rightarrow$ electrolyte $\rightarrow$ host) could also influence Li-ion transportation. The result is a mixture of both irreversible capacity loss as well as significant growth of cell impedance, which is consistent with what was observed in the electrochemical data: when charging using a very low C-rate such as C/100, 28% capacity could not be regained, indicating that some primary particles have essentially become isolated. The probability of deactivation of primary grains is higher within the core region than over the outer rim of the particle.

7 Summary and Outlook

In the first part, the thermomechanical stability of chemically delithiated NCA cathode material, which was continuously heated to 450 °C, was analyzed and the chemical and morphological changes retrieved. The findings indicate oxygen evolution, phase transformation, and continuous reduction of surface, subsurface, and bulk Ni, and inter- as well as intragranular cracking and the creation of mesopores upon heating. While in good agreement with what has been reported previously in the literature for the thermal degradation of delithiated NCA, it was additionally shown that oxygen evolution causes mesopores upon heating between 300 - 350 °C. This creates a pathway for the release of lattice oxygen from the bulk and surface. Furthermore, it was observed, that some of the mesopores seem to follow intragranular cracks that appear in somewhat parallel manner within primary grains. These mesopores most probably are part of the compensation of the internal pressure build up due to oxygen evolution. However, internal pressure build up further decreases the volume of intergranular cracks suggesting that mesopores lead to a volume expansion of primary grains. While the chemical and morphological changes appear at temperatures higher than 200 °C, delithiated NCA shows good short-term stability for temperatures up to 200 °C.

To get an idea about the chemothermal stability, hard and soft X-ray absorption spectroscopy were used to probe the Ni oxidation state changes of chemically delithiated NCA aged alone, and in a variety of combinations with polymer (PEO or PCL) and Li salt ($LiBF_4$ or LiTFSI) in the second part of this thesis. By analyzing the oxidation state changes for Ni located at the surface, subsurface, and in the bulk regions it was shown, how the chemothermal degradation of the active material begins at the surface and seems to propagate into the bulk material. Depending on the additional components (polymer and/or Li salt) blended with the delithiated cathode active material, the surface reconstruction at 80 °C can be hindered to a certain degree. Blending in polymers accelerates Ni reduction at the surface and subsurface, and in the bulk, particularly in the case of PEO. In contrast, blending in only Li salts with the delithiated cathode materials results in less Ni reduction in the case of $LiBF_4$, and more distinct reduction for LiTFSI. In terms of the ‘use case’, i.e., a SPB with cathode active material, polymer and Li salt, PCL-$LiBF_4$ was identified as a promising catholyte for Li//NCA polymer cells and showed the importance of the chemothermal interplay of all three components within the cell. The methodology of a quick screening of the Ni reduction within the cathode active material using soft and hard XAS was shown to be directly applicable into SPB development via electrochemical cycling.

Finally, 2D/3D-FF-TXM were used to probe secondary NCA particles harvested from cycled NCA-PEO-LiTFSI polymer batteries. This methodology allowed to quantify the morphological and electrochemical changes occurring in a real SPB. Additionally, high resolution BIB- and FIB-SEM data and a numerical model were used to estimate the deterioration in effective Li-diffusivity in fractured particles. The obtained results suggest that the absence of liquid electrolyte severely affects transport of charge carriers in fractured particles and may also hasten and accelerate fracture due to lower uniformity in current density. Intergranular cracks significantly increase diffusion path lengths of both charge carriers, electrons and Li ions. In liquid LIBs, electrolyte filling the cracks should maintain Li-ion transport pathways but not electron transport pathways. In solid-state batteries, intergranular cracking compromises not only the electronic pathways, but also the ionic pathways. Furthermore, intergranular cracking in NCA particles cast in a polymer matrix seems to lead to isolated and inactivated primary grains within the core of secondary particles, leading to capacity fade and reduced Ni oxidation state. While the subsurface of secondary NCA particles stays somewhat intact and available for (de-)intercalation of Li ions, the core of the particle loses a significant amount of its activity and contributes to the loss of capacity and rate capability, partially because of full isolation of primary grains. In comparison to conventional LIBs, the amount of intergranular cracking observed for the solid-polymer cells was more severe, and the effect of cracking on capacity fade is very rapid, at least for very deteriorating polymer and Li salt combinations such as PEO-LiTFSI. The detailed mechanism for the cause of rapid crack formation in NCA-PEO polymer cells is not yet wholly clear, but there are several possibilities. As observed in conventional LIBs, mechanical strain arising from lattice breathing or anisotropic volumetric changes upon cycling can lead to cracks in NCA particles. Oxygen release from the layered oxide, potentially exacerbated by elevated operating temperature under long-term cycling conditions, can lead to both pressure buildup and phase transformation to a rocksalt structure, which can also cause mechanical failure. These mechanisms may be exacerbated in the polymer setting, due to the pliability of the polymer electrolytes, the elevated temperature, the chemomechanical interplay with degrading PEO, high cut-off voltages, or other effects that are not yet known.

Looking forward, more studies on the promising PCL matrix should be conducted, as has also been highlighted by Bergfelt et al. [223]. The path towards SPBs combined with high-voltage Ni-rich cathode materials seems to be a feasible one if more efforts are made, especially also in finding suitable polymer/Li salt combinations. As has been demonstrated, polymer/Li salt complexes known to have good electrochemical stabilities such as PEO-LiTFSI [339], must be reworked in order to pave the way for SPBs in combination with industry-preferred Ni-rich cathode materials like NCA. Additionally, possible ways of avoiding intergranular cracking such as the use of single-crystalline particles [340], ALD coating [341], and the use of a Li salt in combination with a low viscosity polymer which could infiltrate cracks, still has to be studied. This work provides a first foundation for future works to build upon this. This work demonstrated that the thermomechanical stability of delithiated NCA, as long as there are no thermal spikes of any source, is not the bottleneck of SPBs operated at elevated temperatures. Furthermore, it was presented that the chemothermal stability of the catholyte is as important as the electrochemical stability under active cycling conditions. Therefore, this work provides a first foundation for future works to build upon.

References

[1] R. Korthauer, *Handbuch Lithium-Ionen-Batterien*, Springer Vieweg, Berlin/Heidelberg, 1st edn., 2013, pp. 3–43.

[2] A. Perner and J. Vetter, in *Advances in Battery Technologies for Electric Vehicles*, ed. B. Scrosati, J. Garche and W. Tillmetz, Elsevier, Cambridge, 2015, pp. 173–190.

[3] B. Dunn, H. Kamath and J.-M. Tarascon, Electrical Energy Storage for the Grid: A Battery of Choices, *Science*, 2011, **334**, 928–935.

[4] J. Li, Z. Du, R. E. Ruther, S. J. An, L. A. David, K. Hays, M. Wood, N. D. Phillip, Y. Sheng, C. Mao, S. Kalnaus, C. Daniel and D. L. Wood, Toward Low-Cost, High-Energy Density, and High-Power Density Lithium-Ion Batteries, *The Journal of The Minerals, Metals & Materials Society (TMS)*, 2017, **69**, 1484–1496.

[5] T. Kim, W. Song, D. Y. Son, L. K. Ono and Y. Qi, Lithium-ion batteries: outlook on present, future, and hybridized technologies, *Journal of Materials Chemistry A*, 2019, **7**, 2942–2964.

[6] Department of Energy, *EV Everywhere Grand Challenge: Road to Success (accessed: 07/28/2020)*, 2014, http://energy.gov/sites/prod/files/2014/02/f8/eveverywhere_road_to_success.pdf.

[7] Department of Energy, *EV Everywhere Grand Challenge - Blueprint (accessed: 07/27/2020)*, 2013, https://www.energy.gov/sites/prod/files/2014/02/f8/eveverywhere_blueprint.pdf.

[8] H. Hao, X. Cheng, Z. Liu and F. Zhao, China's traction battery technology roadmap: Targets, impacts and concerns, *Energy Policy*, 2017, **108**, 355–358.

[9] J. Duan, X. Tang, H. Dai, Y. Yang, W. Wu, X. Wei and Y. Huang, Building Safe Lithium-Ion Batteries for Electric Vehicles: A Review, *Electrochemical Energy Reviews*, 2020, **3**, 1–42.

[10] S. T. Myung, F. Maglia, K. J. Park, C. S. Yoon, P. Lamp, S. J. Kim and Y. K. Sun, Nickel-Rich Layered Cathode Materials for Automotive Lithium-Ion Batteries: Achievements and Perspectives, *ACS Energy Letters*, 2017, **2**, 196–223.

[11] D. Andre, S.-J. Kim, P. Lamp, S. F. Lux, F. Maglia, O. Paschos and B. Stiaszny, Future generations of cathode materials: an automotive industry perspective, *Journal of Materials Chemistry A*, 2015, **3**, 6709–6732.

[12] B. Commarieu, A. Paolella, J.-C. Daigle and K. Zaghib, Toward high lithium conduction in solid polymer and polymer-ceramic batteries, *Current Opinion in Electrochemistry*, 2018, **9**, 56–63.

[13] M. M. Besli, A. K. Shukla, C. Wei, M. Metzger, J. Alvarado, J. Boell, D. Nord-

lund, G. Schneider, S. Hellstrom, C. Johnston, J. Christensen, M. M. Doeff, Y. Liu and S. Kuppan, Thermally-driven mesopore formation and oxygen release in delithiated NCA cathode particles, *Journal of Materials Chemistry A*, 2019, **7**, 12593–12603.

[14] M. M. Besli, C. Usubelli, M. Metzger, S. Hellstrom, S. Sainio, D. Nordlund, J. Christensen, G. Schneider, M. M. Doeff and S. Kuppan, Long-term chemothermal stability of delithiated NCA in polymer solid-state batteries, *Journal of Materials Chemistry A*, 2019, **7**, 27135–27147.

[15] M. M. Besli, S. Xia, S. Kuppan, Y. Huang, M. Metzger, A. K. Shukla, G. Schneider, S. Hellstrom, J. Christensen, M. M. Doeff and Y. Liu, Mesoscale Chemomechanical Interplay of the $LiNi_{0.8}Co_{0.15}Al_{0.05}O_2$ Cathode in Solid-State Polymer Batteries, *Chemistry of Materials*, 2019, **31**, 491–501.

[16] P. Kurzweil and O. K. Dietlmeier, *Elektrochemische Speicher*, Springer Vieweg, Wiesbaden, 1st edn., 2015, pp. 157–215.

[17] S. W. Mayer and D. E. McKenzie, Lightweight secondary battery, *US Patent No.: US3185590A*, 1965.

[18] M. V. Reddy, A. Mauger, C. M. Julien, A. Paolella and K. Zaghib, Brief history of early lithium-battery development, *Materials*, 2020, **13**, 1–9.

[19] D. Fouchard and L. Lechner, Analysis of safety and reliability in secondary lithium batteries, *Electrochimica Acta*, 1993, **38**, 1193–1198.

[20] K. Brandt, Historical development of secondary lithium batteries, *Solid State Ionics*, 1994, **69**, 173–183.

[21] W. Xu, J. Wang, F. Ding, X. Chen, E. Nasybulin, Y. Zhang and J.-G. Zhang, Lithium metal anodes for rechargeable batteries, *Energy Environ. Sci.*, 2014, **7**, 513–537.

[22] A. Manthiram, X. Yu and S. Wang, Lithium battery chemistries enabled by solid-state electrolytes, *Nature Reviews Materials*, 2017, **2**, 16103.

[23] P. Mozur, *Galaxy Note 7 Fires Caused by Battery and Design Flaws, Samsung Says (accessed: 07/27/2020)*, 2017, https://www.nytimes.com/2017/01/22/business/samsung-galaxy-note-7-battery-fires-report.html.

[24] P. Sun, R. Bisschop, H. Niu and X. Huang, A Review of Battery Fires in Electric Vehicles, *Fire Technology*, 2020, **56**, 1361–1410.

[25] P. Albertus, S. Babinec, S. Litzelman and A. Newman, Status and challenges in enabling the lithium metal electrode for high-energy and low-cost rechargeable batteries, *Nature Energy*, 2018, **3**, 16–21.

[26] K. Xu, Nonaqueous Liquid Electrolytes for Lithium-Based Rechargeable Batteries, *Chemical Reviews*, 2004, **104**, 4303–4418.

[27] K. Xu, Electrolytes and Interphases in Li-Ion Batteries and Beyond, *Chemical Reviews*, 2014, **114**, 11503–11618.

[28] T. Placke, R. Kloepsch, S. Dühnen and M. Winter, Lithium ion, lithium metal, and alternative rechargeable battery technologies: the odyssey for high energy density, *Journal of Solid State Electrochemistry*, 2017, **21**, 1939–1964.

[29] J. C. Bachman, S. Muy, A. Grimaud, H.-H. Chang, N. Pour, S. F. Lux, O. Paschos, F. Maglia, S. Lupart, P. Lamp, L. Giordano and Y. Shao-Horn, Inorganic Solid-State Electrolytes for Lithium Batteries: Mechanisms and Properties Governing Ion Conduction, *Chemical Reviews*, 2016, **116**, 140–162.

[30] C. Sun, J. Liu, Y. Gong, D. P. Wilkinson and J. Zhang, Recent advances in all-solid-state rechargeable lithium batteries, *Nano Energy*, 2017, **33**, 363–386.

[31] X. He, *Solid-State and Polymer Batteries 2020-2030: Technology, Patents, Forecasts, Players (accessed: 07/29/2020)*, 2020, https://www.idtechex.com/en/research-report/solid-state-and-polymer-batteries-2020-2030-technology-patents-forecasts-players/763.

[32] Volkswagen AG, *Volkswagen increases stake in QuantumScape (accessed: 08/05/2020)*, 2020, https://www.volkswagenag.com/en/news/2020/06/volkswagen-increases-stake-in-quantumscape.html.

[33] A. Mauger, M. Armand, C. M. Julien and K. Zaghib, Challenges and issues facing lithium metal for solid-state rechargeable batteries, *Journal of Power Sources*, 2017, **353**, 333–342.

[34] K. Momma and F. Izumi, VESTA 3 for three-dimensional visualization of crystal, volumetric and morphology data, *Journal of Applied Crystallography*, 2011, **44**, 1272–1276.

[35] S. Randau, D. A. Weber, O. Kötz, R. Koerver, P. Braun, A. Weber, E. Ivers-Tiffée, T. Adermann, J. Kulisch, W. G. Zeier, F. H. Richter and J. Janek, Benchmarking the performance of all-solid-state lithium batteries, *Nature Energy*, 2020, **5**, 259–270.

[36] J. Betz, G. Bieker, P. Meister, T. Placke, M. Winter and R. Schmuch, Theoretical versus Practical Energy: A Plea for More Transparency in the Energy Calculation of Different Rechargeable Battery Systems, *Advanced Energy Materials*, 2019, **9**, 1–18.

[37] K. G. Gallagher, S. E. Trask, C. Bauer, T. Woehrle, S. F. Lux, M. Tschech, P. Lamp, B. J. Polzin, S. Ha, B. Long, Q. Wu, W. Lu, D. W. Dees and A. N. Jansen, Optimizing Areal Capacities through Understanding the Limitations of Lithium-Ion Electrodes, *Journal of The Electrochemical Society*, 2016, **163**, A138–A149.

[38] E. J. Berg, C. Villevieille, D. Streich, S. Trabesinger and P. Novák, Rechargeable Batteries: Grasping for the Limits of Chemistry, *Journal of The Electrochemical Society*, 2015, **162**, A2468–A2475.

[39] K. Field, *Tesla Model 3 Battery Pack & Battery Cell Teardown Highlights Performance Improvements (accessed: 08/05/2020)*, 2019,

https://cleantechnica.com/2019/01/28/tesla-model-3-battery-pack-cell-teardown-highlights-performance-improvements/.

[40] M. S. Kim, J. H. Ryu, Deepika, Y. R. Lim, I. W. Nah, K. R. Lee, L. A. Archer and W. Il Cho, Langmuir-Blodgett artificial solid-electrolyte interphases for practical lithium metal batteries, *Nature Energy*, 2018, **3**, 889–898.

[41] C. Niu, H. Lee, S. Chen, Q. Li, J. Du, W. Xu, J. G. Zhang, M. S. Whittingham, J. Xiao and J. Liu, High-energy lithium metal pouch cells with limited anode swelling and long stable cycles, *Nature Energy*, 2019, **4**, 551–559.

[42] X. Q. Zhang, T. Li, B. Q. Li, R. Zhang, P. Shi, C. Yan, J. Q. Huang and Q. Zhang, A Sustainable Solid Electrolyte Interphase for High-Energy-Density Lithium Metal Batteries Under Practical Conditions, *Angewandte Chemie - International Edition*, 2020, **59**, 3252–3257.

[43] Battery500 Consortium, *Battery500: Progress Update (accessed: 08/11/2020)*, 2020, https://www.energy.gov/eere/articles/battery500-progress-update.

[44] S. Baksa and W. Yourey, Consumer-Based Evaluation of Commercially Available Protected 18650 Cells, *Batteries*, 2018, **4**, 45.

[45] Benchmark Mineral Intelligence, *Panasonic reduces Tesla's cobalt consumption by 60% in 6 years... (accessed: 11/14/2020)*, 2018, https://www.benchmarkminerals.com/panasonic-reduces-teslas-cobalt-consumption-by-60-in-6-years/.

[46] K. Korosec, *Panasonic boosts energy density, trims cobalt in new 2170 battery cell for Tesla (accessed: 08/20/2020)*, 2020, https://tcrn.ch/3hOGGlv.

[47] M. S. Whittingham, The Role of Ternary Phases in Cathode Reactions, *Journal of The Electrochemical Society*, 1976, **123**, 315–320.

[48] M. S. Whittingham, Electrical Energy Storage and Intercalation Chemistry, *Science*, 1976, **192**, 1126–1127.

[49] K. Mizushima, P. Jones, P. Wiseman and J. Goodenough, Li_xCoO_2 ($0<x\leqslant1$): A new cathode material for batteries of high energy density, *Solid State Ionics*, 1981, **3-4**, 171–174.

[50] G. E. Blomgren, The Development and Future of Lithium Ion Batteries, *Journal of The Electrochemical Society*, 2017, **164**, 5019–5025.

[51] K. Wang, J. Wan, Y. Xiang, J. Zhu, Q. Leng, M. Wang, L. Xu and Y. Yang, Recent advances and historical developments of high voltage lithium cobalt oxide materials for rechargeable Li-ion batteries, *Journal of Power Sources*, 2020, **460**, 228062.

[52] BBC, *Top tech firms sued over DR Congo cobalt mining deaths (accessed: 08/26/2020)*, 2019, https://www.bbc.com/news/world-africa-50812616.

[53] G. X. Wang, S. Zhong, D. H. Bradhurst, S. X. Dou and H. K. Liu, Synthesis and characterization of $LiNiO_2$ compounds as cathodes for rechargeable lithium batteries, *Journal of Power Sources*, 1998, **76**, 141–146.

[54] M. S. Whittingham, Lithium Batteries and Cathode Materials, *Chemical Reviews*, 2004, **104**, 4271–4302.

[55] C. Julien, A. Mauger, A. Vijh and K. Zaghib, *Lithium Batteries*, Springer International Publishing, 1st edn., 2016, pp. 119–192.

[56] A. Manthiram, An Outlook on Lithium Ion Battery Technology, *ACS Central Science*, 2017, **3**, 1063–1069.

[57] W. Li, J. N. Reimers and J. R. D, In situ x-ray diffraction and electrochemical studies of $\mathrm{Li_{1-x}NiO_2}$, *Solid State Ionics*, 1993, **67**, 123–130.

[58] I. Nakai, K. Takahashi, Y. Shiraishi, T. Nakagome, F. Izumi, Y. Ishii, F. Nishikawa and T. Konishi, X-ray absorption fine structure and neutron diffraction analyses of de-intercalation behavior in the $\mathrm{LiCoO_2}$ and $\mathrm{LiNiO_2}$ systems, *Journal of Power Sources*, 1997, **68**, 536–539.

[59] P. Kalyani and N. Kalaiselvi, Various aspects of $\mathrm{LiNiO_2}$ chemistry: A review, *Science and Technology of Advanced Materials*, 2005, **6**, 689–703.

[60] A. Rougier, P. Gravereau and C. Delmas, Optimization of the Composition of the $\mathrm{Li_{1-z}Ni_{1+z}O_2}$ Electrode Materials: Structural, Magnetic, and Electrochemical Studies, *Journal of the Electrochemical Society*, 1996, **143**, 1168–1175.

[61] J. Reed, G. Ceder and A. V. D. Ven, Layered-to-Spinel Phase Transition in $\mathrm{Li_xMnO_2}$, *Electrochemical and Solid-State Letters*, 2001, **4**, A78–A81.

[62] P. He, H. Yu, D. Li and H. Zhou, Layered lithium transition metal oxide cathodes towards high energy lithium-ion batteries, *Journal of Materials Chemistry*, 2012, **22**, 3680–3695.

[63] N. Yabuuchi and T. Ohzuku, Novel lithium insertion material of $\mathrm{LiCo_{1/3}Ni_{1/3}Mn_{1/3}O_2}$ for advanced lithium-ion batteries, *Journal of Power Sources*, 2003, **119-121**, 171–174.

[64] J. Choi and A. Manthiram, Role of Chemical and Structural Stabilities on the Electrochemical Properties of Layered $\mathrm{LiNi_{1/3}Mn_{1/3}Co_{1/3}O_2}$ Cathodes, *Journal of The Electrochemical Society*, 2005, **152**, A1714.

[65] A. Manthiram, B. Song and W. Li, A perspective on nickel-rich layered oxide cathodes for lithium-ion batteries, *Energy Storage Materials*, 2017, **6**, 125–139.

[66] Y. Ding, D. Mu, B. Wu, R. Wang, Z. Zhao and F. Wu, Recent progresses on nickel-rich layered oxide positive electrode materials used in lithium-ion batteries for electric vehicles, *Applied Energy*, 2017, **195**, 586–599.

[67] W. Liu, P. Oh, X. Liu, M. J. Lee, W. Cho, S. Chae, Y. Kim and J. Cho, Nickel-Rich Layered Lithium Transition-Metal Oxide for High-Energy Lithium-Ion Batteries, *Angewandte Chemie - International Edition*, 2015, **54**, 4440–4457.

[68] S. T. Myung, F. Maglia, K. J. Park, C. S. Yoon, P. Lamp, S. J. Kim and Y. K. Sun, Nickel-Rich Layered Cathode Materials for Automotive Lithium-Ion Batteries: Achievements and Perspectives, *ACS Energy Letters*, 2017, **2**, 196–223.

[69] T. Ohzuku, T. Yanagawa, M. Kouguchi and A. Ueda, Innovative insertion material of $LiAl_{1/4}Ni_{3/4}O_2$ (R-m) for lithium-ion (shuttlecock) batteries, *Journal of Power Sources*, 1997, **68**, 131–134.

[70] J. S. Weaving, F. Coowar, D. A. Teagle, J. Cullen, V. Dass, P. Bindin, R. Green and W. J. Macklin, Development of high energy density Li-ion batteries based on $LiNi_{1-x-y}Co_xAl_yO_2$, *Journal of Power Sources*, 2001, **97-98**, 733–735.

[71] K. K. Lee, W. S. Yoon, K. B. Kim, K. Y. Lee and S. T. Hong, Characterization of $LiNi_{0.85}Co_{0.10}M_{0.05}O_2$ (M = Al, Fe) as a cathode material for lithium secondary batteries, *Journal of Power Sources*, 2001, **97-98**, 308–312.

[72] G. X. Wang, S. Bewlay, J. Yao, Y. Chen, Z. P. Guo, H. K. Liu and S. X. Dou, Multiple-ion-doped lithium nickel oxides as cathode materials for lithium-ion batteries, *Journal of Power Sources*, 2003, **119-121**, 189–194.

[73] R. Kostecki and F. McLarnon, Local-probe studies of degradation of composite $LiNi_{0.8}Co_{0.15}Al_{0.05}O_2$ cathodes in high-power lithium-ion cells, *Electrochemical and Solid-State Letters*, 2004, **7**, 380–383.

[74] S. Sallis, N. Pereira, P. Mukherjee, N. F. Quackenbush, N. Faenza, C. Schlueter, T. L. Lee, W. L. Yang, F. Cosandey, G. G. Amatucci and L. F. J. Piper, Surface degradation of $Li_{1-x}Ni_{0.80}Co_{0.15}Al_{0.05}O_2$ cathodes: Correlating charge transfer impedance with surface phase transformations, *Applied Physics Letters*, 2016, **108**, 2–6.

[75] S. Sallis, *Ph.D. thesis: Understanding the Intrinsic Electrochemistry of Ni-Rich Layered Cathodes*, State University of New York at Binghamton, 2017.

[76] M. D. Radin, S. Hy, M. Sina, C. Fang, H. Liu, J. Vinckeviciute, M. Zhang, M. S. Whittingham, Y. S. Meng and A. Van der Ven, Narrowing the Gap between Theoretical and Practical Capacities in Li-Ion Layered Oxide Cathode Materials, *Advanced Energy Materials*, 2017, **7**, 1–33.

[77] C. Delmas, C. Fouassier and P. Hagenmuller, Structural classification and properties of the layered oxides, *Physica B+C*, 1980, **99**, 81–85.

[78] L. Liang, C. Wu, X. Sun, X. Sun, L. Hou, J. Sun and C. Yuan, Sur-/Interface Engineering of Hierarchical $LiNi_{0.6}Mn_{0.2}Co_{0.2}O_2$@$LiCoPO_4$@Graphene Architectures as Promising High-Voltage Cathodes toward Advanced Li-Ion Batteries, *Advanced Materials Interfaces*, 2017, **4**, 1–12.

[79] M. Bianchini, M. Roca-Ayats, P. Hartmann, T. Brezesinski and J. Janek, There and Back Again—The Journey of $LiNiO_2$ as a Cathode Active Material, *Angewandte Chemie - International Edition*, 2019, **58**, 10434–10458.

[80] K.-J. Park, J.-Y. Hwang, H.-H. Ryu, F. Maglia, S.-J. Kim, P. Lamp, C. S. Yoon and Y.-K. Sun, Degradation Mechanism of Ni-Enriched NCA Cathode for Lithium Batteries: Are Microcracks Really Critical?, *ACS Energy Letters*, 2019, **4**, 1394–1400.

[81] S. S. Zhang, Problems and their origins of Ni-rich layered oxide cathode materials, *Energy Storage Materials*, 2020, **24**, 247–254.

[82] P. Teichert, G. G. Eshetu, H. Jahnke and E. Figgemeier, Degradation and Aging Routes of Ni-richCathode Based Li-Ion Batteries, *Batteries*, 2020, **6**, 1–26.

[83] X. Zeng, C. Zhan, J. Lu and K. Amine, Stabilization of a High-Capacity and High-Power Nickel-Based Cathode for Li-Ion Batteries, *Chem*, 2018, **4**, 690–704.

[84] X. Feng, M. Ouyang, X. Liu, L. Lu, Y. Xia and X. He, Thermal runaway mechanism of lithium ion battery for electric vehicles: A review, *Energy Storage Materials*, 2018, **10**, 246–267.

[85] X. Wu, K. Song, X. Zhang, N. Hu, L. Li, W. Li, L. Zhang and H. Zhang, Safety issues in lithium ion batteries: Materials and cell design, *Frontiers in Energy Research*, 2019, **7**, 1–17.

[86] S.-M. Bak, E. Hu, Y. Zhou, X. Yu, S. D. Senanayake, S.-J. Cho, K.-B. Kim, K. Y. Chung, X.-Q. Yang and K.-W. Nam, Structural Changes and Thermal Stability of Charged $\mathrm{LiNi_xMn_yCo_zO_2}$ Cathode Materials Studied by Combined In Situ Time-Resolved XRD and Mass Spectroscopy, *ACS Applied Materials & Interfaces*, 2014, **6**, 22594–22601.

[87] N. Y. Kim, T. Yim, J. H. Song, J.-S. Yu and Z. Lee, Microstructural study on degradation mechanism of layered $\mathrm{LiNi_{0.6}Co_{0.2}Mn_{0.2}O_2}$ cathode materials by analytical transmission electron microscopy, *Journal of Power Sources*, 2016, **307**, 641–648.

[88] M. Dixit, B. Markovsky, F. Schipper, D. Aurbach and D. T. Major, Origin of Structural Degradation during Cycling and Low Thermal Stability of Ni-Rich Layered Transition Metal-Based Electrode Materials, *Journal of Physical Chemistry C*, 2017, **121**, 22628–22636.

[89] H.-H. Ryu, K.-J. Park, C. S. Yoon and Y.-K. Sun, Capacity Fading of Ni-Rich $\mathrm{Li[Ni_xCo_yMn_{1-x-y}]O_2}$ $(0.6 \leq \mathrm{x} \leq 0.95)$ Cathodes for High-Energy-Density Lithium-Ion Batteries: Bulk or Surface Degradation?, *Chemistry of Materials*, 2018, **30**, 1155–1163.

[90] L. Wang, T. Maxisch and G. Ceder, A first-principles approach to studying the thermal stability of oxide cathode materials, *Chemistry of Materials*, 2007, **19**, 543–552.

[91] P. Kalyani and N. Kalaiselvi, Various aspects of $\mathrm{LiNiO_2}$ chemistry: A review, *Science and Technology of Advanced Materials*, 2005, **6**, 689–703.

[92] F. Kong, C. Liang, R. C. Longo, D.-H. Yeon, Y. Zheng, J.-H. Park, S.-G. Doo and K. Cho, Conflicting Roles of Anion Doping on the Electrochemical Performance of Li-Ion Battery Cathode Materials, *Chemistry of Materials*, 2016, **28**, 6942–6952.

[93] F. Schipper, M. Dixit, D. Kovacheva, M. Talianker, O. Haik, J. Grinblat, E. M. Erickson, C. Ghanty, D. T. Major, B. Markovsky and D. Aurbach, Stabilizing

nickel-rich layered cathode materials by a high-charge cation doping strategy: zirconium-doped $LiNi_{0.6}Co_{0.2}Mn_{0.2}O_2$, *Journal of Materials Chemistry A*, 2016, **4**, 16073–16084.

[94] G. Chen, J. An, Y. Meng, C. Yuan, B. Matthews, F. Dou, L. Shi, Y. Zhou, P. Song, G. Wu and D. Zhang, Cation and anion Co-doping synergy to improve structural stability of Li- and Mn-rich layered cathode materials for lithium-ion batteries, *Nano Energy*, 2019, **57**, 157–165.

[95] W. Cho, Y. J. Lim, S.-M. Lee, J. H. Kim, J.-H. Song, J.-S. Yu, Y.-J. Kim and M.-S. Park, Facile Mn Surface Doping of Ni-Rich Layered Cathode Materials for Lithium Ion Batteries, *ACS Applied Materials & Interfaces*, 2018, **10**, 38915–38921.

[96] X. Cheng, J. Zheng, J. Lu, Y. Li, P. Yan and Y. Zhang, Realizing superior cycling stability of Ni-Rich layered cathode by combination of grain boundary engineering and surface coating, *Nano Energy*, 2019, **62**, 30–37.

[97] L. Liang, W. Zhang, F. Zhao, D. K. Denis, F. uz Zaman, L. Hou and C. Yuan, Surface/Interface Structure Degradation of Ni-Rich Layered Oxide Cathodes toward Lithium-Ion Batteries: Fundamental Mechanisms and Remedying Strategies, *Advanced Materials Interfaces*, 2020, **7**, 1–34.

[98] S. M. Bak, K. W. Nam, W. Chang, X. Yu, E. Hu, S. Hwang, E. A. Stach, K. B. Kim, K. Y. Chung and X. Q. Yang, Correlating structural changes and gas evolution during the thermal decomposition of charged $Li_xNi_{0.8}Co_{0.15}Al_{0.05}O_2$ cathode materials, *Chemistry of Materials*, 2013, **25**, 337–351.

[99] S. Sharifi-Asl, J. Lu, K. Amine and R. Shahbazian-Yassar, Oxygen Release Degradation in Li-Ion Battery Cathode Materials: Mechanisms and Mitigating Approaches, *Advanced Energy Materials*, 2019, **9**, 1–19.

[100] F. Lin, I. M. Markus, D. Nordlund, T.-C. Weng, M. D. Asta, H. L. Xin and M. M. Doeff, Surface reconstruction and chemical evolution of stoichiometric layered cathode materials for lithium-ion batteries, *Nature Communications*, 2014, **5**, 3529.

[101] C. Tian, F. Lin and M. M. Doeff, Electrochemical Characteristics of Layered Transition Metal Oxide Cathode Materials for Lithium Ion Batteries: Surface, Bulk Behavior, and Thermal Properties, *Accounts of Chemical Research*, 2018, **51**, 89–96.

[102] C. Tian, Y. Xu, D. Nordlund, F. Lin, J. Liu, Z. Sun, Y. Liu and M. Doeff, Charge Heterogeneity and Surface Chemistry in Polycrystalline Cathode Materials, *Joule*, 2018, **2**, 464–477.

[103] H.-J. Noh, S. Youn, C. S. Yoon and Y.-K. Sun, Comparison of the structural and electrochemical properties of layered $Li[Ni_xCo_yMn_z]O_2$ (x = 1/3, 0.5, 0.6, 0.7, 0.8 and 0.85) cathode material for lithium-ion batteries, *Journal of Power Sources*, 2013, **233**, 121–130.

[104] E. Flores, N. Vonrüti, P. Novák, U. Aschauer and E. J. Berg, Elucidation of $Li_xNi_{0.8}Co_{0.15}Al_{0.05}O_2$ Redox Chemistry by Operando Raman Spectroscopy, *Chemistry of Materials*, 2018, **30**, 4694–4703.

[105] R. Jung, M. Metzger, F. Maglia, C. Stinner and H. A. Gasteiger, Oxygen Release and Its Effect on the Cycling Stability of $LiNi_xMn_yCo_zO_2$ (NMC) Cathode Materials for Li-Ion Batteries, *Journal of The Electrochemical Society*, 2017, **164**, A1361–A1377.

[106] S. S. Zhang, Insight into the Gassing Problem of Li-ion Battery, *Frontiers in Energy Research*, 2014, **2**, 2–5.

[107] D. Leanza, M. Mirolo, C. A. F. Vaz, P. Novák and M. El Kazzi, Surface Degradation and Chemical Electrolyte Oxidation Induced by the Oxygen Released from Layered Oxide Cathodes in Li−Ion Batteries, *Batteries & Supercaps*, 2019, **2**, 482–492.

[108] J. Wandt, A. T. Freiberg, A. Ogrodnik and H. A. Gasteiger, Singlet oxygen evolution from layered transition metal oxide cathode materials and its implications for lithium-ion batteries, *Materials Today*, 2018, **21**, 825–833.

[109] J. Yang and Y. Xia, Enhancement on the Cycling Stability of the Layered Ni-Rich Oxide Cathode by In-Situ Fabricating Nano-Thickness Cation-Mixing Layers, *Journal of The Electrochemical Society*, 2016, **163**, A2665–A2672.

[110] S.-K. Jung, H. Gwon, J. Hong, K.-Y. Park, D.-H. Seo, H. Kim, J. Hyun, W. Yang and K. Kang, Understanding the Degradation Mechanisms of $LiNi_{0.5}Co_{0.2}Mn_{0.3}O_2$ Cathode Material in Lithium Ion Batteries, *Advanced Energy Materials*, 2014, **4**, 1300787.

[111] H. Zhang, F. Omenya, M. S. Whittingham, C. Wang and G. Zhou, Formation of an Anti-Core-Shell Structure in Layered Oxide Cathodes for Li-Ion Batteries, *ACS Energy Letters*, 2017, **2**, 2598–2606.

[112] D. J. Miller, C. Proff, J. G. Wen, D. P. Abraham and J. Bareño, Observation of Microstructural Evolution in Li battery Cathode Oxide Particles by In Situ Electron Microscopy, *Advanced Energy Materials*, 2013, **3**, 1098–1103.

[113] A. Mukhopadhyay and B. W. Sheldon, Deformation and stress in electrode materials for Li-ion batteries, *Progress in Materials Science*, 2014, **63**, 58–116.

[114] J. Zhu and G. Chen, Single-crystal based studies for correlating the properties and high-voltage performance of $Li[Ni_xMn_yCo_{1-x-y}]O_2$ cathodes, *Journal of Materials Chemistry A*, 2019, **7**, 5463–5474.

[115] Y. Liu, J. Harlow and J. Dahn, Microstructural Observations of “Single Crystal” Positive Electrode Materials Before and After Long Term Cycling by Cross-section Scanning Electron Microscopy, *Journal of The Electrochemical Society*, 2020, **167**, 020512.

[116] X. Zeng, T. Jian, Y. Lu, L. Yang, W. Ma, Y. Yang, J. Zhu, C. Huang, S. Dai and X. Xi, Enhancing High-Temperature and High-Voltage Performances of

Single-Crystal $LiNi_{0.5}Co_{0.2}Mn_{0.3}O_2$ Cathodes through a $LiBO_2$/$LiAlO_2$ Dual-Modification Strategy, *ACS Sustainable Chemistry & Engineering*, 2020, **8**, 6293–6304.

[117] Y. Makimura, S. Zheng, Y. Ikuhara and Y. Ukyo, Microstructural Observation of $LiNi_{0.8}Co_{0.15}Al_{0.05}O_2$ after Charge and Discharge by Scanning Transmission Electron Microscopy, *Journal of The Electrochemical Society*, 2012, **159**, 1070–1073.

[118] J.-M. Lim, T. Hwang, D. Kim, M.-S. Park, K. Cho and M. Cho, Intrinsic Origins of Crack Generation in Ni-rich $LiNi_{0.8}Co_{0.1}Mn_{0.1}O_2$ Layered Oxide Cathode Material, *Scientific Reports*, 2017, **7**, 39669.

[119] H.-H. Sun and A. Manthiram, Impact of Microcrack Generation and Surface Degradation on a Nickel-Rich Layered $Li[Ni_{0.9}Co_{0.05}Mn_{0.05}]O_2$ Cathode for Lithium-Ion Batteries, *Chemistry of Materials*, 2017, **29**, 8486–8493.

[120] Y. Kojima, S. Muto, K. Tatsumi, H. Kondo, H. Oka, K. Horibuchi and Y. Ukyo, Degradation analysis of a Ni-based layered positive-electrode active material cycled at elevated temperatures studied by scanning transmission electron microscopy and electron energy-loss spectroscopy, *Journal of Power Sources*, 2011, **196**, 7721–7727.

[121] S. Watanabe, M. Kinoshita, T. Hosokawa, K. Morigaki and K. Nakura, Capacity fading of $LiAl_yNi_{1-x-y}Co_xO_2$ cathode for lithium-ion batteries during accelerated calendar and cycle life tests (effect of depth of discharge in charge–discharge cycling on the suppression of the micro-crack generation), *Journal of Power Sources*, 2014, **260**, 50–56.

[122] N. V. Faenza, Z. W. Lebens-Higgins, P. Mukherjee, S. Sallis, N. Pereira, F. Badway, A. Halajko, G. Ceder, F. Cosandey, L. F. Piper and G. G. Amatucci, Electrolyte-Induced Surface Transformation and Transition-Metal Dissolution of Fully Delithiated $LiNi_{0.8}Co_{0.15}Al_{0.05}O_2$, *Langmuir*, 2017, **33**, 9333–9353.

[123] S. Y. Park, W. J. Baek, S. Y. Lee, J. A. Seo, Y.-S. Kang, M. Koh and S. H. Kim, Probing electrical degradation of cathode materials for lithium-ion batteries with nanoscale resolution, *Nano Energy*, 2018, **49**, 1–6.

[124] R. Huang and Y. Ikuhara, STEM characterization for lithium-ion battery cathode materials, *Current Opinion in Solid State and Materials Science*, 2012, **16**, 31–38.

[125] L. Mu, R. Lin, R. Xu, L. Han, S. Xia, D. Sokaras, J. D. Steiner, T. C. Weng, D. Nordlund, M. M. Doeff, Y. Liu, K. Zhao, H. L. Xin and F. Lin, Oxygen Release Induced Chemomechanical Breakdown of Layered Cathode Materials, *Nano Letters*, 2018, **18**, 3241–3249.

[126] J. Christensen and J. Newman, Stress generation and fracture in lithium insertion materials, *Journal of Solid State Electrochemistry*, 2006, **10**, 293–319.

[127] Y. T. Cheng and M. W. Verbrugge, Evolution of stress within a spherical

insertion electrode particle under potentiostatic and galvanostatic operation, *Journal of Power Sources*, 2009, **190**, 453–460.

[128] W. H. Woodford, Y.-M. Chiang and W. C. Carter, "Electrochemical Shock" of Intercalation Electrodes: A Fracture Mechanics Analysis, *Journal of The Electrochemical Society*, 2010, **157**, A1052–A1059.

[129] J. Christensen, Modeling Diffusion-Induced Stress in Li-Ion Cells with Porous Electrodes, *Journal of The Electrochemical Society*, 2010, **157**, A366–A380.

[130] S.-G. Woo, J.-H. Kim, H.-R. Kim, W. Cho and J.-S. Yu, Failure mechanism analysis of $\mathrm{LiNi_{0.88}Co_{0.09}Mn_{0.03}O_2}$ cathodes in Li-ion full cells, *Journal of Electroanalytical Chemistry*, 2017, **799**, 315–320.

[131] P. Yan, J. Zheng, M. Gu, J. Xiao, J.-G. Zhang and C.-M. Wang, Intragranular cracking as a critical barrier for high-voltage usage of layer-structured cathode for lithium-ion batteries, *Nature Communications*, 2017, **8**, 14101.

[132] J. Zheng, P. Yan, J. Zhang, M. H. Engelhard, Z. Zhu, B. J. Polzin, S. Trask, J. Xiao, C. Wang and J. Zhang, Suppressed oxygen extraction and degradation of $\mathrm{LiNi_xMn_yCo_zO_2}$ cathodes at high charge cut-off voltages, *Nano Research*, 2017, **10**, 4221–4231.

[133] M. Lang, M. S. D. Darma, K. Kleiner, L. Riekehr, L. Mereacre, M. Ávila Pérez, V. Liebau and H. Ehrenberg, Post mortem analysis of fatigue mechanisms in $\mathrm{LiNi_{0.8}Co_{0.15}Al_{0.05}O_2}$ – $\mathrm{LiNi_{0.5}Co_{0.2}Mn_{0.3}O_2}$ – $\mathrm{LiMn_2O_4}$/graphite lithium ion batteries, *Journal of Power Sources*, 2016, **326**, 397–409.

[134] S. Xia, L. Mu, Z. Xu, J. Wang, C. Wei, L. Liu, P. Pianetta, K. Zhao, X. Yu, F. Lin and Y. Liu, Chemomechanical interplay of layered cathode materials undergoing fast charging in lithium batteries, *Nano Energy*, 2018, **53**, 753–762.

[135] C. S. Yoon, K.-J. Park, U.-H. Kim, K. H. Kang, H.-H. Ryu and Y.-K. Sun, High-Energy Ni-Rich $\mathrm{Li[Ni_xCo_yMn_{1-x-y}]O_2}$ Cathodes via Compositional Partitioning for Next-Generation Electric Vehicles, *Chemistry of Materials*, 2017, **29**, 10436–10445.

[136] H.-R. Kim, S.-G. Woo, J.-H. Kim, W. Cho and Y.-J. Kim, Capacity fading behavior of Ni-rich layered cathode materials in Li-ion full cells, *Journal of Electroanalytical Chemistry*, 2016, **782**, 168–173.

[137] H. Arai, S. Okada, H. Ohtsuka, M. Ichimura and J. Yamaki, Characterization and cathode performance of $\mathrm{Li_{1-x}Ni_{1+x}O_2}$ prepared with the excess lithium method, *Solid State Ionics*, 1995, **80**, 261–269.

[138] K. Matsumoto, R. Kuzuo, K. Takeya and A. Yamanaka, Effects of $\mathrm{CO_2}$ in air on Li deintercalation from $\mathrm{LiNi_{1-x-y}Co_xAl_yO_2}$, *Journal of Power Sources*, 1999, **81-82**, 558–561.

[139] D.-H. Cho, C.-H. Jo, W. Cho, Y.-J. Kim, H. Yashiro, Y.-K. Sun and S.-T. Myung, Effect of Residual Lithium Compounds on Layer Ni-Rich $\mathrm{Li[Ni_{0.7}Mn_{0.3}]O_2}$, *Journal of The Electrochemical Society*, 2014, **161**, A920–A926.

[140] C.-H. Jo, D.-H. Cho, H.-J. Noh, H. Yashiro, Y.-K. Sun and S.-T. Myung, An effective method to reduce residual lithium compounds on Ni-rich $Li[Ni_{0.6}Co_{0.2}Mn_{0.2}]O_2$ active material using a phosphoric acid derived Li_3PO_4 nanolayer, *Nano Research*, 2015, **8**, 1464–1479.

[141] P. Oh, B. Song, W. Li and A. Manthiram, Overcoming the chemical instability on exposure to air of Ni-rich layered oxide cathodes by coating with spinel $LiMn_{1.9}Al_{0.1}O_4$, *Journal of Materials Chemistry A*, 2016, **4**, 5839–5841.

[142] R. Jung, R. Morasch, P. Karayaylali, K. Phillips, F. Maglia, C. Stinner, Y. Shao-Horn and H. A. Gasteiger, Effect of Ambient Storage on the Degradation of Ni-Rich Positive Electrode Materials (NMC811) for Li-Ion Batteries, *Journal of The Electrochemical Society*, 2018, **165**, A132–A141.

[143] J. Sicklinger, M. Metzger, H. Beyer, D. Pritzl and H. A. Gasteiger, Ambient Storage Derived Surface Contamination of NCM811 and NCM111: Performance Implications and Mitigation Strategies, *Journal of The Electrochemical Society*, 2019, **166**, A2322–A2335.

[144] Frost & Sullivan, *Solid-state Electrolytes - Next-generation Safer Alternative in Li-ion Batteries (accessed: 10/13/2020)*, 2017, https://ww2.frost.com/frost-perspectives/solid-state-electrolytes-next-generation-safer-alternative-li-ion-batteries/.

[145] T. Inoue and K. Mukai, Are All-Solid-State Lithium-Ion Batteries Really Safe? - Verification by Differential Scanning Calorimetry with an All-Inclusive Microcell, *ACS Applied Materials & Interfaces*, 2017, **9**, 1507–1515.

[146] V. Thangadurai and W. Weppner, Recent progress in solid oxide and lithium ion conducting electrolytes research, *Ionics*, 2006, **12**, 81–92.

[147] J. W. Fergus, Ceramic and polymeric solid electrolytes for lithium-ion batteries, *Journal of Power Sources*, 2010, **195**, 4554–4569.

[148] N. Boaretto, L. Meabe, M. Martinez-Ibañez, M. Armand and H. Zhang, Review—Polymer Electrolytes for Rechargeable Batteries: From Nanocomposite to Nanohybrid, *Journal of The Electrochemical Society*, 2020, **167**, 070524.

[149] C. Cao, Z.-B. Li, X.-L. Wang, X.-B. Zhao and W.-Q. Han, Recent Advances in Inorganic Solid Electrolytes for Lithium Batteries, *Frontiers in Energy Research*, 2014, **2**, 1–10.

[150] K. Murata, S. Izuchi and Y. Yoshihisa, An overview of the research and development of solid polymer electrolyte batteries, *Electrochimica Acta*, 2000, **45**, 1501–1508.

[151] S. S. Lee, Y. J. Lim, H. W. Kim, J.-K. Kim, Y.-G. Jung and Y. Kim, Electrochemical properties of a ceramic-polymer-composite-solid electrolyte for Li-ion batteries, *Solid State Ionics*, 2016, **284**, 20–24.

[152] J. Evans, C. A. Vincent and P. G. Bruce, Electrochemical measurement of transference numbers in polymer electrolytes, *Polymer*, 1987, **28**, 2324–2328.

[153] K. Pożyczka, M. Marzantowicz, J. Dygas and F. Krok, Ionic Conductivity and Lithium Transference Number of Poly(etyhlene oxide):LiTFSI System, *Electrochimica Acta*, 2017, **227**, 127–135.

[154] S. Kalnaus, W. E. Tenhaeff, J. Sakamoto, A. S. Sabau, C. Daniel and N. J. Dudney, Analysis of composite electrolytes with sintered reinforcement structure for energy storage applications, *Journal of Power Sources*, 2013, **241**, 178–185.

[155] P. Knauth, Inorganic solid Li ion conductors: An overview, *Solid State Ionics*, 2009, **180**, 911–916.

[156] L. Chen, Y. Li, S.-P. Li, L.-Z. Fan, C.-W. Nan and J. B. Goodenough, PEO/garnet composite electrolytes for solid-state lithium batteries: From "ceramic-in-polymer" to "polymer-in-ceramic", *Nano Energy*, 2018, **46**, 176–184.

[157] I. Jayasekara, M. Poyner and D. Teeters, Investigation of a nanoconfined, ceramic composite, solid polymer electrolyte, *Electrochimica Acta*, 2017, **247**, 1147–1154.

[158] J. Syzdek, M. Armand, M. Gizowska, M. Marcinek, E. Sasim, M. Szafran and W. Wieczorek, Ceramic-in-polymer versus polymer-in-ceramic polymeric electrolytes—A novel approach, *Journal of Power Sources*, 2009, **194**, 66–72.

[159] N. Shubha, R. Prasanth, H. H. Hng and M. Srinivasan, Study on effect of poly (ethylene oxide) addition and in-situ porosity generation on poly (vinylidene fluoride)-glass ceramic composite membranes for lithium polymer batteries, *Journal of Power Sources*, 2014, **267**, 48–57.

[160] J. Zhang, N. Zhao, M. Zhang, Y. Li, P. K. Chu, X. Guo, Z. Di, X. Wang and H. Li, Flexible and ion-conducting membrane electrolytes for solid-state lithium batteries: Dispersion of garnet nanoparticles in insulating polyethylene oxide, *Nano Energy*, 2016, **28**, 447–454.

[161] M. Keller, G. B. Appetecchi, G.-T. Kim, V. Sharova, M. Schneider, J. Schuhmacher, A. Roters and S. Passerini, Electrochemical performance of a solvent-free hybrid ceramic-polymer electrolyte based on $Li_7La_3Zr_2O_{12}$ in $P(EO)_{15}LiTFSI$, *Journal of Power Sources*, 2017, **353**, 287–297.

[162] G. Appetecchi, F. Croce, L. Persi, F. Ronci and B. Scrosati, Transport and interfacial properties of composite polymer electrolytes, *Electrochimica Acta*, 2000, **45**, 1481–1490.

[163] N. Miyake, J. S. Wainright and R. F. Savinell, Evaluation of a Sol-Gel Derived Nafion/Silica Hybrid Membrane for Polymer Electrolyte Membrane Fuel Cell Applications: II. Methanol Uptake and Methanol Permeability, *Journal of The Electrochemical Society*, 2001, **148**, A905.

[164] B. Kumar, Polymer–ceramic composite protonic conductors, *Journal of Power Sources*, 2003, **123**, 132–136.

[165] L. Long, S. Wang, M. Xiao and Y. Meng, Polymer electrolytes for lithium polymer batteries, *Journal of Materials Chemistry A*, 2016, **4**, 10038–10039.

[166] D. Zhou, D. Shanmukaraj, A. Tkacheva, M. Armand and G. Wang, Polymer Electrolytes for Lithium-Based Batteries: Advances and Prospects, *Chem*, 2019, **5**, 2326–2352.

[167] P. Yao, H. Yu, Z. Ding, Y. Liu, J. Lu, M. Lavorgna, J. Wu and X. Liu, Review on Polymer-Based Composite Electrolytes for Lithium Batteries, *Frontiers in Chemistry*, 2019, **7**, 1–17.

[168] G. Homann, L. Stolz, J. Nair, I. C. Laskovic, M. Winter and J. Kasnatscheew, Poly(Ethylene Oxide)-based Electrolyte for Solid-State-Lithium-Batteries with High Voltage Positive Electrodes: Evaluating the Role of Electrolyte Oxidation in Rapid Cell Failure, *Scientific Reports*, 2020, **10**, 2–10.

[169] M. B. Armand, J. M. Chabagno and M. Duclot, *"Poly-ethers as solid electrolytes." in Fast ion Transport in Solids. Electrodes and Electrolytes*, North Holland Publishers, Amsterdam, 1979.

[170] M. Armand and M. Duclot, Ionically and pref. electronically conductive electrode - comprising agglomerate of active electrode material and solid soln. of ionic cpd. in polymer pref. polyoxyalkylene, *FR Patent No.: FR2442514A1*, 1978.

[171] M. Armand, The history of polymer electrolytes, *Solid State Ionics*, 1994, **69**, 309–319.

[172] D. Baril, C. Michot and M. Armand, Electrochemistry of liquids vs. solids: Polymer electrolytes, *Solid State Ionics*, 1997, **94**, 35–47.

[173] D. Devaux, D. Glé, T. N. Phan, D. Gigmes, E. Giroud, M. Deschamps, R. Denoyel and R. Bouchet, Optimization of Block Copolymer Electrolytes for Lithium Metal Batteries, *Chemistry of Materials*, 2015, **27**, 4682–4692.

[174] M. Watanabe, K. Sanui, N. Ogata, T. Kobayashi and Z. Ohtaki, Ionic conductivity and mobility in network polymers from poly(propylene oxide) containing lithium perchlorate, *Journal of Applied Physics*, 1985, **57**, 123–128.

[175] M. Kakihana, S. Schantz and L. M. Torell, Raman spectroscopic study of ion-ion interaction and its temperature dependence in a poly(propylene-oxide)-based $NaCF_3SO_3$-polymer electrolyte, *The Journal of Chemical Physics*, 1990, **92**, 6271–6277.

[176] M. Singh, O. Odusanya, G. M. Wilmes, H. B. Eitouni, E. D. Gomez, A. J. Patel, V. L. Chen, M. J. Park, P. Fragouli, H. Iatrou, N. Hadjichristidis, D. Cookson and N. P. Balsara, Effect of Molecular Weight on the Mechanical and Electrical Properties of Block Copolymer Electrolytes, *Macromolecules*, 2007, **40**, 4578–4585.

[177] M. Dollé, L. Sannier, B. Beaudoin, M. Trentin and J. M. Tarascon, Live scanning electron microscope observations of dendritic growth in lithium/polymer cells, *Electrochemical and Solid-State Letters*, 2002, **5**, 286–289.

[178] M. Rosso, C. Brissot, A. Teyssot, M. Dollé, L. Sannier, J. M. Tarascon, R. Bouchet and S. Lascaud, Dendrite short-circuit and fuse effect on Li/polymer/Li cells, *Electrochimica Acta*, 2006, **51**, 5334–5340.

[179] F. M. Gray, J. R. MacCallum, C. A. Vincent and J. R. M. Giles, Novel polymer electrolytes based on ABA block copolymers, *Macromolecules*, 1988, **21**, 392–397.

[180] I. Khan, D. Fish, Y. Delaviz and J. Smid, ABA triblock comb copolymers with oligo(oxyethylene) side chains as matrix for ion transport, *Die Makromolekulare Chemie*, 1989, **190**, 1069–1078.

[181] J. Li and I. Khan, Mixed (electronic and ionic) conductive solid polymer matrix, 1. Synthesis and properties of poly(2,5,8,11,14,17,20,23-octaoxapentacosyl methacrylate)-block-poly(4-vinylpyridine), *Die Makromolekulare Chemie*, 1991, **192**, 3043–3050.

[182] H. Kosonen, S. Valkama, J. Hartikainen, H. Eerikäinen, M. Torkkeli, K. Jokela, R. Serimaa, F. Sundholm, G. Ten Brinke and O. Ikkala, Mesomorphic structure of poly(styrene)-block-poly(4-vinylpyridine) with oligo(ethylene oxide)sulfonic acid side chains as a model for molecularly reinforced polymer electrolyte, *Macromolecules*, 2002, **35**, 10149–10154.

[183] W. S. Young, W. F. Kuan and T. H. Epps, Block copolymer electrolytes for rechargeable lithium batteries, *Journal of Polymer Science, Part B: Polymer Physics*, 2014, **52**, 1–16.

[184] B. Hsieh, H. B. Eitouni and M. Singh, Polymer Electrolyte Materials Based on Block Copolymers, *US Patent No.: US8691928B2*, 2014.

[185] B. Hsieh, H. B. Eitouni and M. Singh, Electrochemical Devices Based on Block Copolymers, *US Patent No.: US8916670B1*, 2014.

[186] S.-L. Wu, A. E. Javier, D. Devaux, N. P. Balsara and V. Srinivasan, Discharge Characteristics of Lithium Battery Electrodes with a Semiconducting Polymer Studied by Continuum Modeling and Experiment, *Journal of The Electrochemical Society*, 2014, **161**, A1836–A1843.

[187] A. Panday, S. Mullin, E. D. Gomez, N. Wanakule, V. L. Chen, A. Hexemer, J. Pople and N. P. Balsara, Effect of molecular weight and salt concentration on conductivity of block copolymer electrolytes, *Macromolecules*, 2009, **42**, 4632–4637.

[188] A. E. Javier, S. N. Patel, D. T. Hallinan, V. Srinivasan and N. P. Balsara, Simultaneous electronic and ionic conduction in a block copolymer: Application in lithium battery electrodes, *Angewandte Chemie - International Edition*, 2011, **50**, 9848–9851.

[189] T. N. Phan, S. Issa and D. Gigmes, Poly(ethylene oxide)-based block copolymer electrolytes for lithium metal batteries, *Polymer International*, 2019, **68**, 7–13.

[190] L. Leibler, Theory of Microphase Separation in Block Copolymers, *Macromolecules*, 1980, **13**, 1602–1617.

[191] Q. Hu, *Ph.D. thesis: Electrode-Electrolyte Interfaces in Solid Polymer Lithium Batteries*, Harvard University, 2012.

[192] P. G. Bruce, *Solid State Electrochemistry*, Cambridge University Press, Cambridge, 1st edn., 1994, pp. 119–162.

[193] M. A. Ratner, P. Johansson and D. F. Shriver, Polymer electrolytes: Ionic transport mechanisms and relaxation coupling, *MRS Bulletin*, 2000, **25**, 31–37.

[194] Y. J. Lee, Y. K. Jo, H. Park, H. H. Chun and N. J. Jo, Solvent Effect on Ion Hopping of Solid Polymer Electrolyte, *Materials Science Forum*, 2007, **544-545**, 1049–1052.

[195] E. Quartarone and P. Mustarelli, Electrolytes for solid-state lithium rechargeable batteries: Recent advances and perspectives, *Chemical Society Reviews*, 2011, **40**, 2525–2540.

[196] U. Grape, *U.S. Department of Energy Final Technical Report: Recovery Act - Solid State Batteries for Grid-Scale Energy Storage*, 2015.

[197] U. Grape, *U.S. Department of Energy Final Technical Report: High-Voltage Solid Polymer Batteries for Electric Drive Vehicles*, 2015.

[198] J. Liang, Y. Sun, Y. Zhao, Q. Sun, J. Luo, F. Zhao, X. Lin, X. Li, R. Li, L. Zhang, S. Lu, H. Huang and X. Sun, Engineering the conductive carbon/PEO interface to stabilize solid polymer electrolytes for all-solid-state high voltage $LiCoO_2$ batteries, *Journal of Materials Chemistry A*, 2020, **8**, 2769–2776.

[199] K. Nie, X. Wang, J. Qiu, Y. Wang, Q. Yang, J. Xu, X. Yu, H. Li, X. Huang and L. Chen, Increasing Poly(ethylene oxide) Stability to 4.5 V by Surface Coating of the Cathode, *ACS Energy Letters*, 2020, **5**, 826–832.

[200] M. Armand, Polymer solid electrolytes - an overview, *Solid State Ionics*, 1983, **9-10**, 745–754.

[201] R. Bouchet, S. Maria, R. Meziane, A. Aboulaich, L. Lienafa, J. P. Bonnet, T. N. Phan, D. Bertin, D. Gigmes, D. Devaux, R. Denoyel and M. Armand, Single-ion BAB triblock copolymers as highly efficient electrolytes for lithium-metal batteries, *Nature Materials*, 2013, **12**, 452–457.

[202] A. M. Stephan, Review on gel polymer electrolytes for lithium batteries, *European Polymer Journal*, 2006, **42**, 21–42.

[203] X. Yang, Q. Sun, C. Zhao, X. Gao, K. R. Adair, Y. Liu, J. Luo, X. Lin, J. Liang, H. Huang, L. Zhang, R. Yang, S. Lu, R. Li and X. Sun, High-areal-capacity all-solid-state lithium batteries enabled by rational design of fast ion transport channels in vertically-aligned composite polymer electrodes, *Nano Energy*, 2019, **61**, 567–575.

[204] K. Fu, Y. Gong, J. Dai, A. Gong, X. Han, Y. Yao, C. Wang, Y. Wang, Y. Chen, C. Yan, Y. Li, E. D. Wachsman and L. Hu, Flexible, solid-state, ion-conducting

membrane with 3D garnet nanofiber networks for lithium batteries, *Proceedings of the National Academy of Sciences of the United States of America*, 2016, **113**, 7094–7099.

[205] X. Wang, Y. Zhang, X. Zhang, T. Liu, Y. H. Lin, L. Li, Y. Shen and C. W. Nan, Lithium-Salt-Rich PEO/$Li_{0.3}La_{0.557}TiO_3$ Interpenetrating Composite Electrolyte with Three-Dimensional Ceramic Nano-Backbone for All-Solid-State Lithium-Ion Batteries, *ACS Applied Materials & Interfaces*, 2018, **10**, 24791–24798.

[206] F. Croce, F. Serraino Fiory, L. Persi and B. Scrosati, A high-rate, long-life, lithium nanocomposite polymer electrolyte battery, *Electrochemical and Solid-State Letters*, 2001, **4**, 121–123.

[207] J. Ma, Z. Liu, B. Chen, L. Wang, L. Yue, H. Liu, J. Zhang, Z. Liu and G. Cui, A Strategy to Make High Voltage $LiCoO_2$ Compatible with Polyethylene Oxide Electrolyte in All-Solid-State Lithium Ion Batteries, *Journal of The Electrochemical Society*, 2017, **164**, A3454–A3461.

[208] S. Seki, Y. Kobayashi, H. Miyashiro, Y. Mita and T. Iwahori, Fabrication of high-voltage, high-capacity all-solid-state lithium polymer secondary batteries by application of the polymer electrolyte/inorganic electrolyte composite concept, *Chemistry of Materials*, 2005, **17**, 2041–2045.

[209] S. Seki, Y. Kobayashi, H. Miyashiro, A. Yamanaka, Y. Mita and T. Iwahori, Degradation mechanism analysis of all-solid-state lithium polymer secondary batteries by using the impedance measurement, *Journal of Power Sources*, 2005, **146**, 741–744.

[210] C. Fu, S. Lou, X. Xu, C. Cui, C. Li, P. Zuo, Y. Ma, G. Yin and Y. Gao, Capacity degradation mechanism and improvement actions for 4 V-class all-solid-state lithium-metal polymer batteries, *Chemical Engineering Journal*, 2020, **392**, 123665.

[211] Y. Xia, T. Fujieda, K. Tatsumi, P. P. Prosini and T. Sakai, Thermal and electrochemical stability of cathode materials in solid polymer electrolyte, *Journal of Power Sources*, 2001, **92**, 234–243.

[212] F. Croce, G. B. Appetecchi, L. Persi and B. Scrosati, Nanocomposite polymer electrolytes for lithium batteries, *Nature*, 1998, **394**, 456–458.

[213] Y. C. Jung, M. S. Park, C. H. Doh and D. W. Kim, Organic-inorganic hybrid solid electrolytes for solid-state lithium cells operating at room temperature, *Electrochimica Acta*, 2016, **218**, 271–277.

[214] D. Lin, W. Liu, Y. Liu, H. R. Lee, P. C. Hsu, K. Liu and Y. Cui, High Ionic Conductivity of Composite Solid Polymer Electrolyte via in Situ Synthesis of Monodispersed SiO_2 Nanospheres in Poly(ethylene oxide), *Nano Letters*, 2016, **16**, 459–465.

[215] Y. Zheng, Y. Yao, J. Ou, M. Li, D. Luo, H. Dou, Z. Li, K. Amine, A. Yu and

Z. Chen, A review of composite solid-state electrolytes for lithium batteries: fundamentals, key materials and advanced structures, *Chemical Society Reviews*, 2020, **49**, 8790–8839.

[216] M. Dirican, C. Yan, P. Zhu and X. Zhang, Composite solid electrolytes for all-solid-state lithium batteries, *Materials Science and Engineering R*, 2019, **136**, 27–46.

[217] Y. Zhao, K. Zheng and X. Sun, Addressing Interfacial Issues in Liquid-Based and Solid-State Batteries by Atomic and Molecular Layer Deposition, *Joule*, 2018, **2**, 2583–2604.

[218] J. Lopez, D. G. Mackanic, Y. Cui and Z. Bao, Designing polymers for advanced battery chemistries, *Nature Reviews Materials*, 2019, **4**, 312–330.

[219] C. Polo Fonseca and S. Neves, Electrochemical properties of a biodegradable polymer electrolyte applied to a rechargeable lithium battery, *Journal of Power Sources*, 2006, **159**, 712–716.

[220] C. P. Fonseca, D. S. Rosa, F. Gaboardi and S. Neves, Development of a biodegradable polymer electrolyte for rechargeable batteries, *Journal of Power Sources*, 2006, **155**, 381–384.

[221] D. Zhang, L. Zhang, K. Yang, H. Wang, C. Yu, D. Xu, B. Xu and L.-M. Wang, Superior Blends Solid Polymer Electrolyte with Integrated Hierarchical Architectures for All-Solid-State Lithium-Ion Batteries, *ACS Applied Materials & Interfaces*, 2017, **9**, 36886–36896.

[222] C. Zuo, G. Chen, Y. Zhang, H. Gan, S. Li, L. Yu, X. Zhou, X. Xie and Z. Xue, Poly(ϵ-caprolactone)-block-poly(ethylene glycol)-block-poly(ϵ-caprolactone)-based hybrid polymer electrolyte for lithium metal batteries, *Journal of Membrane Science*, 2020, **607**, 118132.

[223] A. Bergfelt, M. J. Lacey, J. Hedman, C. Sångeland, D. Brandell and T. Bowden, ϵ-Caprolactone-based solid polymer electrolytes for lithium-ion batteries: synthesis, electrochemical characterization and mechanical stabilization by block copolymerization, *RSC Advances*, 2018, **8**, 16716–16725.

[224] P.-M. Jalbert, B. Commarieu, J.-C. Daigle, J. P. Claverie and K. Zaghib, A 3D Network Based on Poly(ϵ -caprolactone) Macromonomers as Polymer Electrolyte for Solid State Lithium Metal Batteries, *Journal of The Electrochemical Society*, 2020, **167**, 080527.

[225] Q. Yang, J. Huang, Y. Li, Y. Wang, J. Qiu, J. Zhang, H. Yu, X. Yu, H. Li and L. Chen, Surface-protected $LiCoO_2$ with ultrathin solid oxide electrolyte film for high-voltage lithium ion batteries and lithium polymer batteries, *Journal of Power Sources*, 2018, **388**, 65–70.

[226] H. Zhang, J. Zhang, J. Ma, G. Xu, T. Dong and G. Cui, Polymer Electrolytes for High Energy Density Ternary Cathode Material-Based Lithium Batteries, *Electrochemical Energy Reviews*, 2019, **2**, 128–148.

[227] Y. Wang, B.-N. Liu, G. Zhou, K.-H. Nie, J.-N. Zhang, X.-Q. Yu and H. Li, Improved electrochemical performance of $Li(Ni_{0.6}Co_{0.2}Mn_{0.2})O_2$ at high charging cut-off voltage with $Li_{1.4}Al_{0.4}Ti_{1.6}(PO_4)_3$ surface coating, *Chinese Physics B*, 2019, **28**, 068202.

[228] Y. Zhu, J. Cao, H. Chen, Q. Yu and B. Li, High electrochemical stability of a 3D cross-linked network PEO@nano-SiO_2 composite polymer electrolyte for lithium metal batteries, *Journal of Materials Chemistry A*, 2019, **7**, 6832–6839.

[229] M. J. Kalita, *Ph.D. thesis: Solid polymeric electrolytes of increased cation transference number*, Warsaw University of Technology, 2008.

[230] H. Zhang, C. Liu, L. Zheng, F. Xu, W. Feng, H. Li, X. Huang, M. Armand, J. Nie and Z. Zhou, Lithium bis(fluorosulfonyl)imide/poly(ethylene oxide) polymer electrolyte, *Electrochimica Acta*, 2014, **133**, 529–538.

[231] M. Nakayama, S. Wada, S. Kuroki and M. Nogami, Factors affecting cyclic durability of all-solid-state lithium polymer batteries using poly(ethylene oxide)-based solid polymer electrolytes, *Energy and Environmental Science*, 2010, **3**, 1995–2002.

[232] R. Amin, D. B. Ravnsbæk and Y.-M. Chiang, Characterization of Electronic and Ionic Transport in $Li_{1-x}Ni_{0.8}Co_{0.15}Al_{0.05}O_2$ (NCA), *Journal of The Electrochemical Society*, 2015, **162**, A1163–A1169.

[233] X. Yu, Q. Wang, Y. Zhou, H. Li, X. Q. Yang, K. W. Nam, S. N. Ehrlich, S. Khalid and Y. S. Meng, High rate delithiation behaviour of $LiFePO_4$ studied by quick X-ray absorption spectroscopy, *Chemical Communications*, 2012, **48**, 11537–11539.

[234] I. Belharouak, W. Lu, J. Liu, D. Vissers and K. Amine, Thermal behavior of delithiated $Li(Ni_{0.8}Co_{0.15}Al_{0.05})O_2$ and $Li_{1.1}(Ni_{1/3}Co_{1/3}Mn_{1/3})_{0.9}O_2$ powders, *Journal of Power Sources*, 2007, **174**, 905–909.

[235] H. Arai, M. Tsuda, K. Saito, M. Hayashi and Y. Sakurai, Thermal Reactions Between Delithiated Lithium Nickelate and Electrolyte Solutions, *Journal of The Electrochemical Society*, 2002, **149**, A401.

[236] Y. Takahashi, N. Kijima, K. Dokko, M. Nishizawa, I. Uchida and J. Akimoto, Structure and electron density analysis of electrochemically and chemically delithiated $LiCoO_2$ single crystals, *Journal of Solid State Chemistry*, 2007, **180**, 313–321.

[237] S.-T. Myung, K.-S. Lee, C. S. Yoon, Y.-K. Sun, K. Amine and H. Yashiro, Effect of AlF_3 Coating on Thermal Behavior of Chemically Delithiated $Li_{0.35}[Ni_{1/3}Co_{1/3}Mn_{1/3}]O_2$, *The Journal of Physical Chemistry C*, 2010, **114**, 4710–4718.

[238] K. Saravanan, A. Jarry, R. Kostecki and G. Chen, A study of room-temperature $Li_xMn_{1.5}Ni_{0.5}O_4$ solid solutions, *Scientific Reports*, 2015, **5**, 8027.

[239] S.-L. Wu, A. E. Javier, D. Devaux, N. P. Balsara and V. Srinivasan, Discharge

Characteristics of Lithium Battery Electrodes with a Semiconducting Polymer Studied by Continuum Modeling and Experiment, *Journal of the Electrochemical Society*, 2014, **161**, A1836–A1843.

[240] R. Nölle, K. Beltrop, F. Holtstiege, J. Kasnatscheew, T. Placke and M. Winter, A reality check and tutorial on electrochemical characterization of battery cell materials: How to choose the appropriate cell setup, *Materials Today*, 2020, **32**, 131–146.

[241] F. Lin, Y. Liu, X. Yu, L. Cheng, A. Singer, O. G. Shpyrko, H. L. Xin, N. Tamura, C. Tian, T. C. Weng, X. Q. Yang, Y. S. Meng, D. Nordlund, W. Yang and M. M. Doeff, Synchrotron X-ray Analytical Techniques for Studying Materials Electrochemistry in Rechargeable Batteries, *Chemical Reviews*, 2017, **117**, 13123–13186.

[242] D. Asakura, E. Hosono, Y. Nanba, H. Zhou, J. Okabayashi, C. Ban, P.-A. Glans, J. Guo, T. Mizokawa, G. Chen, A. J. Achkar, D. G. Hawthron, T. Z. Regier and H. Wadati, Material/element-dependent fluorescence-yield modes on soft X-ray absorption spectroscopy of cathode materials for Li-ion batteries, *AIP Advances*, 2016, **6**, 035105.

[243] F. Lin, D. Nordlund, I. M. Markus, T. C. Weng, H. L. Xin and M. M. Doeff, Profiling the nanoscale gradient in stoichiometric layered cathode particles for lithium-ion batteries, *Energy and Environmental Science*, 2014, **7**, 3077–3085.

[244] C. Wei, Y. Zhang, S.-J. Lee, L. Mu, J. Liu, C. Wang, Y. Yang, M. Doeff, P. Pianetta, D. Nordlund, X. Du, Y.-C. Tian, K. Zhao, J.-S. Lee, F. Lin and Y. Liu, Thermally driven mesoscale chemomechanical interplay in $Li_{0.5}Ni_{0.6}Mn_{0.2}Co_{0.2}O_2$ cathode materials, *Journal of Materials Chemistry A*, 2018, **6**, 23055–23061.

[245] J. V. Elp, B. G. Searle and Z. H. Zbou, Electronic structure and symmetry in nickel L-edge X-ray absorption spectroscopy: Application to a nickel protein, *Journal of American Chemical Society*, 1994, **116**, 1918–1923.

[246] W.-S. Yoon, O. Haas, S. Muhammad, H. Kim, W. Lee, D. Kim, D. A. Fischer, C. Jaye, X.-Q. Yang, M. Balasubramanian and K.-W. Nam, In situ soft XAS study on nickel-based layered cathode material at elevated temperatures: A novel approach to study thermal stability, *Scientific Reports*, 2015, **4**, 6827.

[247] S. Kuppan, H. Duncan and G. Chen, Controlling side reactions and self-discharge in high-voltage spinel cathodes: the critical role of surface crystallographic facets, *Physical Chemistry Chemical Physics*, 2015, **17**, 26471–26481.

[248] M. L. Baker, M. W. Mara, J. J. Yan, K. O. Hodgson, B. Hedman and E. I. Solomon, K- and L-edge X-ray absorption spectroscopy (XAS) and resonant inelastic X-ray scattering (RIXS) determination of differential orbital covalency (DOC) of transition metal sites, *Coordination Chemistry Reviews*, 2017, **345**, 182–208.

[249] M. G. Kim and C. H. Yo, X-ray Absorption Spectroscopic Study of Chemically

and Electrochemically Li Ion Extracted $Li_yCo_{0.85}Al_{0.15}O_2$ Compounds, *The Journal of Physical Chemistry B*, 1999, **103**, 6457–6465.

[250] K.-W. Nam, S.-M. Bak, E. Hu, X. Yu, Y. Zhou, X. Wang, L. Wu, Y. Zhu, K.-Y. Chung and X.-Q. Yang, Combining In Situ Synchrotron X-Ray Diffraction and Absorption Techniques with Transmission Electron Microscopy to Study the Origin of Thermal Instability in Overcharged Cathode Materials for Lithium-Ion Batteries, *Advanced Functional Materials*, 2013, **23**, 1047–1063.

[251] R. E. Ruther, H. Zhou, C. Dhital, K. Saravanan, A. K. Kercher, G. Chen, A. Huq, F. M. Delnick and J. Nanda, Synthesis, Structure, and Electrochemical Performance of High Capacity $Li_2Cu_{0.5}Ni_{0.5}O_2$ Cathodes, *Chemistry of Materials*, 2015, **27**, 6746–6754.

[252] Z. Gong and Y. Yang, The application of synchrotron X-ray techniques to the study of rechargeable batteries, *Journal of Energy Chemistry*, 2018, **27**, 1566–1583.

[253] W.-S. Yoon, M. Balasubramanian, K. Y. Chung, X.-Q. Yang, J. McBreen, C. P. Grey and D. A. Fischer, Investigation of the Charge Compensation Mechanism on the Electrochemically Li-Ion Deintercalated $Li_{1-x}Co_{1/3}Ni_{1/3}Mn_{1/3}O_2$ Electrode System by Combination of Soft and Hard X-ray Absorption Spectroscopy, *Journal of the American Chemical Society*, 2005, **127**, 17479–17487.

[254] C. Rumble, T. E. Conry, M. Doeff, E. J. Cairns, J. E. Penner-Hahn and A. Deb, Structural and Electrochemical Investigation of $Li(Ni_{0.4}Co_{0.15}Al_{0.05}Mn_{0.4})O_2$ Cathode Material, *Journal of The Electrochemical Society*, 2010, **157**, A1317–A1322.

[255] S. Kuppan, Y. Xu, Y. Liu and G. Chen, Phase transformation mechanism in lithium manganese nickel oxide revealed by single-crystal hard X-ray microscopy, *Nature Communications*, 2017, **8**, 14309.

[256] W. E. Gent, Y. Li, S. Ahn, J. Lim, Y. Liu, A. M. Wise, C. B. Gopal, D. N. Mueller, R. Davis, J. N. Weker, J.-H. Park, S.-K. Doo and W. C. Chueh, Persistent State-of-Charge Heterogeneity in Relaxed, Partially Charged $Li_{1-x}Ni_{1/3}Co_{1/3}Mn_{1/3}O_2$ Secondary Particles, *Advanced Materials*, 2016, **28**, 6631–6638.

[257] S. M. Webb, SIXPack a Graphical User Interface for XAS Analysis Using IFEFFIT, *Physica Scripta*, 2005, **2005**, 1011–1014.

[258] J. C. Andrews, F. Meirer, Y. Liu, Z. Mester and P. Pianetta, Transmission X-ray microscopy for full-field nano imaging of biomaterials, *Microscopy Research and Technique*, 2011, **74**, 671–681.

[259] J. C. Andrews and B. M. Weckhuysen, Hard X-ray spectroscopic nano-imaging of hierarchical functional materials at work, *ChemPhysChem*, 2013, **14**, 3655–3666.

[260] Y. Liu, J. C. Andrews, J. Wang, F. Meirer, P. Zhu, Z. Wu and P. Pianetta, Phase

retrieval using polychromatic illumination for transmission X-ray microscopy, *Optics Express*, 2011, **19**, 540–545.

[261] F. Meirer, J. Cabana, Y. Liu, A. Mehta, J. C. Andrews and P. Pianetta, Three-dimensional imaging of chemical phase transformations at the nanoscale with full-field transmission X-ray microscopy, *Journal of Synchrotron Radiation*, 2011, **18**, 773–781.

[262] B. Ravel and M. Newville, ATHENA, ARTEMIS, HEPHAESTUS: Data analysis for X-ray absorption spectroscopy using IFEFFIT, *Journal of Synchrotron Radiation*, 2005, **12**, 537–541.

[263] V. A. Solé, E. Papillon, M. Cotte, P. Walter and J. Susini, A multiplatform code for the analysis of energy-dispersive X-ray fluorescence spectra, *Spectrochimica Acta - Part B Atomic Spectroscopy*, 2007, **62**, 63–68.

[264] Y. Liu, F. Meirer, P. A. Williams, J. Wang, J. C. Andrews and P. Pianetta, TXM-Wizard: A program for advanced data collection and evaluation in full-field transmission X-ray microscopy, *Journal of Synchrotron Radiation*, 2012, **19**, 281–287.

[265] B. Xu, C. R. Fell, M. Chi and Y. S. Meng, Identifying surface structural changes in layered Li-excess nickel manganese oxides in high voltage lithium ion batteries: A joint experimental and theoretical study, *Energy and Environmental Science*, 2011, **4**, 2223.

[266] L. Li, S. Basu, Y. Wang, Z. Chen, P. Hundekar, B. Wang, J. Shi, Y. Shi, S. Narayanan and N. Koratkar, Self-heating–induced healing of lithium dendrites, *Science*, 2018, **359**, 1513–1516.

[267] K. W. Nam, W. S. Yoon and X. Q. Yang, Structural changes and thermal stability of charged $LiNi_{1/3}Co_{1/3}Mn_{1/3}O_2$ cathode material for Li-ion batteries studied by time-resolved XRD, *Journal of Power Sources*, 2009, **189**, 515–518.

[268] T. Okumura, M. Shikano and H. Kobayashi, Contribution of oxygen partial density of state on lithium intercalation/de-intercalation process in $Li_xNi_{0.5}Mn_{1.5}O_4$ spinel oxides, *Journal of Power Sources*, 2013, **244**, 544–547.

[269] F. M. F. de Groot, J. Faber, J. J. M. Michiels, M. T. Czyżyk, M. Abbate and J. C. Fuggle, Oxygen 1s x-ray absorption of tetravalent titanium oxides: A comparison with single-particle calculations, *Physical Review B*, 1993, **48**, 2074–2080.

[270] J.-H. Cheng, C.-J. Pan, J.-F. Lee, J.-M. Chen, M. Guignard, C. Delmas, D. Carlier and B.-J. Hwang, Simultaneous Reduction of Co^{3+} and Mn^{4+} in P2-$Na_{2/3}Co_{2/3}Mn_{1/3}O_2$ As Evidenced by X-ray Absorption Spectroscopy during Electrochemical Sodium Intercalation, *Chemistry of Materials*, 2014, **26**, 1219–1225.

[271] M. G. Kim, H. J. Shin, J.-H. Kim, S.-H. Park and Y.-K. Sun, XAS Investigation

of Inhomogeneous Metal-Oxygen Bond Covalency in Bulk and Surface for Charge Compensation in Li-Ion Battery Cathode Li[$Ni_{1/3}Co_{1/3}Mn_{1/3}$]O_2 Material, *Journal of The Electrochemical Society*, 2005, **152**, A1320.

[272] M. Balasubramanian, X. Sun, X. Q. Yang and J. McBreen, In Situ X-Ray Absorption Studies of a High-Rate $LiNi_{0.85}Co_{0.15}O_2$ Cathode Material, *Journal of The Electrochemical Society*, 2000, **147**, 2903.

[273] Y. Terada, K. Yasaka, F. Nishikawa, T. Konishi, M. Yoshio and I. Nakai, In Situ XAFS Analysis of Li(Mn, M)$_2O_4$ (M = Cr, Co, Ni) 5 V Cathode Materials for Lithium-Ion Secondary Batteries, *Journal of Solid State Chemistry*, 2001, **156**, 286–291.

[274] J. Xu, F. Lin, M. M. Doeff and W. Tong, A review of Ni-based layered oxides for rechargeable Li-ion batteries, *Journal of Materials Chemistry A*, 2017, **5**, 874–901.

[275] C. Wei, S. Xia, H. Huang, Y. Mao, P. Pianetta and Y. Liu, Mesoscale Battery Science: The Behavior of Electrode Particles Caught on a Multispectral X-ray Camera, *Accounts of Chemical Research*, 2018, **51**, 2484–2492.

[276] M. M. Besli, *Video A.1: FIB-SEM milling of an as-prepared $Li_{0.3}$NCA particle captured using the TLD (accessed: 01/14/2021)*, 2019, https://drive.google.com/open?id=19p0T8S6oIhVJ10SBVdG9Jc6xfV2qeU-d.

[277] M. M. Besli, *Video A.2: FIB-SEM milling of a heat-treated $Li_{0.3}$NCA particle captured using the TLD (accessed: 01/14/2020)*, 2019, https://drive.google.com/open?id=1qvTCIFQ6VG5DJDPrHSb1tH01axGldaDe.

[278] J. Schindelin, I. Arganda-Carreras, E. Frise, V. Kaynig, M. Longair, T. Pietzsch, S. Preibisch, C. Rueden, S. Saalfeld, B. Schmid, J. Y. Tinevez, D. J. White, V. Hartenstein, K. Eliceiri, P. Tomancak and A. Cardona, Fiji: An open-source platform for biological-image analysis, *Nature Methods*, 2012, **9**, 676–682.

[279] M. Hall, E. Frank, G. Holmes, B. Pfahringer, P. Reutemann and I. H. Witten, The WEKA data mining software, *ACM SIGKDD Explorations Newsletter*, 2009, **11**, 10–18.

[280] I. Arganda-Carreras, V. Kaynig, C. Rueden, K. W. Eliceiri, J. Schindelin, A. Cardona and H. Sebastian Seung, Trainable Weka Segmentation: a machine learning tool for microscopy pixel classification, *Bioinformatics*, 2017, **33**, 2424–2426.

[281] X. Liu, G.-L. Xu, L. Yin, I. Hwang, Y. Li, L. Lu, W. Xu, X. Zhang, Y. Chen, Y. Ren, C.-J. Sun, Z. Chen, M. Ouyang and K. Amine, Probing the Thermal-Driven Structural and Chemical Degradation of Ni-Rich Layered Cathodes by Co/Mn Exchange, *Journal of the American Chemical Society*, 2020, **142**, 19745–19753.

[282] H. Xia, C. Liu, L. Shen, J. Yu, B. Li, F. Kang and Y. B. He, Structure and ther-

mal stability of $\mathrm{LiNi_{0.8}Co_{0.15}Al_{0.05}O_2}$ after long cycling at high temperature, *Journal of Power Sources*, 2020, **450**, 227695.

[283] K. Karki, Y. Huang, S. Hwang, A. D. Gamalski, M. S. Whittingham, G. Zhou and E. A. Stach, Tuning the Activity of Oxygen in $\mathrm{LiNi_{0.8}Co_{0.15}Al_{0.05}O_2}$ Battery Electrodes, *ACS Applied Materials & Interfaces*, 2016, **8**, 27762–27771.

[284] P. Mukherjee, N. V. Faenza, N. Pereira, J. Ciston, L. F. J. Piper, G. G. Amatucci and F. Cosandey, Surface Structural and Chemical Evolution of Layered $\mathrm{LiNi_{0.8}Co_{0.15}Al_{0.05}O_2}$ (NCA) under High Voltage and Elevated Temperature Conditions, *Chemistry of Materials*, 2018, **30**, 8431–8445.

[285] C. S. Yoon, M. H. Choi, B.-B. Lim, E.-J. Lee and Y.-K. Sun, Review—High-Capacity $\mathrm{Li[Ni_{1-x}Co_{x/2}Mn_{x/2}]O_2}$ (x = 0.1, 0.05, 0) Cathodes for Next-Generation Li-Ion Battery, *Journal of The Electrochemical Society*, 2015, **162**, A2483–A2489.

[286] I. Belharouak, W. Lu, D. Vissers and K. Amine, Safety characteristics of $\mathrm{Li(Ni_{0.8}Co_{0.15}Al_{0.05})O_2}$ and $\mathrm{Li(Ni_{1/3}Co_{1/3}Mn_{1/3})O_2}$, *Electrochemistry Communications*, 2006, **8**, 329–335.

[287] I. Belharouak, D. Vissers and K. Amine, Thermal Stability of the $\mathrm{Li(Ni_{0.8}Co_{0.15}Al_{0.05})O_2}$ Cathode in the Presence of Cell Components, *Journal of The Electrochemical Society*, 2006, **153**, A2030.

[288] Y. Huang, Y.-C. Lin, D. M. Jenkins, N. A. Chernova, Y. Chung, B. Radhakrishnan, I.-H. Chu, J. Fang, Q. Wang, F. Omenya, S. P. Ong and M. S. Whittingham, Thermal Stability and Reactivity of Cathode Materials for Li-Ion Batteries, *ACS Applied Materials & Interfaces*, 2016, **8**, 7013–7021.

[289] H. Beyer, S. Meini, N. Tsiouvaras, M. Piana and H. A. Gasteiger, Thermal and electrochemical decomposition of lithium peroxide in non-catalyzed carbon cathodes for Li–air batteries, *Physical Chemistry Chemical Physics*, 2013, **15**, 11025–11037.

[290] C. Usubelli, M. M. Besli, S. Kuppan, N. Jiang, M. Metzger, A. Dinia, J. Christensen and Y. Gorlin, Understanding the Overlithiation Properties of $\mathrm{LiNi_{0.6}Mn_{0.2}Co_{0.2}O_2}$ Using Electrochemistry and Depth-Resolved X-ray Absorption Spectroscopy, *Journal of The Electrochemical Society*, 2020, **167**, 080514.

[291] K.-W. Nam and X.-Q. Yang, 2013 DOE Hydrogen Program and Vehicle Technologies Annual Merit Review and Peer Evaluation Meeting Washington, DC, May 13-17, 2013.

[292] W.-S. Yoon, K. Y. Chung, J. McBreen, D. A. Fischer and X.-Q. Yang, Changes in electronic structure of the electrochemically Li-ion deintercalated $\mathrm{LiNiO_2}$ system investigated by soft X-ray absorption spectroscopy, *Journal of Power Sources*, 2006, **163**, 234–237.

[293] J. Xu, E. Hu, D. Nordlund, A. Mehta, S. N. Ehrlich, X.-q. Yang and W. Tong,

Understanding the Degradation Mechanism of Lithium Nickel Oxide Cathodes for Li-Ion Batteries, *ACS Applied Materials & Interfaces*, 2016, **8**, 31677–31683.

[294] M. M. Besli, *Video A.3: FIB-SEM milling of a pristine NCA particle captured in mirror mode (accessed 01/14/2021)*, 2019, https://pubs.acs.org/doi/suppl/10.1021/acs.chemmater.8b04418/suppl_file/cm8b04418_si_002.avi.

[295] M. M. Besli, *Video A.4: FIB-SEM milling of a pristine NCA particle captured using the TLD (accessed: 01/14/2021)*, 2019, https://pubs.acs.org/doi/suppl/10.1021/acs.chemmater.8b04418/suppl_file/cm8b04418_si_003.avi.

[296] A. O. Kondrakov, A. Schmidt, J. Xu, H. Geßwein, R. Mönig, P. Hartmann, H. Sommer, T. Brezesinski and J. Janek, Anisotropic Lattice Strain and Mechanical Degradation of High- and Low-Nickel NCM Cathode Materials for Li-Ion Batteries, *Journal of Physical Chemistry C*, 2017, **121**, 3286–3294.

[297] J.-M. Lim, T. Hwang, D. Kim, M.-S. Park, K. Cho and M. Cho, Intrinsic Origins of Crack Generation in Ni-rich $LiNi_{0.8}Co_{0.1}Mn_{0.1}O_2$ Layered Oxide Cathode Material, *Scientific Reports*, 2017, **7**, 39669.

[298] H. Liu, M. Wolf, K. Karki, Y.-S. Yu, E. A. Stach, J. Cabana, K. W. Chapman and P. J. Chupas, Intergranular Cracking as a Major Cause of Long-Term Capacity Fading of Layered Cathodes, *Nano Letters*, 2017, **17**, 3452–3457.

[299] H. Zhang, F. Omenya, P. Yan, L. Luo, M. S. Whittingham, C. Wang and G. Zhou, Rock-Salt Growth-Induced (003) Cracking in a Layered Positive Electrode for Li-Ion Batteries, *ACS Energy Letters*, 2017, **2**, 2607–2615.

[300] C. S. Yoon, H. H. Ryu, G. T. Park, J. H. Kim, K. H. Kim and Y. K. Sun, Extracting maximum capacity from Ni-rich $Li[Ni_{0.95}Co_{0.025}Mn_{0.025}]O_2$ cathodes for high-energy-density lithium-ion batteries, *Journal of Materials Chemistry A*, 2018, **6**, 4126–4132.

[301] M. M. Besli, *Sheet A.1: Calculation of the volume fraction corresponding to mesopore formation (accessed: 04/17/2021)*, 2019, http://www.rsc.org/suppdata/c9/ta/c9ta01720h/c9ta01720h1.xlsx.

[302] R. Jung, M. Metzger, F. Maglia, C. Stinner and H. A. Gasteiger, Chemical versus Electrochemical Electrolyte Oxidation on NMC111, NMC622, NMC811, LNMO, and Conductive Carbon, *The Journal of Physical Chemistry Letters*, 2017, **8**, 4820–4825.

[303] B. Strehle, K. Kleiner, R. Jung, F. Chesneau, M. Mendez, H. A. Gasteiger and M. Piana, The Role of Oxygen Release from Li- and Mn-Rich Layered Oxides during the First Cycles Investigated by On-Line Electrochemical Mass Spectrometry, *Journal of The Electrochemical Society*, 2017, **164**, A400–A406.

[304] A. Manthiram, K. Chemelewski and E.-S. Lee, A perspective on the high-voltage $LiMn_{1.5}Ni_{0.5}O_4$ spinel cathode for lithium-ion batteries, *Energy & Environmental Science*, 2014, **7**, 1339–1350.

[305] Y. Wang, J. Jiang and J. R. Dahn, The reactivity of delithiated

$Li(Ni_{1/3}Co_{1/3}Mn_{1/3})O_2$, $Li(Ni_{0.8}Co_{0.15}Al_{0.05})O_2$ or $LiCoO_2$ with non-aqueous electrolyte, *Electrochemistry Communications*, 2007, **9**, 2534–2540.

[306] Z. Li, N. A. Chernova, J. Feng, S. Upreti, F. Omenya and M. S. Whittingham, Stability and Rate Capability of Al Substituted Lithium-Rich High-Manganese Content Oxide Materials for Li-Ion Batteries, *Journal of The Electrochemical Society*, 2012, **159**, A116–A120.

[307] J. D. Steiner, L. Mu, J. Walsh, M. M. Rahman, B. Zydlewski, F. M. Michel, H. L. Xin, D. Nordlund and F. Lin, Accelerated Evolution of Surface Chemistry Determined by Temperature and Cycling History in Nickel-Rich Layered Cathode Materials, *ACS Applied Materials & Interfaces*, 2018, **10**, 23842–23850.

[308] M. Lécuyer, J. Gaubicher, A.-L. Barrès, F. Dolhem, M. Deschamps, D. Guyomard and P. Poizot, A rechargeable lithium/quinone battery using a commercial polymer electrolyte, *Electrochemistry Communications*, 2015, **55**, 22–25.

[309] Q. Hu, The renaissance of lithium metal: SolidEnergy's role in the future of lithium batteries, *Nature*, 2015, **526**, 102–105.

[310] K. Jarvis, C. C. Wang, M. Varela, R. R. Unocic, A. Manthiram and P. J. Ferreira, Surface Reconstruction in Li-Rich Layered Oxides of Li-Ion Batteries, *Chemistry of Materials*, 2017, **29**, 7668–7674.

[311] H. Zhang, K. Karki, Y. Huang, M. S. Whittingham, E. A. Stach and G. Zhou, Atomic insight into the layered/spinel phase transformation in charged $LiNi_{0.80}Co_{0.15}Al_{0.05}O_2$ cathode particles, *Journal of Physical Chemistry C*, 2017, **121**, 1421–1430.

[312] P. Lu, P. Yan, E. Romero, E. D. Spoerke, J.-G. Zhang and C.-M. Wang, Observation of Electron-Beam-Induced Phase Evolution Mimicking the Effect of the Charge–Discharge Cycle in Li-Rich Layered Cathode Materials Used for Li Ion Batteries, *Chemistry of Materials*, 2015, **27**, 1375–1380.

[313] M. Lin, L. Ben, Y. Sun, H. Wang, Z. Yang, L. Gu, X. Yu, X.-q. Yang, H. Zhao, R. Yu, M. Armand and X. Huang, Insight into the Atomic Structure of High-Voltage Spinel $LiNi_{0.5}Mn_{1.5}O_4$ Cathode Material in the First Cycle, *Chemistry of Materials*, 2015, **27**, 292–303.

[314] J. Zheng, P. Xu, M. Gu, J. Xiao, N. D. Browning, P. Yan, C. Wang and J. G. Zhang, Structural and chemical evolution of Li- and Mn-rich layered cathode material, *Chemistry of Materials*, 2015, **27**, 1381–1390.

[315] J. W. Boyd, P. W. Schmalzl and L. L. Miller, Mechanism of anodic cleavage of benzyl ethers, *Journal of the American Chemical Society*, 1980, **102**, 3856–3862.

[316] D. T. Hallinan, A. Rausch and B. McGill, An electrochemical approach to measuring oxidative stability of solid polymer electrolytes for lithium batteries, *Chemical Engineering Science*, 2016, **154**, 34–41.

[317] D. T. Hallinan, M. Majeed, K. Kim and M. Berliner, Electrochemical Kinetics in Solid Battery Electrolytes, *ECS Meeting Abstracts*, 2019, **MA2019-02**, 640.

[318] P. de Sainte Claire, Degradation of PEO in the Solid State: A Theoretical Kinetic Model, *Macromolecules*, 2009, **42**, 3469–3482.

[319] H. Stendzenberger, K. Heinen and D. Hummel, Thermal degradation of poly (ethyleneglycol), *Journal of Polymer Science: Polymer Chemistry Edition*, 1976, **14**, 2911–2925.

[320] S. Z. D. Cheng and B. Wunderlich, Molecular segregation and nucleation of poly(ethylene oxide) crystallized from the melt. I. Calorimetric study, *Journal of Polymer Science Part B: Polymer Physics*, 1986, **24**, 577–594.

[321] L. D. Ellis, J. Xia, A. J. Louli and J. R. Dahn, Effect of substituting $LiBF_4$ for $LiPF_6$ in high voltage lithium-ion cells containing electrolyte additives, *Journal of the Electrochemical Society*, 2016, **163**, A1686–A1692.

[322] L. D. Ellis, I. G. Hill, K. L. Gering and J. R. Dahn, Synergistic Effect of $LiPF_6$ and $LiBF_4$ as Electrolyte Salts in Lithium-Ion Cells, *Journal of The Electrochemical Society*, 2017, **164**, A2426–A2433.

[323] S. S. Zhang, K. Xu and T. R. Jow, An improved electrolyte for the $LiFePO_4$ cathode working in a wide temperature range, *Journal of Power Sources*, 2006, **159**, 702–707.

[324] C. Shen, D. Xiong, L. D. Ellis, K. L. Gering, L. Huang and J. R. Dahn, Using the charge-discharge cycling of positive electrode symmetric cells to find electrolyte/electrode combinations with minimum reactivity, *Journal of the Electrochemical Society*, 2017, **164**, A3349–A3356.

[325] T. Doi, Y. Shimizu, M. Hashinokuchi and M. Inaba, $LiBF_4$-Based Concentrated Electrolyte Solutions for Suppression of Electrolyte Decomposition and Rapid Lithium-Ion Transfer at $LiNi_{0.5}Mn_{1.5}O_4$/Electrolyte Interface, *Journal of the Electrochemical Society*, 2016, **163**, A2211–A2215.

[326] T. Doi, Y. Shimizu, M. Hashinokuchi and M. Inaba, Dilution of Highly Concentrated $LiBF_4$/Propylene Carbonate Electrolyte Solution with Fluoroalkyl Ethers for 5-V $LiNi_{0.5}Mn_{1.5}O_4$ Positive Electrodes, *Journal of the Electrochemical Society*, 2017, **164**, A6412–A6416.

[327] X. Zuo, C. Fan, X. Xiao, J. Wu, J. Nan and J. Liu, Lithium Tetrafluoroborate as an Electrolyte Additive to Improve the High Voltage Performance of Lithium-ion Battery, *Journal of the Electrochemical Society*, 2013, **160**, A1199–A1204.

[328] Z. Lu, L. Yang and Y. Guo, Thermal behavior and decomposition kinetics of six electrolyte salts by thermal analysis, *Journal of Power Sources*, 2006, **156**, 555–559.

[329] L. Cheng, H. B. Eitouni, S. Hellstrom, Y. Huang, S. Kuppan, M. Metzger and T. Palmer, High-energy Cathode Material Particles With Oxy-fluoride Surfaces For Aqueous Processing, *US Patent Application No.: 20200106105 16/218475*, 2020.

[330] D. Aurbach, B. Markovsky, G. Salitra, E. Markevich, Y. Talyossef, M. Koltypin,

L. Nazar, B. Ellis and D. Kovacheva, Review on electrode-electrolyte solution interactions, related to cathode materials for Li-ion batteries, *Journal of Power Sources*, 2007, **165**, 491–499.

[331] G. G. Amatucci, J. M. Tarascon and L. C. Klein, CoO_2, The End Member of the Li_xCoO_2 Solid Solution, *Journal of The Electrochemical Society*, 1996, **143**, 1114.

[332] J. L. Tebbe, A. M. Holder and C. B. Musgrave, Mechanisms of $LiCoO_2$ Cathode Degradation by Reaction with HF and Protection by Thin Oxide Coatings, *ACS Applied Materials & Interfaces*, 2015, **7**, 24265–24278.

[333] M. Aykol, S. Kim, V. I. Hegde, D. Snydacker, Z. Lu, S. Hao, S. Kirklin, D. Morgan and C. Wolverton, High-throughput computational design of cathode coatings for Li-ion batteries, *Nature Communications*, 2016, **7**, 1–12.

[334] P. C. Tsai, B. Wen, M. Wolfman, M. J. Choe, M. S. Pan, L. Su, K. Thornton, J. Cabana and Y. M. Chiang, Single-particle measurements of electrochemical kinetics in NMC and NCA cathodes for Li-ion batteries, *Energy and Environmental Science*, 2018, **11**, 860–871.

[335] M. M. Besli, *Video A.5: FIB-SEM milling of a NCA particle harvested after cycling captured in mirror mode (accessed: 01/14/2021)*, 2019, https://pubs.acs.org/doi/suppl/10.1021/acs.chemmater.8b04418/suppl_file/cm8b04418_si_004.avi.

[336] M. M. Besli, *Video A.6: FIB-SEM milling of a NCA particle harvested after cycling captured using the TLD (accessed: 01/14/2021)*, 2019, https://pubs.acs.org/doi/suppl/10.1021/acs.chemmater.8b04418/suppl_file/cm8b04418_si_005.avi.

[337] L. Wu, K.-W. Nam, X. Wang, Y. Zhou, J.-C. Zheng, X.-Q. Yang and Y. Zhu, Structural Origin of Overcharge-Induced Thermal Instability of Ni-Containing Layered-Cathodes for High-Energy-Density Lithium Batteries, *Chemistry of Materials*, 2011, **23**, 3953–3960.

[338] T. Ma, G. L. Xu, Y. Li, L. Wang, X. He, J. Zheng, J. Liu, M. H. Engelhard, P. Zapol, L. A. Curtiss, J. Jorne, K. Amine and Z. Chen, Revisiting the Corrosion of the Aluminum Current Collector in Lithium-Ion Batteries, *Journal of Physical Chemistry Letters*, 2017, **8**, 1072–1077.

[339] S. Sylla, J. Y. Sanchez and M. Armand, Electrochemical study of linear and crosslinked POE-based polymer electrolytes, *Electrochimica Acta*, 1992, **37**, 1699–1701.

[340] G. Liu, M. Li, N. Wu, L. Cui, X. Huang, X. Liu, Y. Zhao, H. Chen, W. Yuan and Y. Bai, Single-Crystalline Particles: An Effective Way to Ameliorate the Intragranular Cracking, Thermal Stability, and Capacity Fading of the $LiNi_{0.6}Co_{0.2}Mn_{0.2}O_2$ Electrodes, *Journal of The Electrochemical Society*, 2018, **165**, A3040–A3047.

[341] D. Mohanty, K. Dahlberg, D. M. King, L. A. David, A. S. Sefat, D. L. Wood, C. Daniel, S. Dhar, V. Mahajan, M. Lee and F. Albano, Modification of Ni-Rich FCG NMC and NCA Cathodes by Atomic Layer Deposition: Preventing Surface Phase Transitions for High-Voltage Lithium-Ion Batteries, *Scientific Reports*, 2016, **6**, 26532.

A Appendix

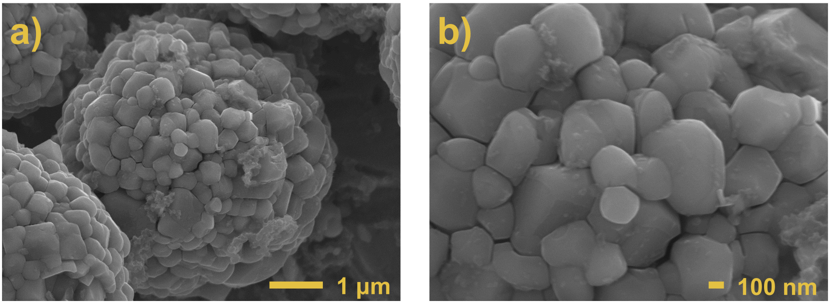

Figure A.1: (a) SEM image of a typical secondary NCA particle in its pristine state. (b) Higher magnification of the surface focusing on the primary particle grains with their smaller diameter.

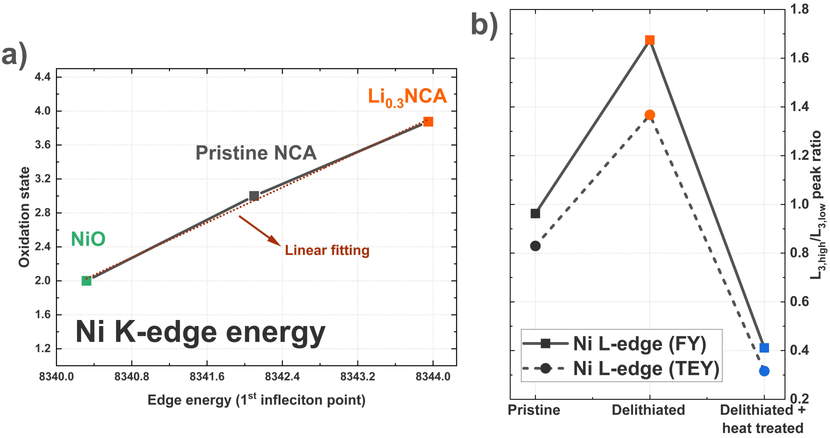

Figure A.2: (a) Edge energies derived from the 1st inflection point of Ni K-edge hard XAS spectra linearly fit to the oxidation state in order quantify the oxidation state of heat-treated $Li_{0.3}NCA$. (b) Ni $L_{3,high}/L_{3,low}$ ratios for surface and subsurface Ni in pristine NCA (black), as-prepared $Li_{0.3}NCA$ (orange), and heat-treated $Li_{0.3}NCA$ (blue).

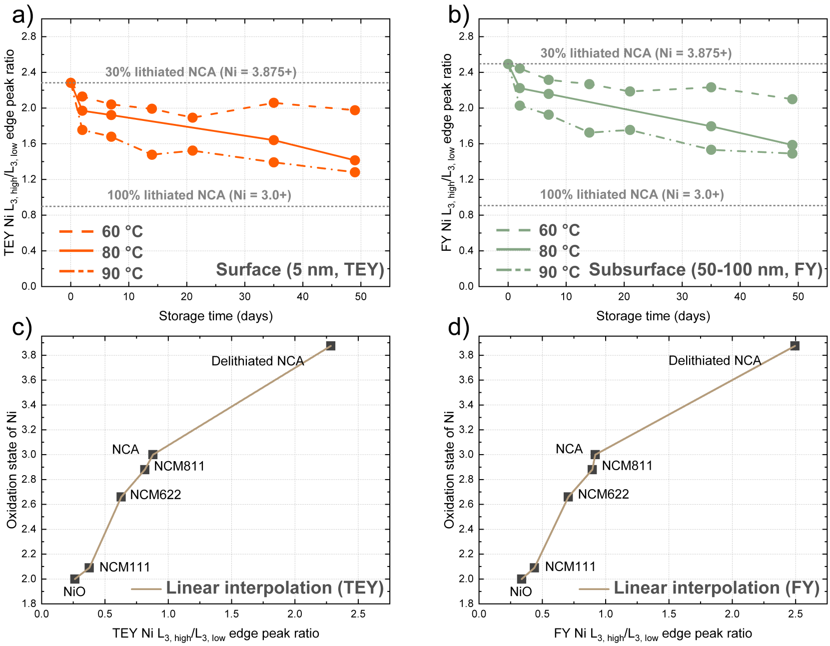

Figure A.3: (a) Ni TEY and (b) Ni FY $L_{3,\ \mathrm{high}}/L_{3,\ \mathrm{low}}$ peak ratios for $Li_{0.3}NCA$ stored at 60, 80 and 90 °C. The decomposition relative to the initial peak ratios/oxidation states of delithiated NCA and pristine NCA is indicated by the upper and lower dashed lines, respectively. (c) and (d) Linear interpolation for TEY and FY mode, respectively, correlating measured ratios to oxidation states of nickelate standards allows to find apparent Ni oxidation states and degrees of aging for aged samples.

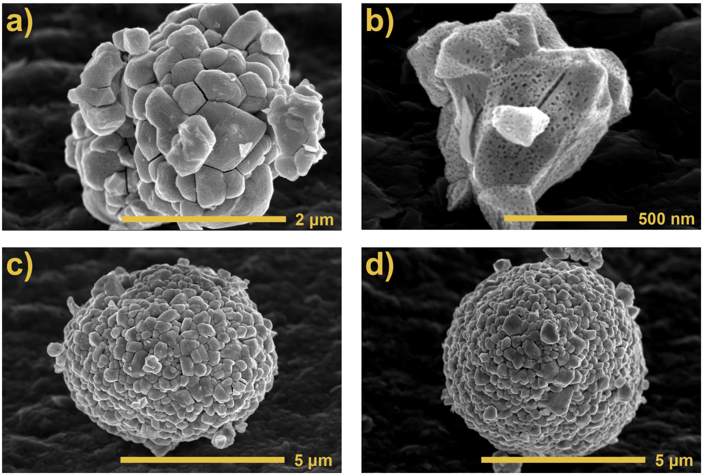

Figure A.4: (a-d) $Li_{0.3}$NCA particles of various sizes subjected to heat treatment showing mesopores on the surface.

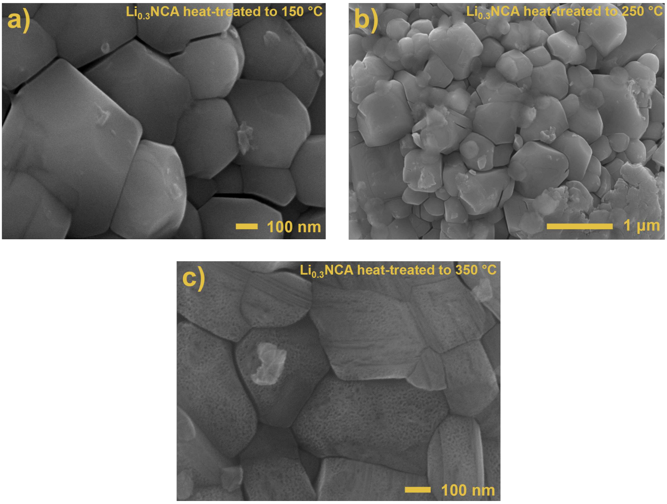

Figure A.5: SEM images of the surface of three batches of as-prepared $Li_{0.3}$NCA heated to (a) 150 °C, (b) 250 °C, and (c) 350 °C, respectively. No mesopores are observed on particles that were heated to 150 or 250 °C. Evolution of mesopores seem to start within a temperature range of above 300 °C and until 350 °C.

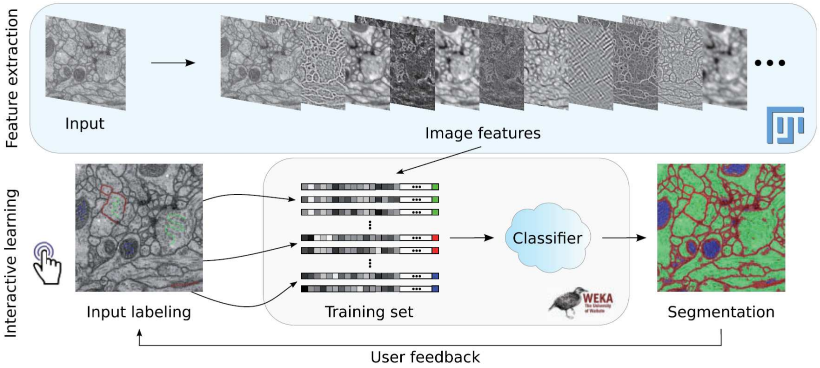

Figure A.6: Firstly, image features are extracted from an input image using the Fiji image processing toolkit and its methods. Secondly, a set of pixel samples is defined and represented as feature vectors. The feature vectors are subsequently used to train a WEKA learning scheme on those samples. Finally, the learning scheme is applied to classify the remaining image data, while the user can interactively provide feedback and correct or add labels [280]. Reproduced with permission from Arganda-Carreras et al. [280].

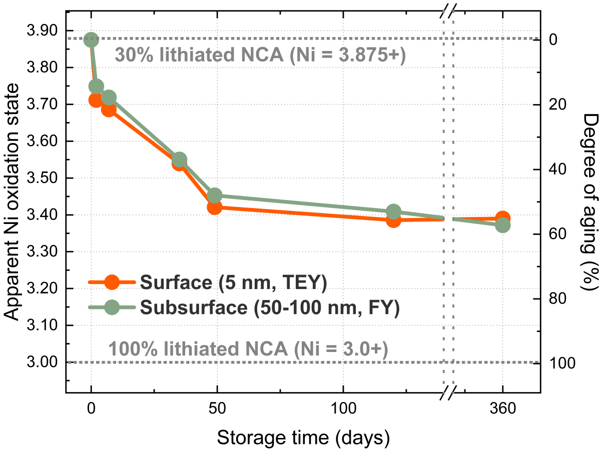

Figure A.7: TEY (orange) and FY (green) Ni L_3-edge ratio derived apparent Ni oxidation states and the correlated degrees of aging for delithiated $Li_{0.3}$NCA stored at 80 °C for up to 1 year. Ni reduction after the initial 49 days is very minimal and comparable with the apparent Ni oxidation state observed after 4 months and 1 year.

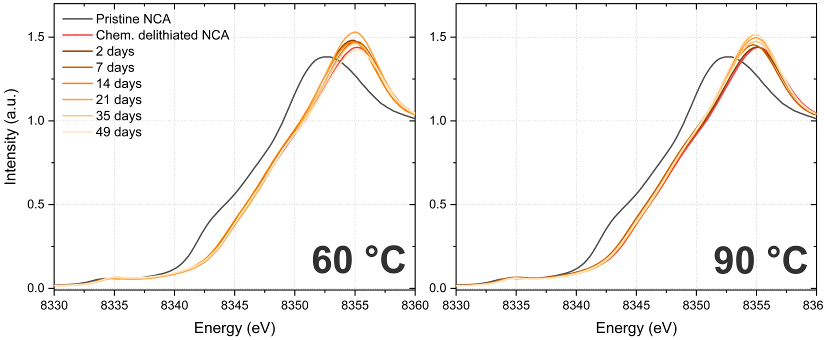

Figure A.8: Ni K-edge XANES spectra for pristine NCA, freshly delithiated $Li_{0.3}NCA$, and $Li_{0.3}NCA$ stored at (a) 60 °C, and (b) 90 °C for various lengths of time.

Combination	**TEY derived apparent oxidation state after 35 days**	**TEY derived degree of aging after 35 days**	**FY derived apparent oxidation state after 35 days**	**FY derived degree of aging after 35 days**	**Bulk apparent oxidation state after 35 days**	**Bulk degree of aging after 35 days**
Li$_{0.3}$NCA	3.54+	37%	3.55+	35%	3.84+	4%
+ PEO	2.53+	147%	2.83+	114%	3.29+	64%
+ PCL	3.33+	60%	3.45+	46%	3.50+	42%
+ LiBF$_4$	3.66+	24%	3.72+	17%	3.85+	2%
+ LiTFSI	2.66+	132%	3.17+	77%	3.69+	20%
+ PEO + LiBF$_4$	3.39+	53%	3.44+	47%	3.46+	45%
+ PCL + LiBF$_4$	3.62+	28%	3.69+	21%	3.73+	15%
+ PEO + LiTFSI	3.00+	96%	3.28+	65%	3.37+	56%
Li$_{0.3}$NMC811 + PCL	2.47+	147%	3.06+	80%	3.06+	80%
Li$_{0.3}$NMC811 + LiBF$_4$	3.31+	51%	3.45+	35%	3.68+	8%
Li$_{0.3}$NMC811 + PCL + LiBF$_4$	3.40+	40%	3.39+	42%	3.72+	3%
Li$_{0.3}$NMC622 + PCL	3.52+	27%	3.36+	40%	3.60+	19%
Li$_{0.3}$NMC622 + LiBF$_4$	3.68+	13%	3.71+	10%	3.80+	3%
Li$_{0.3}$NMC622 + PCL + LiBF$_4$	3.63+	17%	3.46+	32%	3.72+	10%

Table A.1: Apparent oxidation state and degree of aging in percent after storing samples for 35 days at 80 °C. Apparent oxidation state and degree of aging is shown for surface (TEY), subsurface (FY), and bulk.

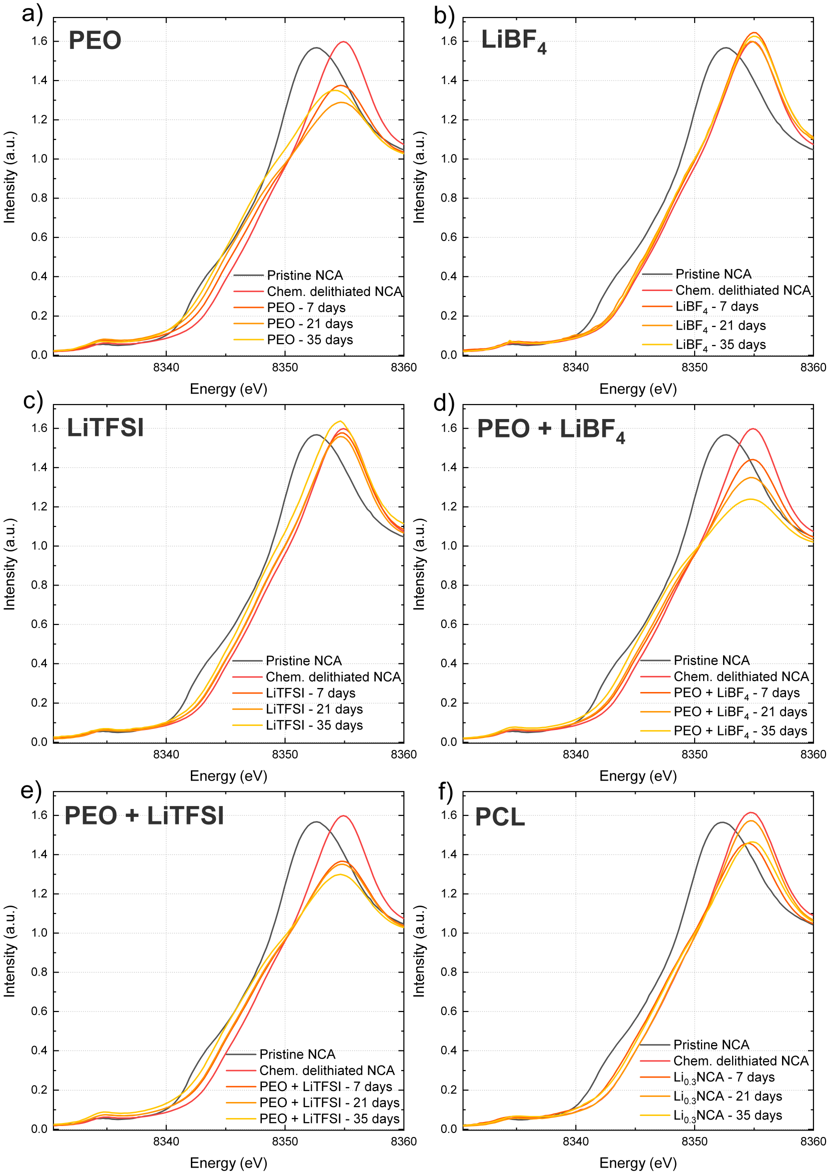

Figure A.9: Ni K-edge spectra for $Li_{0.3}$NCA in combination with (a) PEO, (b) $LiBF_4$, (c) LiTFSI, (d) PEO + $LiBF_4$, (e) PEO + LiTFSI, and (f) PCL stored at 80 °C for 7 days, 21 days and 35 days.

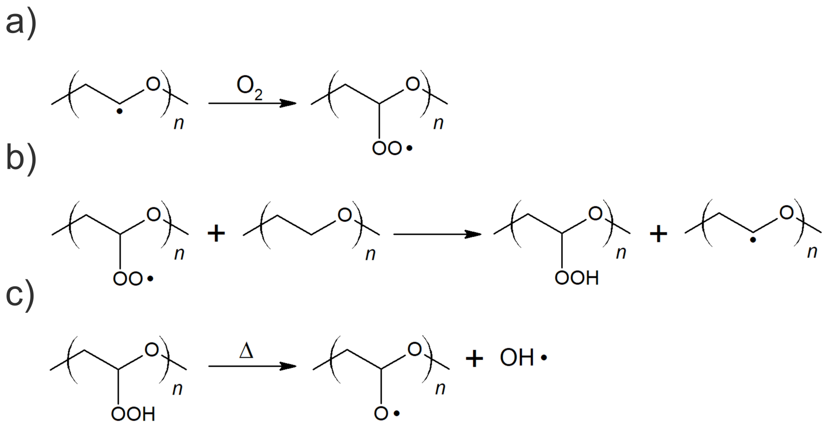

Figure A.10: (a) Addition of molecular oxygen to pre-existing radical sites forming hydroperoxide radicals. (b) Peroxide radicals reacting with side chains of the polymer (intermolecular). (c) Thermal dissociation of hydroperoxide radicals (monomolecular) forming alkoxy radicals and hydroxyl radicals. More details on this exact mechanism can be found in de Saint Claire [318].

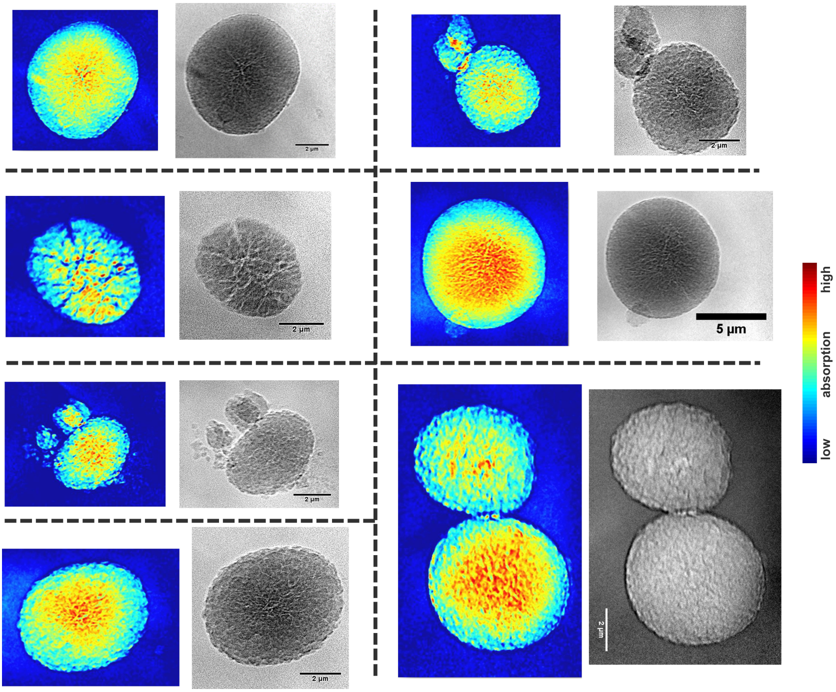

Figure A.11: 2D-FF-TXM transmission images of several cycled secondary NCA particles with varying diameters. On the left of each pair is the color-coded transmission images with the corresponding color map displayed on the very right of the image; the contrast in the 2D-FF-TXM projection images is directly proportional to the mass thickness of the particles. On the right of each pair: inverted greyscale images. Regardless of the particle size, cracks are observed in the center of the particles.

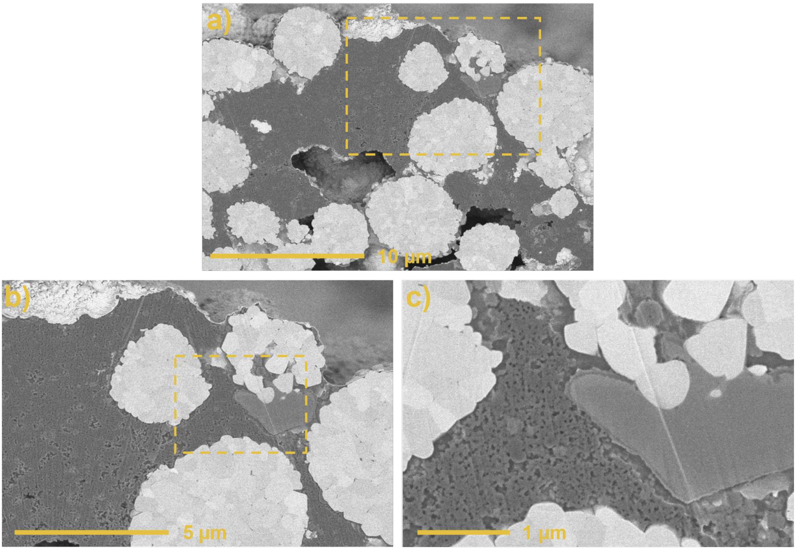

Figure A.12: BIB-SEM cross-sectional images of pristine NCA-PEO electrodes.

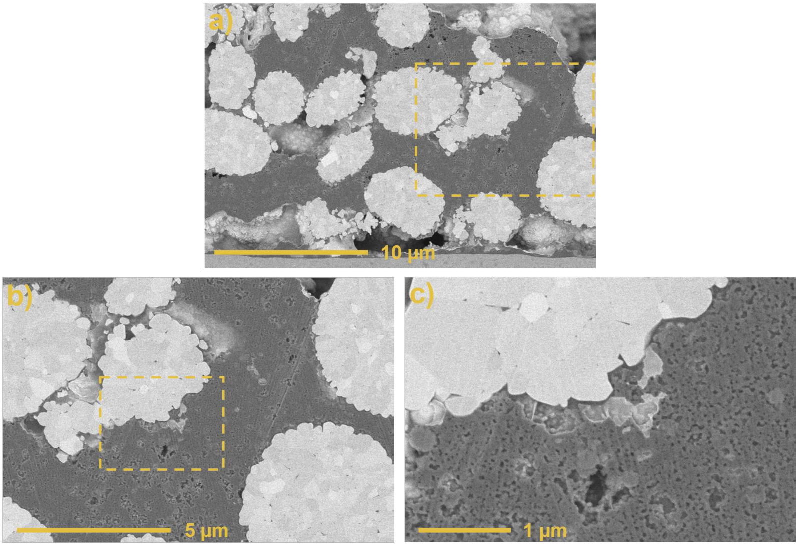

Figure A.13: BIB-SEM cross-sectional images of pristine NCA-PEO electrodes.

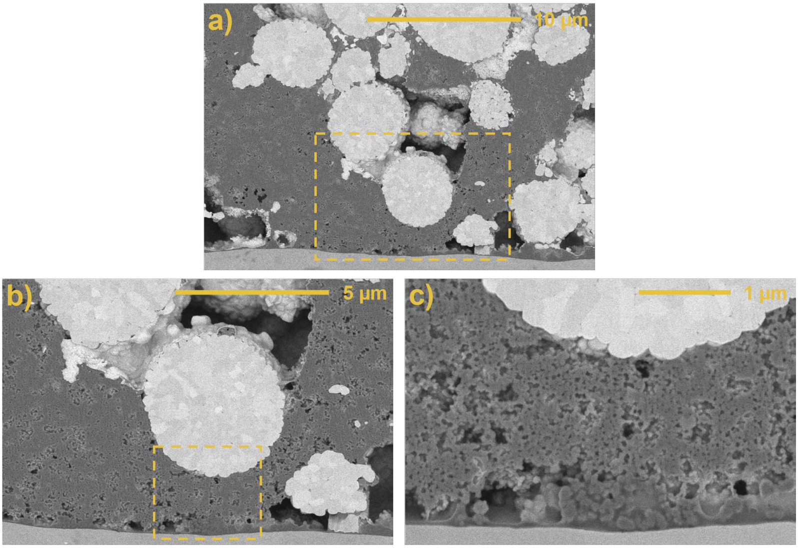

Figure A.14: BIB-SEM cross-sectional images of pristine NCA-PEO electrodes.

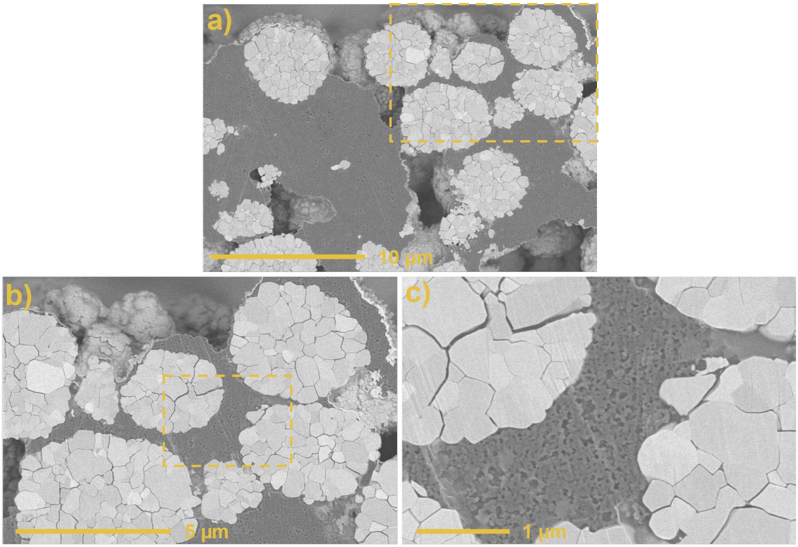

Figure A.15: BIB-SEM cross-sectional images of cycled NCA-PEO electrodes.

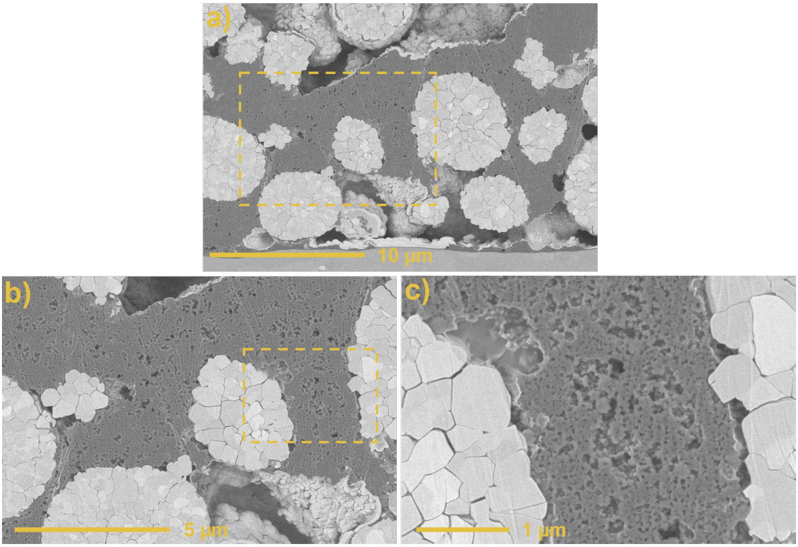

Figure A.16: BIB-SEM cross-sectional images of cycled NCA-PEO electrodes.

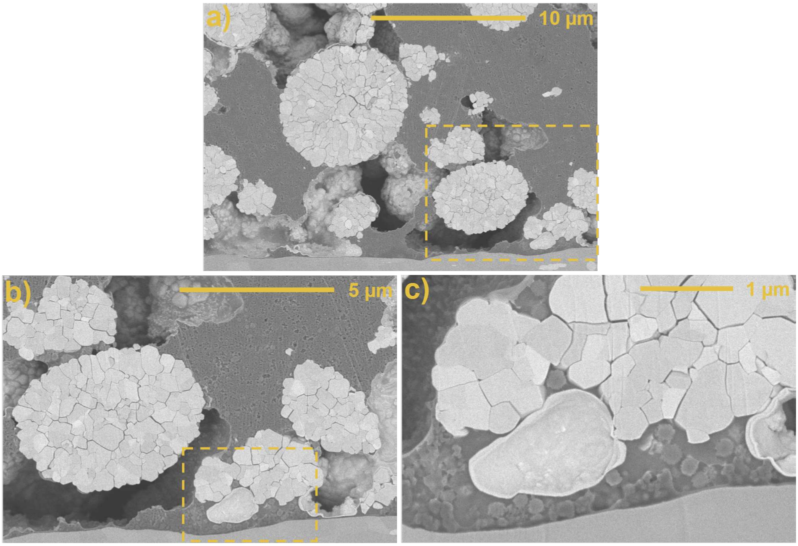

Figure A.17: BIB-SEM cross-sectional images of cycled NCA-PEO electrodes.

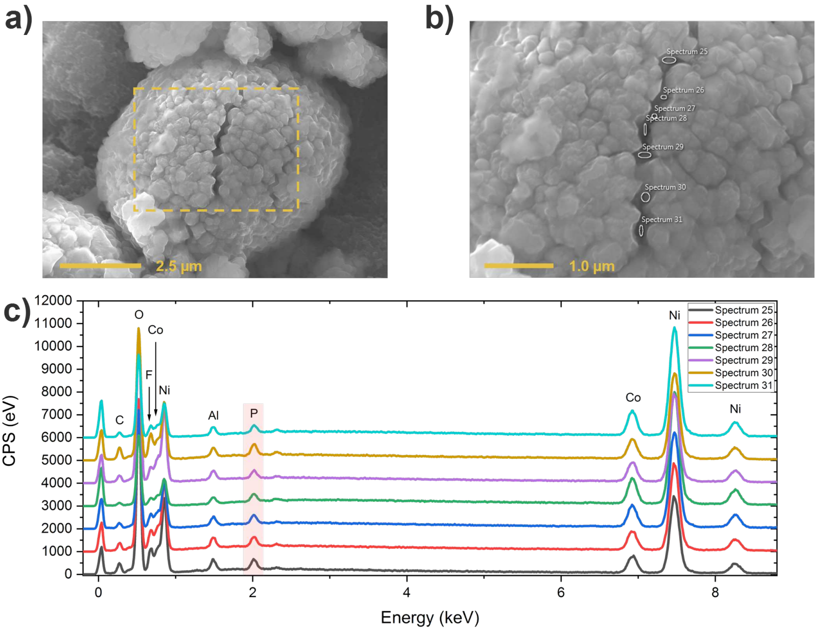

Figure A.18: (a) Secondary particle with an extensive intergranular crack on the surface after cycling and a high magnification image shown in (b). (c) Phosphorus peaks in EDS spectra of the highlighted areas in (b) show that electrolyte diffuses into intergranular cracks.

B Scientific Publications & Contributions

Peer-reviewed journal publications:

1. M. M. Besli, S. Xia, S. Kuppan, Y. Huang, M. Metzger, A. K. Shukla, G. Schneider, S. Hellstrom, J. Christensen, M. M. Doeff, Y. Liu, Mesoscale Chemomechanical Interplay of the $LiNi_{0.8}Co_{0.15}Al_{0.05}O_2$ Cathode in Solid-State Polymer Batteries, *Chemistry of Materials*, 2019, **31**, 491-501.
2. M. M. Besli, A. K. Shukla, C. Wei, M. Metzger, J. Alvarado, J. Boell, D. Nordlund, G. Schneider, S. Hellstrom, C. Johnston, J. Christensen, M. M. Doeff, Y. Liu, S. Kuppan, Thermally-driven mesopore formation and oxygen release in delithiated NCA cathode particles, *Journal of Materials Chemistry A*, 2019, **7**, 12593-12603.
3. M. M. Besli, C. Usubelli, M. Metzger, S. Hellstrom, S. Sainio, D. Nordlund, J. Christensen, G. Schneider, M. M. Doeff, S. Kuppan, Long-Term Chemothermal Stability of Delithiated NCA in Polymer Solid-State Batteries, *Journal of Materials Chemistry A*, 2019, **7**, 27135-27147.
4. M. Metzger, M. M. Besli, S. Kuppan, S. Hellstrom, S. Kim, E. Sebti, C. V. Subban, J. Christensen, Techno-economic analysis of capacitive and intercalative water deionization, *Energy and Environmental Science*, 2019, **13**, 1544-1560.
5. K. Kimura, R. Wilhelm, M. M. Besli, S. Kim, C. Usubelli, J. C. Ziegler, R. Klein, J. Christensen, Y. Gorlin, Interrelationship Between the Open Circuit Potential Curves in a Class of Ni-Rich Cathode Materials, *Journal of the Electrochemical Society*, 2020, **167**, 040510.
6. M. M. Besli, C. Usubelli, M. Metzger, V. Pande, K. Harry, D. Nordlund, S. Sainio, J. Christensen, M. M. Doeff, S. Kuppan, Effect of Liquid Electrolyte Soaking on the Interfacial Resistance of $Li_7La_3Zr_2O_{12}$ for All-Solid-State Lithium Batteries, *ACS Applied Materials & Interfaces*, 2020, **12**, 20605-20612.
7. C. Usubelli, M. M. Besli, S. Kuppan, N. Jiang, M. Metzger, A. Dinia, J. Christensen, Y. Gorlin, Understanding the Overlithiation Properties of $LiNi_{0.6}Mn_{0.2}Co_{0.2}O_2$ Using Electrochemistry and Depth-Resolved X-ray Absorption Spectroscopy, *Journal of the Electrochemical Society*, 2020, **167**, 080514.
8. E. Sebti, M. M. Besli, M. Metzger, S. Hellstrom, M. J. Schultz-Neu, J. Alvarado, J. Christensen, M. M. Doeff, S. Kuppan, C. V. Subban, Removal of Na^+ and Ca^{2+} with Prussian blue analogue electrodes for brackish water desalination, *Desalination*, 2020, **487**, 114479.

9. M. M. Besli, A. Subbaraman, F. R. Pour Safaei, C. Johnston, G. Schneider, N. Ravi, J. Christensen, Y. Liu, M. M. Doeff, M. Metzger, S. Kuppan, A study of model-based protective fast-charging and associated degradation in commercial smartphone cells: insights on cathode degradation as a result of lithium depositions on the anode, *Advanced Energy Materials*, 2021, **11**, 2003019.
10. X. Zhang, M. Klinsmann, S. Chumakov, X. Li, S. U. Kim, M. Metzger, M. M. Besli, R. Klein, C. Linder, J. Christensen, A modified electrochemical model to account for mechanical effects due to lithium intercalation and external pressure, *Journal of Electrochemical Society*, 2021, **168**, 020533.
11. K. Khedekar, M. R. Talarposhti, L. Cheng, M. M. Besli, S. Kuppan, A. Perego, Y. Chen, M. Metzger, S. Stewart, P. Atanassov, N. Tamura, N. Craig, C. Johnston, I. V. Zenyuk, Probing Heterogeneous Degradation of Catalyst in PEM Fuel Cells Under Realistic Automotive Conditions with Multi-modal Techniques, submitted to *Energy and Environmental Science*, 2021.
12. M. M. Besli, C. Usubelli, A. Subbaraman, F. R. Pour Safaei, S. Bone, C. Johnston, G. Schneider, F. Beauchaud, N. Ravi, J. Christensen, M. M. Doeff, M. Metzger, S. Kuppan, Location Dependent Cobalt Deposition in Smartphone Cells Upon Long-term Fast-charging Visualized by Synchrotron X-ray Fluorescence, submitted to *Chemistry of Materials*, 2021.

Non peer-reviewed publications:

1. M. M. Besli, Tapping the Full Potential of Raman Spectroscopy, *G.I.T. Laboratory Journal*, 2014, **168**, 26-28.
2. M. M. Besli, Overcoming Optical Focus Issues in Handheld Raman Systems for Analysis of Pharmaceutical Drug Formulations. *European Pharmaceutical Review*, 2015, **20**, 19-21.
3. M. M. Besli, S. Kappes, Was ist drin? - Tragbare Raman Spektrometer, *GIT Labor-Fachzeitschrift*, 2015, **3**, 12-13.
4. M. M. Besli, K. Carron, *Monograph: Introduction to Raman Spectroscopy*, Metrohm AG, Herisau, 1st edn., 2015.

Conference contributions:

1. Spectromicroscopic Investigation of the Chemical and Morphological Heterogeneity in Cycled NCA/PEO Batteries. International School for Materials for Energy and Sustainability VIII, Caltech, Pasadena, USA, July 2019.
2. Cycling Induced Structural Breakdown of NCA in Polymer Batteries. Molecular Foundry User Meeting 2019, The National Center for Electron Microscopy, Lawrence Berkeley National Laboratory, Berkeley, USA, August 2019.

3. Mesoscale Chemomechanical Interplay of the $LiNi_{0.8}Co_{0.15}Al_{0.05}O_2$ Cathode in Solid-State Polymer Batteries. 236th Electrochemical Society (ECS) Meeting, Atlanta, USA, October 2019.
4. (Invited) Understanding Chemical, Mechanical and Thermal Stability of NCA in Polymer Solid-State Batteries. 237th Electrochemical Society (ECS) Meeting, Montreal, Canada, May 2020.
5. Analysis of the Impact of Fast Charging on Aging for Smartphone Cells: A Case Study Using Synchrotron Based Techniques. Electrochemical Society (ECS) PRiME Meeting, October 2020.

Filed patents:

- 3 patents filed in 2019 for Robert Bosch LLC
- 1 patent filed in 2020 for Robert Bosch LLC